AlGaN/GaN high electron mobility transistor (HEMT) based sensors for gas sensing applications

Sokolovskij, Robert

DOI
10.4233/uuid:856522dc-528d-4ac6-95f7-d44fb8791ddc

Publication date
2019

Document Version
Final published version

Citation (APA)
Sokolovskij, R. (2019). *AlGaN/GaN high electron mobility transistor (HEMT) based sensors for gas sensing applications*. [Dissertation (TU Delft), Delft University of Technology]. https://doi.org/10.4233/uuid:856522dc-528d-4ac6-95f7-d44fb8791ddc

AlGaN/GaN high electron mobility transistor (HEMT) based sensors for gas sensing applications

AlGaN/GaN high electron mobility transistor (HEMT) based sensors for gas sensing applications

Dissertation

for the purpose of obtaining the degree of doctor
at Delft University of Technology
by the authority of the Rector Magnificus, Prof. dr. ir. T.H.J.J. van der Hagen,
chair of the Board for Doctorates
to be defended publicly on
Tuesday 10 December 2019 at 12:30 o'clock

by

Robert SOKOLOVSKIJ

Master of Science in Electrical Engineering
Delft University of Technology, the Netherlands
born in Vilnius, Lithuania.

This dissertation has been approved by the promotor.

Composition of the doctoral committee:

Rector Magnificus,	chairman
Prof. dr. G. Q. Zhang	Delft University of Technology, promotor
Independent members:	
Prof. dr. P.M. Sarro	Delft University of Technology
Prof. dr. P.J. French	Delft University of Technology
Dr. ir. R. Poelma	Nexperia
Prof. dr. J.A. Ferreira	University of Twente
Prof. dr. H.Y. Yu	Southern University of Science and Technology
Prof. dr. R. Lee	Hong Kong University of Science and Technology
Prof. dr. W.D. van Driel	Delft University of Technology, reserve member

Keywords: AlGaN/GaN, HEMT, gas sensor, gate recess, 2DEG, H_2S, H_2

Printed by: IPSKAMP Printing

Front & Back: R. Sokolovskij

ISBN 978-94-028-1851-2

An electronic version of this dissertation is available at
`http://repository.tudelft.nl/`.

Dedication

To my Mom, my Family and Zhang Shiqing.

Robert Sokolovskij
Delft, December 2019

Contents

1

Introduction

1.1. Background

In 2018, the global shipments of semiconductors have exceeded one trillion units for the first time [1]. Sensors have accounted for only 3 % of all produced chips (fig. 1.1a), indicating high growth potential. Furthermore, The Trillion Sensors (Tsensors) Initiative presented a roadmap [2] for cumulative annual sensor adoption of one trillion by the middle 2020s (fig. 1.1b). Growing population is the catalyst for wider adoption of sensing technologies for environmental protection, healthcare, sustainability and food produc-

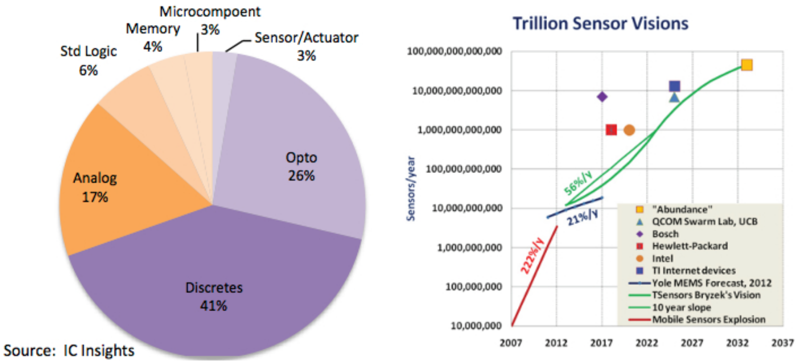

(a) (b)

Figure 1.1: Forecast percentage split of the semiconductor market for 2019 (a). Actual and predicted sensor market growth (b).

tion. The presence of certain hazardous gasses, chemical, organic and inorganic species in the air can cause discomfort, short or long term health effects and even death. Continuous monitoring of people with chronic ailments would enable physicians to remotely observe condition progression thereby reducing healthcare costs. Gas sensors are becoming widely adopted in chemical, energy, aerospace and transportation industries in order to monitor levels of air, water and soil contaminants, as well as process control, leak monitoring, combustion efficiency and worker safety. Advances in monitoring production, preservation and transportation of foodstuffs would result in increased outputs and lower spoilage. Due to varying application specific demands, a common sensing technology satisfying all requirements is not feasible. Therefore, a wide range of sensor types with different transduction mechanisms have been developed over the years.

1.2. HISTORICAL OVERVIEW

Identifying chemical compounds and elements was one of the fundamental challenges of early chemistry research. The pioneering studies on gasses emitted from chemical reactions such as combustion or fermentation were carried out by a Flemish chemist Jan Baptist van Helmont, who in the 17th century introduced the term "gas" [3]. During the 18th and 19th centuries color spectrum analysis was developed to identify various salts, acids and chlorides [4]. Spectral analysis research led to the invention of the first spectroscope in 1859 by G. Kirchhoff and R. Bunsen [5]. However outside of the laboratory environment, detecting gases in air was not possible.

The industrial revolution was a significant historical turning point. Due to the growing need for fuel to run steam engines and produce electricity, the coal mining industry experienced rapid growth during the 18th and 19th centuries. Mining was a very dangerous industry due to accumulation of methane, carbon monoxide and other toxic gases inside the mines. Early attempts at detecting these gases involved bringing a caged canary bird into the tunnels [6]. If the bird stopped chirping it was a strong indication that presence of poisonous gas caused it to die and the workers had to quickly evacuate. At the time electric bulbs were not available, so miners had to rely on open flame lights. Pockets of methane build up could ignite and cause deadly explosions. Around 1815 the flame lamp (or safety lamp) with a glass enclose was developed to prevent the flame from interacting with the outside air [7]. A fine wire mesh allowed only enough air in to keep the light from extinguishing. Later on, markings were added to observe flame height, which indicated oxygen deficient or methane rich atmosphere.

During World War I chemical weapons such as chlorine, phosgene and mustard gas were widely used. Attempts were made to protect soldiers in the field from these agents.

One way of detecting toxic vapor was the Copper Flame Test Lantern [8]. The operating principle was based on characteristic blue-green color of the flame when burning halogens in the presence of copper oxide. The Selenious Acid Field Detector was based on the observations that dilute solution of selenious acid produced orange color suspension upon interaction with mustard gas [9].

Significant advancements in chemical and gas detection technology were made during the 1920s. The first combustible gas detector based on light-wave interference was made by Dr. Jiro Tsuji in 1925 [10]. Two years later Dr. Oliver Johnson developed a catalytic combustion-type sensor for flamable gases [11]. The important results of chemical sensing that were demonstrated thereafter are summarized in table 1.1. Notable are the early results on resistivity variation in semiconductors and metal-oxides exposed to various gasses by Brattain, Seiyama and Taguchi [16, 23, 25], that led to commercialization of metal-oxide (MOX) type sensors. Field effect type sensors made by silicon microfabrication technology were reported soon after to miniaturize the sensing transducers for ion, gas and bio-sensing applications [26, 29, 31]. Sensing in harsh environments promted application of wide-bandgap semiconductors [35, 37, 39] as the current state-of-art of FET sensing technology.

Table 1.1: Historical survey of selected significant chemical sensor developments.

Year	**Sensor type**	**Inventor**
1930	Glass electrode for selective pH measurements	MacInnes [12]
1938	LiCl humidity sensor	Hersch [13]
1946	Photoelectric refractometer	Karrer, Orr [14]
1952	Galvanic cell-type oxygen gas sensor	Hersch [15]
1953	Gas sensitivity of germenium	Brattain, Bardeen [16]
1957	Catalytic activity of semiconducting MOX	Bielański [17]
1957	EMF in solid electrolyte galvanic cells	Kiukkola, Wagner [18]
1961	Solid electrolite oxygen sensor	Weissbart, Ruka [19]
1961	Ion sensitive electrode	Pungor [20]
1962	Biosensor for continous blood analysis	Clark [21]
1962	Pellistor for combustable gases	Baker [22]
1962	ZnO resistive gas sensor	Seiyama [23]
1964	Piezoelectic quartz gas detector	King [24]
1970	Commercial SnO_2 resistive gas sensor	Taguchi [25]
1970	Ion sensitive field effect transistor	Bergveld [26]
1972	Gas sensitive electrodes	Frant [27]
1974	Enzyme thermistor	Mosbach, Danielsson [28]
1975	Pd gate MOSFET H_2 sensor	Lundström [29]
1979	Surface accoustic wave probe	Wohltjen, Dessy [30]
1980	Immunologically sensitive FET (IMFET)	Janata, Huber [31]
1980	Fiber optic pH probe	Peterson [32]
1982	Surface plasmon resonance gas detector	Nylander [33]
1990	Suspended gate FET gas sensor	Lorenz [34]
1993	SiC MOS capacitor H_2 sensor	Arbab [35]
1996	Capacitively controlled FET (CCFET) gas sensor	Gergintschew [36]
1999	SiC MISFET gas sensor	Svenningstorp [37]
2001	Si nanowire chemical sensor	Cui [38]
2001	Pt-AlGaN/GaN HEMT gas sensor	Schalwig [39]

1.3. TYPES OF GAS SENSING TRANSDUCERS

A transducer is a device that converts one form of energy into another. A sensor is a type of transducer that detects a physical change in the surrounding conditions and converts it into an electrical signal for further processing. Based on the type of transduction mechanism gas sensors can be classified into optical, electrochemical, mass-sensitive, calorimetric, magnetic and electrical sensors [40].

Optical gas sensors monitor changes in optical properties of electromagnetic waves upon exposure the target analyte. Optical sensors are broadly classified into those that detect intrinsic optical properties of the target gas or those that monitor optical changes of gas sensitive labels or dies [40]. The optical properties are typically detected based on optical absorption, fluorescence and chemiluminescence. Absorption type sensors utilize the characteristic of certain gas molecules to absorb specific wavelengths of infra-red (IR) or ultraviolet (UV) spectra. A schematic of a widely used non-dispersive infra-red (NDIR) absorption CO_2 sensor is shown in fig. 1.2. It consists of a broadband IR source, gas detection cell with particular path-length and a dual detector with two filters. As the concentration of CO_2 flowing between the inlet and outlet increases the signal intensity detected by the absorption detector through the 4.3 µm wavelength filter is reduced as part of this light is absorbed by the gas molecules. The reference detector measures a wavelength which is not absorbed by the analyte in order to compensate for light source intensity variations [41, 42]. Non-absorbtion based sensors rely on the property of gases such as NO_x or SO_2 to emit light of specific wavelength. Chemiluminescence sensors detect light emitted during oxidation of NO to NO_2 by ozone. Fluorescence optical detectors use a UV source to excite SO_2 molecules to higher energy state, which then decay to lower state and emit a characteristic wavelength in the process. The intensity of detected emission is then correlated to the analyte concentration.

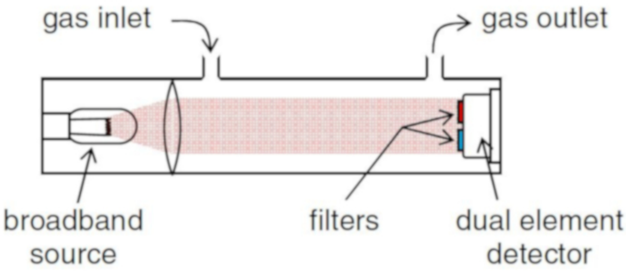

Figure 1.2: Schematic diagram of NDIR sensor [41].

To detect gases that do not have intrinsic optical properties gas sensitive mediators in the form of dies or labels are utilized. Only the mediator is exposed to the gas containing ambient, which causes a change in Its optical property e.g. absorption or luminescence that can be detected by a spectrometer or visual inspection [40].

Electrochemical gas sensors operate on the principal of producing an electrical charge during oxidizing or reducing chemical reaction at the sensing electrode [40]. This charge can then flow between the sensing and auxiliary electrode in a closed loop (circuit). Depending on the type of signal measured, these sensors are differentiated into potentiometric, amperometric and conductometric, that measure changes in voltage, current or conductivity, respectively [43]. A typical sensor consists of two or three electrodes separated by a liquid, polymer or solid electrolyte that together form an electrochemical cell, as is shown in fig. 1.3. The chemical reactions occur at the working electrode which is commonly made using noble metals or carbon to catalyze the reaction. The counter electrode is used to close the circuit with the working electrode and measure the electrical signal [45]. If the sensor requires an external voltage bias, a reference electrode is used to stabilize the potential at the working electrode. The test gas enters the sensor though a capillary barrier and then passes through a hydrophobic membrane that prevents moisture from contacting the working electrode and the electrolyte from leaking out or evaporating too quickly. These sensors have very low power consumption, but their lifetime is limited and depends on ambient temperature and humidity which can cause the electrolyte to evaporate [44].

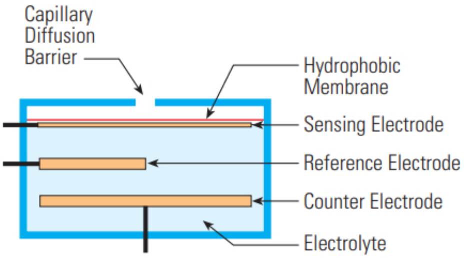

Figure 1.3: Schematic diagram of an electrochemical gas sensor [44].

Mass-sensitive sensors detect changes in mass of the sensitive area exposed to the target gas. Common types of these transducers are the quartz crystal microbalance (QCM), surface acoustic wave (SAW) device and microcantilever, shown in fig. 1.4. QCM sensors consist of a quartz plate with electrodes on each side. Applying a voltage between the electrodes causes the crystal to oscillate at a certain frequency [46]. When gas molecules adsorb on the surface the mass changes resulting in a shift of the resonant frequency, according to the Sauerbrey equation [47]. Therefore the frequency shift is proportional to the gas concentration. The limiting factor of QMB gas sensitivity is the thinning of quartz crystal until it becomes too fragile. A film bulk acoustic resonator (FBAR) allows to enhance gas sensitivity by forming thin piezoelectric films using sputtering or other deposition methods [48], which enables higher resonant frequency in the GHz range.

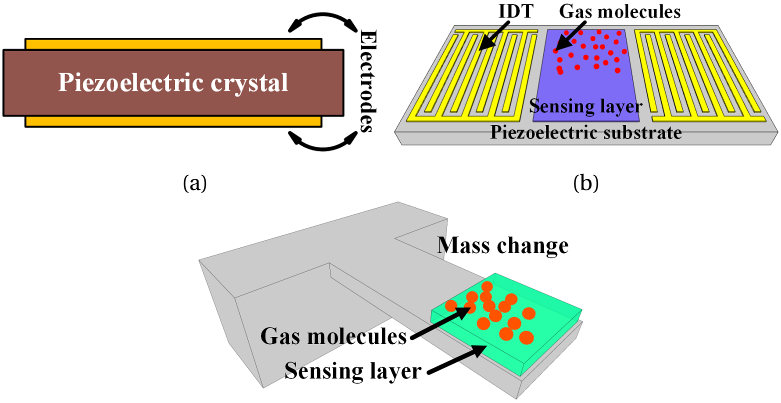

(a)

(b)

(c)

Figure 1.4: Common types of mass-sensitive transducers: (a) quartz crystal microbalance, (b) surface acoustic wave, (c) microcantilever.

SAW sensors also utilize piezoelectric resonators such as quartz plates as a substrate. Metal comb shaped interdigitated transducers (IDT) are patterned on the substrate using deposition and photolithography (fig. 1.4b). A delay line between two sets of IDTs is coated with gas sensing layer to which specific gas molecules can adsorb. When AC voltage is applied at the input IDT, a surface acoustic wave is generated which travels along the surface of the substrate to the output IDT [49]. Adsorbed gas molecules increase the mass of the sensing layer, altering the frequency of the surface wave which is detected by the output IDT. SAW sensors can be designed for resonant frequencies in the GHz range and have higher sensitivity than QCM devices [50].

Microcantilever sensors are mostly fabricated using microelectromechanical (MEMS) surface and bulk micromachining technologies out of silicon, silicon nitride/oxide or polymers. The cantilever tip is functionalized with a gas sensitive layer [40]. These sensors can be operated in a static or dynamic mode. In static mode the deflection of the cantilever caused by surface stress due to adsorbed analyte is measured. In dynamic mode the cantilever is oscillated at its resonance frequency and when gas molecules adsorb on the surface there is a detectable frequency shift. Resonance frequencies of these types of sensors are typically in the kHz range. However due to low stiffness and very small suspended mass of the cantilever the sensing performance is superior to that of QCM or SAW type transducers [51].

Calorimetric (thermometric) sensors sense temperature variations arising from chemical reactions and convert it into a measurable electrical signal. A well know thermometric sensor is the pellistor. It consists of a wire coil, commonly made of Pt, embedded inside a catalytic bead. Figure 1.5 shows a schematic view of a commercial pellistor and a close up of the sensing bead. Applying DC voltage to the coil heats up the bead to approximately 500 °C. In the ambient containing flammable gas, oxidation occurs on the bead surface and extra heat is produced [43]. The increased temperature is detected as higher resistance of the Pt coil, which is proportional to the gas concentration. Frequently the sensor is combined with a reference bead without catalytic coating and connected in a Wheatstone bridge circuit, so that when the resistance of both beads is not equal a voltage signal is generated [53].

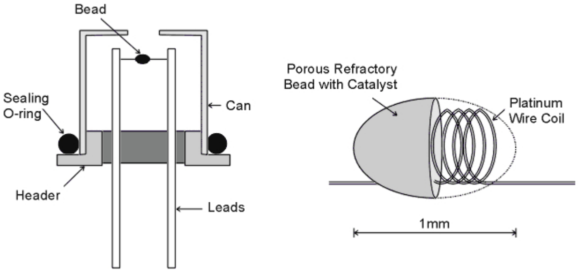

Figure 1.5: Schematic diagram of a pellistor sensor and a close up view of the bead [52].

Thermoelectric (TE) and pyroelectric (PE) devices are another class of thermometric sensors. In the former, a part of a TE film is coated with a catalyst (e.g. Pt). Upon interaction with a combustible gas on the Pt surface an oxidation reaction occurs, which generates heat and a temperature difference along the TE film. A voltage signal, proportional to the gas concentration, can then be detected between the hot and cold part due to Seebeck effect [54]. Similarly, a PE film can be heated by placing a catalyst on top of it, which will alter the electric polarization of the film and generate a voltage difference across it [55].

Utilizing the differences of thermal conductivity of certain gases is another way to implement a sensor. A basic thermal conductivity gas sensor consists of two identical heating elements, such as non-catalytic pellistor beads, connected in a Wheatstone bridge (fig. 1.6). One bead is placed inside a reference gas chamber and the other in the test chamber and both are heated to the same operating temperature [56]. Once a gas with a higher or lower thermal conductivity is injected the temperature of the bead reduces or increases compared to the reference and a signal is detected equivalently to the pellistor.

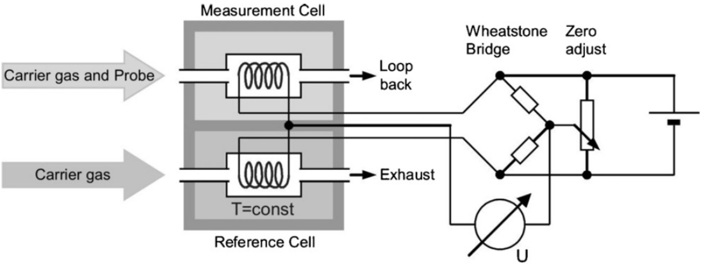

Figure 1.6: Diagram of thermal conductivity sensor connected in a Wheatstone bridge [56].

Magnetic sensors utilize the paramagnetic properties of gases and are not widely used. The most well-known application of this type of sensors is for detecting oxygen as it has high magnetic susceptibility compared to other common gases. A notable magnetic oxygen sensor is the magneto-dynamic dumbbell device [57].

Electrical sensors directly interact with the target gas which results in the change of their electrical properties. These devices cover a wide range of sensing methods and employ different types of materials such as polymers, metals, metal-oxides and semiconductors. Conductometric or resistive sensors detect variations of electrical conductivity of the sensing layer due to adsorbtion, chemical reactions, catalytic dissociation, expansion or shrinkage. Selection and preparation of the appropriate sensing material is essential for these devices. Very widely applied sensing layers are metal oxide (MOX) semiconductors such as as ZnO, SnO_2, TiO_2, In_2O_3 , and WO_3, NiO and Ga_2O_3. The detection mechanism of these sensors is attributed to adsorption and desorption of oxygen. In the case of n-type MOX ambient oxygen chemisorbs on the surface, consumes surface electrons and forms ionic species ${O_2}^-$, O^-, O^{2-} thereby increasing the material resistivity. When reducing gases such as H_2, CO or NH_3 are introduced they react with the adsorbed oxygen and release electrons back into the conduction band of the MOX and the resistivity is reduced proportionally to the gas concentration. Reaction with oxidizing gases (e.g. NO_2, CO_2) consumes additional electrons thereby increasing the resistivity above the initial value. The resistivity changes of p-type MOX sensing layers are opposite of n-type based sensors. To obtain sufficient gas sensing response and for the chemical reactions to occur at the fast enough rate the MOX sensors are generally operated at high temperatures of 100–900 °C [58]. Various sensor configurations are shown in fig. 1.7. The pellet structure (fig. 1.7a), consisting of a metal-oxide disk sandwiched between two metal contacts was used early on to study the effects of humidity, temperature and gases on SnO_2 conductance [61]. Figure 1.7b shows the commercially available tube type sensor, with a ceramic cylinder as a non-conductive substrate. A metal coil heater

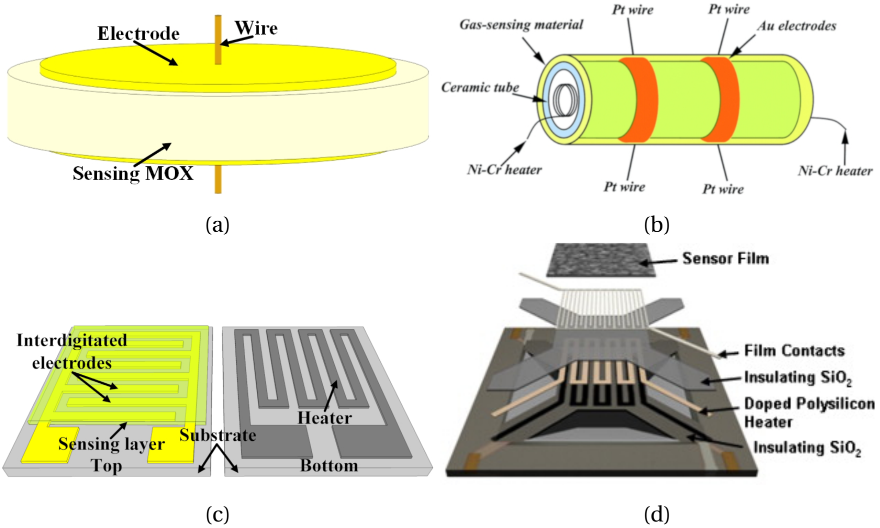

(a) (b)

(c) (d)

Figure 1.7: Resistive sensor types: (a) pellet, (b) tube [59], (c) planar IDT, (d) microhotplate [60].

is inserted inside the tube and the outer surface has electrodes formed on each end [59]. The area between these electrodes is coated with the required MOX layer for the target gas. This structure is suspended between the posts of the sensor package using Pt wire bonds to minimize heat loss via conduction. A planar geometry utilizes interdigitated electodes that are patterned on the insulating substrated (fig. 1.7c) and the gas sensitive layer is then applied on top. A resistive heater can be fabricated on the backside to control the operating temperature. This structure has several advantages. Firstly, it allows for a larger contact area between the electrodes and the sensing layer in a compact form factor. In addition, is it well compatible with thin and thick film deposition methods such as sputtering or screen printing, respectively [62]. Furthermore, the electrode width, spacing and position can be optimized to enhance the sensor response [63]. Devices with ceramic substrates require roughly few watts of power to obtain the necessary operating temperature. To reduce the power consumption especially for portable and battery powered applications, the microhotplate structure is utilized fig. 1.7d. Here miniaturized sensors are fabricated using MEMS processing on silicon. The heater and IDT electrodes are fabricated on a thin dielectric membrane, which is suspended by etching the Si underneath. The heater power consumption of these devices is in the mW range [60].

Sensing material selection and microstructure optimization are of critical importance for resistive gas sensor research. Besides binary metal oxides, numerous complex ternary and quaternary materials have been studied [64]. MOX composites and noble metal nanoparticle doping (loading) have also been implemented in order to enhance sensor performance [65]. Furthermore quasi two-dimensional and one-dimensional structures such as nanosheets, nanowires, nanotubes, nanoribbons etc. were successfully utilized for conductometric sensors. MOX nanostructures possess superior sensing performance in comparison to their thick and thin film counterparts due to larger porosity and surface-to-volume ratios [66, 67].

Thin metal film gas sensitive chemiresistors have also been reported. Noble metals such as Pt, Pd or Ir have demonstrated resistance variations upon interaction with hydrogen containing gases. The highest solubility of H_2 among the platinum group metals is in Pd. Resistive structures are made on substrates like glass, Si or ceramic by Pd deposition and patterning. Thick and thin film Pd resistors have been previously demonstrated [56]. The sensing mechanism is based on catalytic dissociation of H_2 molecules into H atoms on the metal surface. These atoms then diffuse into the metal and occupy the interstitial sites of the Pd lattice and form palladium hydride (PdH_x) [56, 68], which also causes the lattice to expand [69]. Electrical resistance of PdH_x is higher than of H-free Pd, hence the sensor resistance increases with increasing H_2 concentration. Several factors such as film thickness, defect density, morphology and operating temperature affect the sensing performance of metal chemiresistors. Pure Pd sensors exhibit phase transitions under higher H_2 concentrations (2-3 %) due to increasing lattice expansion which in turn causes hysteresis behaviour of sensor response and low reliability due to cracking, blistering and delamination of the metal film after few cycles of gas exposure [70]. In order to improve sensor stability several alloys such Pd-Ag, Pd-Au or Pd-Ni have been investigated as hydrogen sensors. It was demonstrated that adding 7% of Ni into the alloy eliminated phase transitions and hysteresis during H_2 measurements as well as prevented film delamination [71]. The sensing response of pure Pd was higher than of Pd-Ni alloys, but the response times were also substantially longer.

Polymer materials are also widely applied for gas sensing applications. Polymers are in most cases organic macromolecules made of carbon and hydrogen atoms with minor amounts of other atoms e.g. nitrogen, oxygen, sulphur, phosphorus and halogens [72]. A wide variety of different polymers have been synthesised over the years. Electrically conducting polymers are most promising and widely applied for chemiresistors. p or n type conductivity can be altered by chemical, electrochemical, photochemical and interfacial doping [73]. Gas sensor fabrication with polymer active layers allows for more design flexibility as these materials can be deposited electrochemically, by dip or spin coating, thermal evaporation and other techniques [74]. Some of the most studied polymers for gas and volatile organic compound (VOC) sensing are polypyrrole (PPy) polyaniline (PAni), polythiophene (PTh), Polyacetylene (PA) and poly

(3,4-ethylenedioxythiophene) (PEDOT). Furthermore sensing properties of these materials can be enhanced by modifying their molecular structure, doping or forming composites by incorporation of non-conducting polymers, metal-oxides or metal nanoparticles. Conductivity variations upon analyte exposure arise from chemical redox reactions which cause doping/de-doping due to electron transfer between gas and polymer. Adsorption of certain VOCs results in resistivity modulation due to mass transfer and swelling. The key advantage of polymer sensing layers is the sufficiently strong interaction with gases at room temperature, resulting in fast response times and low power consumption. Long term stability is a major concern for these materials. It was reported that exposure to air for prolonged time caused de-doping and reduced sensor performance. Similarly to MOX, selectivity of polymer sensors is limited as conductivity is influenced by humidity, temperature and presence of interfering gases in the ambient [74].

Capacitive sensors utilize changes in capacitance as sensing signal when exposed to target gas or vapour. Capacitance (C_0) of a parallel plate capacitor is expressed as:

$$C_0 = \frac{\epsilon_0 \epsilon_r A}{t} \tag{1.1}$$

where ϵ_0 and ϵ_r are the vacuum and relative dielectric permittivity, A – electrode area, t – distance between plates (i.e. dielectric thickness). Therefore, in order to vary the C_0, interaction with the analyte should alter the ϵ_r, A or t [75]. The typical sensor structures are the interdigitated electrode similar to fig. 1.7c or parallel plate with a porous top electrode. The dielectric layer is utilized as sensing material, which is commonly a metal oxide or a polymer. Detection of gases in air, which relies on variations in dielectric constant is challenging as the relative permittivity of gases is very similar to that of air, however it can be achieved with low noise capacitance readout circuits [76]. Humidity and VOC sensors based on ϵ_r changes are more common. It is due to high permittivity of water (ϵ_r=76) compared to air (ϵ_r=1). Adsorption of analyte on a polymer sensing layer can affect not only the ϵ_r value but can also cause polymer swelling, which will increase the effective electrode area A, hence two parameters affect capacitance variations simultaneously as illustrated in fig. 1.8 [77]. Effective capacitive sensing of gases is achievable utilizing the metal-oxide-semiconductor (MOS), metal-semiconductor or p and n type semiconductor junctions. In these cases depletion layers are formed that contribute to the total capacitance of the structure. The thickness of the depletion layer can be modified via gas interaction with the top electrode or at p-n grain boundaries. These types of devices are further discussed in section 1.4 where field effect type sensors are presented.

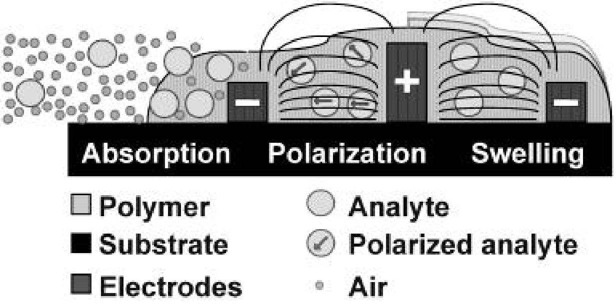

Figure 1.8: Schematic diagram showing the effects of analyte absorption, polarization and swelling, which affect ϵ_r and area (A) [57].

1.4. FIELD EFFECT GAS SENSORS

A distinct class of conductometric chemical sensors are field effect devices. The first chemical sensors of this type were the silicon ion sensitive field efect transistor (ISFET) invented by Bergveld in 1970 [26] and Pd-gated Si metal oxide semiconductor field effect transistor (MOSFET) H_2 gas sensor invented by Lundström [29] in 1975. Other frequently used gas sensing field effect transducers are the Schottky barrier diode (SBD) and MOS capacitor. The Schottky diode is the simplest structure to fabricate and consists of the Si substrate on top of which a gas sensitive catalytic metal (e.g. Pt, Pd or Ir) Schottky contact is deposited and the ohmic contact is formed on the backside (fig. 1.9a). The ideal current-voltage characteristic of a Schottky diode, according to thermionic-emission transport model, is expressed as [78]:

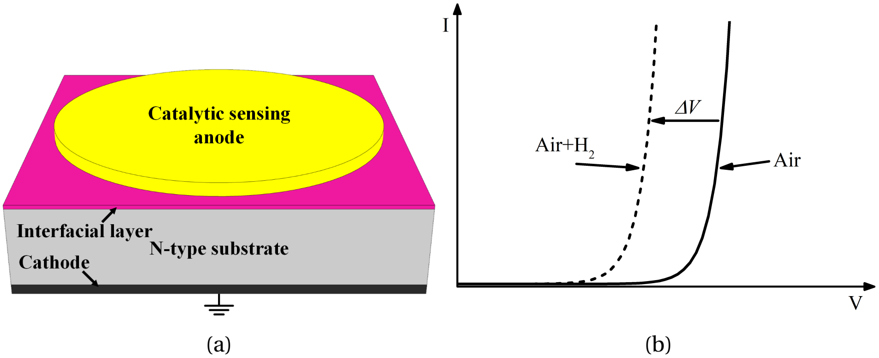

(a) (b)

Figure 1.9: Schematic of a Si SBD sensor (a) and I-V curve with a shift upon exposure to H_2 (b).

$$I_D = I_S\left(e^{\frac{qV_D}{nkT}} - 1\right) \tag{1.2}$$

and

$$I_0 = AA^{**}T^2 e^{\frac{-q\phi_b}{kT}} \tag{1.3}$$

where I_D and V_D are the diode current and bias voltage receptively, I_s is the reverse saturation current, q the elementary charge, n the ideality factor, k the Boltzmann constant, T is the temperature in Kelvin, A is the contact area, A^{**} the effective Richardson constant and ϕ_b is the Schottky barrier height, which is the difference between the metal work function ϕ_m and the semiconductor electron affinity χ_s, ϕ_b=ϕ_m-χ_s. An example I-V curve of a SBD is shown in fig. 1.9b. Sensor interaction with target gas results in the measurable shift of this curve caused by the variation of the Schottky barrier height ($\Delta\phi_b$). In the case of Si-based diode sensors there is large density of surface states at the metal-semiconductor interface, causing Fermi level pinning and a fixed barrier height independent of metal work function variation. Incorporating a thin interfacial insulator layer between the metal and semiconductor lowers the number of surface states and restores work function dependant Schottky barrier height. The interface layer is few nanometers thin and still permits current tunnelling across the diode.

The MOS capacitor has a similar structure to Schottky diode except the dielectric layer is thicker to prevent current conduction (fig. 1.10a). Device capacitance is defined

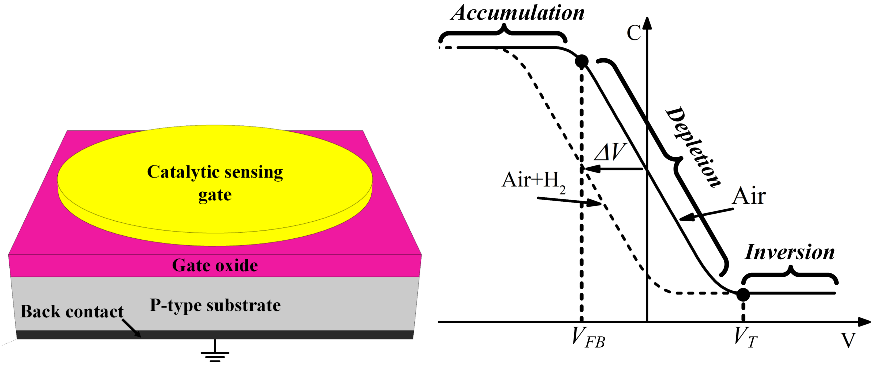

(a) (b)

Figure 1.10: Schematic of a MOSCAP sensor (a) and I-V curve with a shift upon exposure to H_2 (b).

as differential variation of charge (Q) with respect to change in voltage:

$$C = \frac{dQ}{dV} \tag{1.4}$$

The MOS capacitor has three operating regions corresponding to applied voltage: accumulation, depletion and inversion, as shown in fig. 1.10b. For p-type Si MOS accumulation occurs when a negative voltage (V_G) is applied on the top gate electrode, which induces a negative charge on the metal and positive charge in the semiconductor. The accumulation capacitance is simply equivalent to the dielectric capacitance according to eq. (1.1). Accumulation capacitance per unit area (C'_{acc}) is expressed as:

$$C'_{acc} = C'_{ox} = \frac{\epsilon_{ox}}{t_{ox}} \tag{1.5}$$

where ϵ_{ox}=$\epsilon_0\epsilon_r$ and t_{ox} is the oxide thickness. As the gate voltage increases a point is reached where the net charge density at the semiconductor surface is zero and there is no energy band bending at the oxide-semiconductor interface. This voltage is known as flatband voltage and is expressed as [79]:

$$V_{FB} = \phi_{ms} - \frac{Q'_{ox}}{C'_{ox}} = \phi_{ms} - \frac{qN_{ox}}{C'_{ox}} \tag{1.6}$$

where ϕ_{ms} is the metal-semiconductor work function difference, Q'_{ox} is the trapped charge density in the oxide and N_{ox} is the number of oxide charge centres per unit area. Above V_{FB} a space charge region begins to form in the semiconductor at the interface. The capacitance of the space charge region (C'_{sc}) is:

$$C'_{sc} = \frac{\epsilon_s}{x_d} \tag{1.7}$$

and is dependent on the space charge region width x_d and the permittivity of Si (ϵ_s). The depletion capacitance is then the series connection of C'_{ox} and C'_{sc}:

$$C'_{dep} = \frac{C'_{ox}C'_{sc}}{C'_{ox} + C'_{sc}} = \frac{\epsilon_{ox}}{t_{ox} + (\epsilon_{ox}/\epsilon_s)x_d} \tag{1.8}$$

and the space charge region width is:

$$x_d = \sqrt{\frac{2\epsilon_s\varphi_s}{qN_A}} \tag{1.9}$$

where N_A is the substrate doping concentration and φ_s is the surface potential, or potential difference between the semiconductor surface and the bulk. The relation between φ_s and the bias voltage (V_G) is expressed as:

$$V_G = V_{FB} + \varphi_s + \frac{\sqrt{2\epsilon_s qN_A}}{C'_{ox}}\sqrt{\varphi_s} \tag{1.10}$$

Therefore the φ_s and consequently x_d increases with increasing V_G and reaches the highest value x_{dT} at $\varphi_s = 2\phi_F$. ϕ_F is the Fermi potential and the corresponding gate voltage is known as the threshold voltage V_T of the MOSCAP:

$$V_T = V_{FB} + 2\phi_F + \frac{\sqrt{2\epsilon_s q N_A}}{C'_{ox}}\sqrt{2\phi_F} \tag{1.11}$$

At threshold voltage the MOS capacitance is at the minimum value:

$$C'_{min} = \frac{\epsilon_{ox}}{t_{ox} + (\epsilon_{ox}/\epsilon_s)x_{dT}} \tag{1.12}$$

Above V_T the capacitor transitions to inversion. Minority carriers i.e. electrons are generated and diffuse towards the semiconductor surface inverting the surface region to n-type. This charge generation occurs at a specific rate and therefore is dependent on the frequency of the AC signal used to measure the C-V characteristics. The inversion capacitance is then equivalent to C'_{ox} under low frequency measurement and to C'_{min} under high frequency. In most cases high frequency characteristics are of interest. When a MOSCAP sensor is exposed to target gas a shift of the capacitance-voltage (C-V) curve along the voltage axis is measured as response signal (fig. 1.10b).

The MOSFET is a voltage controlled switch. The basic structure consists of the MOS capacitor which is contacted on both sides with highly doped regions (n^+ in the case of n-channel FET) called the source and drain (fig. 1.11a). When the gate-source voltage (V_{GS}) is higher than threshold voltage ($V_{GS} > V_T$) the inversion channel of electrons is formed and connects the source and drain contacts allowing current to flow if voltage (V_{DS}) is applied. FETs that require a $V_{GS} \neq 0$ to form the channel are called enhancement mode, while those with the channel already present at $V_{GS} = 0$ are depletion mode.

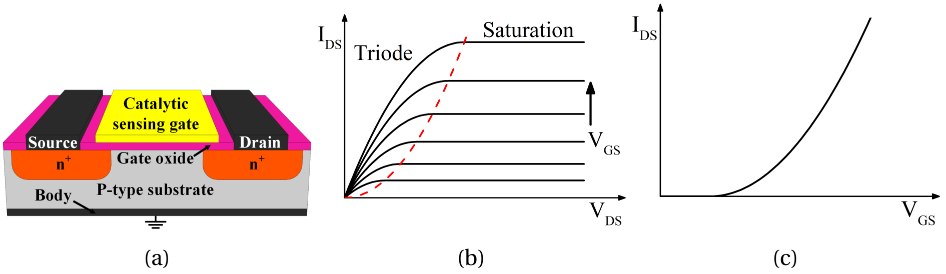

(a) (b) (c)

Figure 1.11: (a) Schematic of a Si MOSFET sensor. (b) Output ($I_{DS}-V_{DS}$) and (c) tranfer ($I_{DS}-V_{GS}$) curves of a MOSFET.

When $V_{GS} - V_T > V_{DS}$ the drain current of the MOSFET is expressed as [78]:

$$I_D = \frac{W \mu_n C'_{ox}}{2L} [2(V_{GS} - V_T)V_{DS} - V_{DS}^2] \tag{1.13}$$

where W and L are the MOSFET gate width and length respectively and μ_n is the electron mobility. This is called the triode region of operation. Once the drain-source voltage is raised to the level of $V_{GS} - V_T = V_{DS}$, the drain current reaches saturation (I_{Dsat}) and, in an ideal case, is independent of V_{DS}:

$$I_{Dsat} = \frac{W \mu_n C'_{ox}}{2L} (V_{GS} - V_T)^2 \tag{1.14}$$

An example drain current versus drain-source and gate-source voltage curves are shown in fig. 1.11b and fig. 1.11c respectively. An important FET parameter is the transconductance (g_m) which is defined as the variation of drain output current with respect to variation of gate voltage. Saturation region g_m is expressed as:

$$g_m = \frac{\partial I_{Dsat}}{\partial V_{GS}} = \frac{W \mu_n C'_{ox}}{L} (V_{GS} - V_T) \tag{1.15}$$

If the gate of FET is made using a gas sensitive layer (e.g. catalytic metal), a shift in both output (fig. 1.12a) and transfer (fig. 1.12b) curves can be measured as response signal.

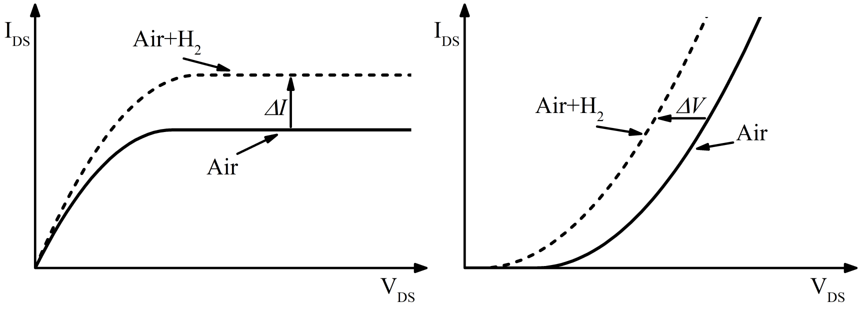

(a)

(b)

Figure 1.12: Example (a) output and (b) transfer I-V curves of a FET-sensor with a shift upon exposure to H_2.

The Schottky diode type sensor is a two terminal device. The interaction with target gas may affect not only the barrier height but also the resistivity of the anode terminal due to metal hydride formation. Therefore the sensing signal variation is not only due to Schottky barrier height changes but also anode series resistance which can impact sensor stability. In the MOS capacitor current does not flow between the terminals and the

C-V curve shift is only due to work function change of the sensing electrode. The main drawback of a MOSCAP sensor is the necessity to apply AC voltage for capacitance measurements, which makes the readout circuitry more complex. Both SBD and MOSFET type sensors are operated in DC mode. The latter has further advantages of the sensing gate terminal being isolated from the signal current flow, hence the sensor response is purely due to field effect. Furthermore, the response current magnitude is larger than of the diode type sensor and the sensitivity can be optimized by the gate bias voltage.

Over the years several modifications to the catalytic gate MOSFET were presented in order to increase the number of detectable species, enhance sensitivity and selectivity. The suspended gate FET (SG-FET) was introduced by Janata [80]. It incorporates an air gap of 100 nm to 1000 nm between gate oxide and the sensing layer as shown in (fig. 1.13). The air gap is formed by inserting a sacrificial layer (e.g. metal or low temperature oxide) above the gate area during device fabrication. After the metal gate electrode is formed, the sacrificial layer is selectively etched. The gate electrode can be coated with a gas selective layer before or after air gap etching by vacuum techniques or electrochemical deposition [34]. The test gas diffuses into the air gap, adsorbs on the sensing layer and gate oxide, resulting in a work function shift [82]. The disadvantage of the FG-FET is the large reduction of the gate capacitance due to the air gap. The effective gate capacitance C'_{eff} now becomes a series connection of C'_{ox} and air capacitance (C'_{air}):

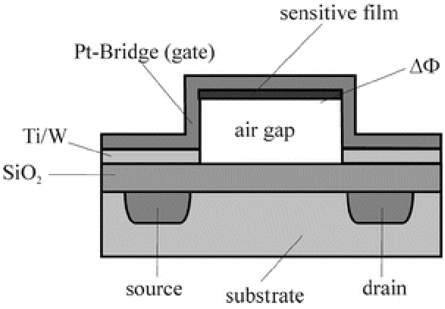

Figure 1.13: Schematic diagram of the suspended gate field effect transistor [81].

$$C'_{eff} = \frac{C'_{ox} C'_{air}}{C'_{ox} + C'_{air}} \tag{1.16}$$

The low capacitance results in reduction of the output current, the transconductance and increase of the threshold voltage up to 100 V (see eqs. (1.11), (1.14) and (1.15)). To avoid using high bias voltage, depletion mode FETs are commonly implemented in FG-FETs, while I_D and g_m are partially restored by increasing the W/L ratio.

The hybrid suspended gate FET (HSG-FET) was developed soon after to further expand the flexibility of sensitive layer deposition. In the HSG-FET the suspended sensing gate is fabricated separately from the un-gated Si FET, therefore wide choice of material types, substrates and deposition methods can be used to prepare the sensitive layer. The suspended electrode is attached above the FET channel region by flip-chip bonding and spacers are added to control the height of the air gap, as shown in fig. 1.14a. A further improvement was the capacitively coupled FET (CC-FET), introduced by [83]. It is made of a capacitor with an air gap and a FET as shown in fig. 1.14b. One of the capacitor plates is coated with gas sensitive layer such as catalytic metal or MOX. One of the plates is connected to the gate of the FET and is at floating potential while the other plate is grounded. Gas molecules adsorbed on the sensing layer cause charging of the plate and a corresponding work function shift, which in turn causes a potential shift of the FET gate and drain current variations. The advantage of this device over the SG-FET is that the air-gap capacitor size is not limited by the dimentions of FET gate. Therefore high C'_{air} and sensing signal can be achieved avoiding high W/L ratio of the FET. The CC-FET enables different sensor implementations that are determined by available manufacturing capabilities, costs and miniaturization requirements, specifically discrete, hybrid and integrated approaches [83]. The floating gate terminal of the CC-FET is exposed to the environment and is therefore susceptible to interference from stray electric fields and leakage current due to charge accumulation by water adsorption on the Si_3N_4/SiO_2 passivation layer under higher relative humidity [84, 85]. To eliminate these problems the sensors had to be screened between electrodes with known potential and a guard ring was added around the floating electrode.

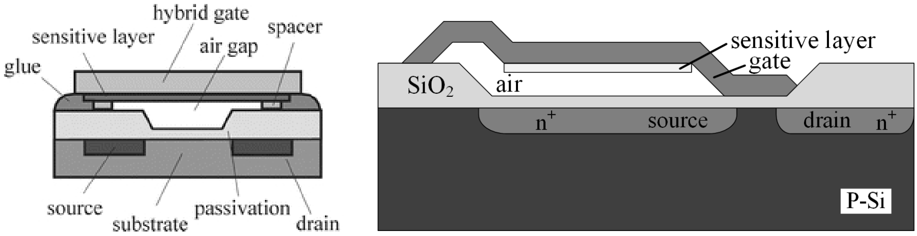

(a) (b)

Figure 1.14: Schematic diagram of (a) the hybrid suspended gate [81] and (b) capacitively coupled field effect transistor type sensors.

To overcome the issues observed with the HSG-FET and CC-FET the floating gate FET (FG-FET) sensor was introduced [86]. It consists of a capacitive voltage divider including the gas sensitive electrode and the sensing signal readout MOSFET (fig. 1.15a).

The main structural difference is that the gate electrode is buried between insulating layers which improves device stability. The capacitive divider (fig. 1.15b) consists of oxide (C_{Ox}), passivation (C_{Pass}) and air gap (C_{Gap}) capacitances in series, with separate n-well, extended floating gate electrode and hybrid mounted top sensing electrode being the capacitor plates. The work function shift ($\Delta\phi$) of the sensing electrode modifies the potential of the floating gate by ΔV_{FG}, expressed as:

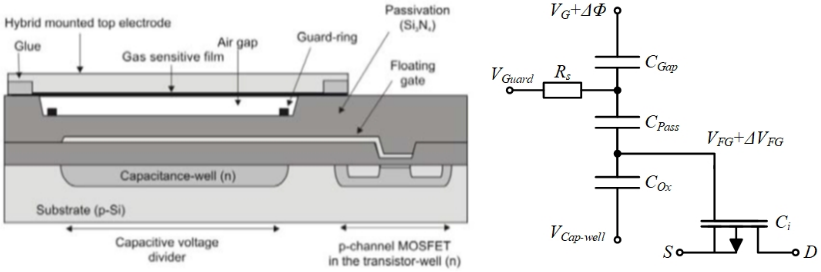

(a) (b)

Figure 1.15: Schematic diagram of the floating gate field effect transistor type sensor (a). Equivalent circuit diagram of the capacitive voltage divider and MOSFET connection of the FG-FET [86].

$$\Delta V_{FG} = \frac{C_1}{C_1 + C_{Ox}} \Delta\phi = \gamma \Delta\phi \tag{1.17}$$

and

$$C_1 = \frac{C_{Gap} C_{Pass}}{C_{Gap} + C_{Pass}} \tag{1.18}$$

where γ is the coupling coefficient. It is desired to have γ close to 1, to obtain a gate voltage shift similar to the work function change. None the less, the sensor sensitivity is orders of magnitude higher compared to the SG-FET, as the gate capacitance of the FG-FET is equal to gate oxide capacitance (C_i), resulting in higher transconductance. The biasing conditions of the FET can be set by applying voltages to $V_{Cap-well}$ and V_G.

Recently a MOSFET type sensor with a horizontal floating gate was demonstrated [87, 88]. The fabricated device and schematic sections along indicated cut planes are shown in figs. 1.16a–1.16c. The MOSFET with the floating gate (FG) is processed first and isolated with Si_3N_4. The control gate (CG) electrode is then fabricated to surround the floating gate. The sensing layer is deposited and patterned in the last step between the FG and part of the CG, forming capacitive voltage divider as shown in fig. 1.16d. This sensor design does not require an air gap, as the capacitors are formed between the sidewalls of the CG and FG, therefore the C_{Gap} is effectively replaced by the capacitance of the sensing layer (C_S). Increasing the coupling ratio (γ) is possible by forming an

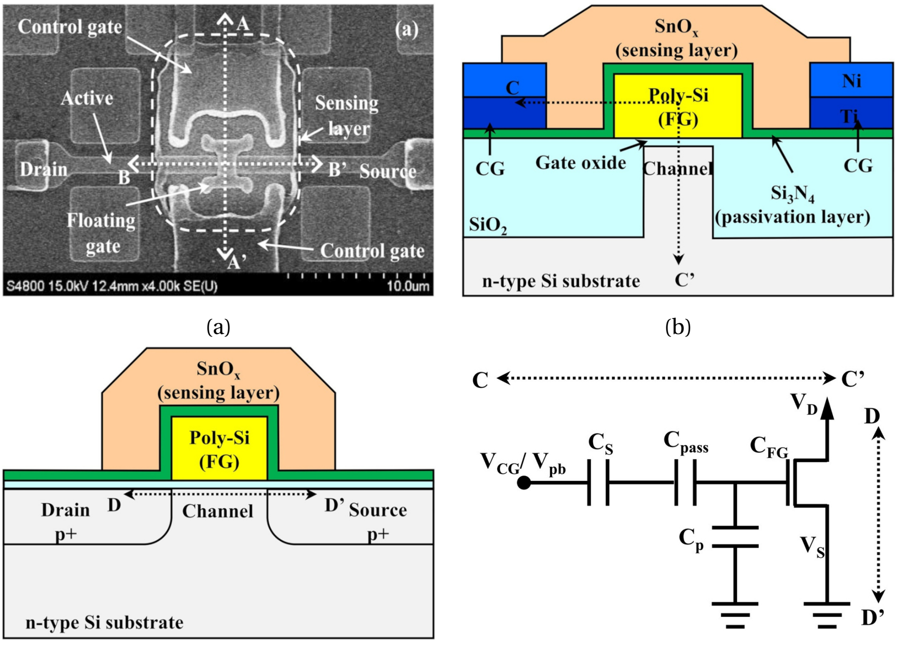

(a) (b)

(c) (d)

Figure 1.16: SEM image of the horizontal floating gate MOSFET sensor (a). Schematic cross-section view along cutline (b) A-A' and (c) B-B'. Equivalent circuit diagram along cut C-C' in (b) and D-D' in (c) [88].

interdigitated structure of the CG and FG electrodes outside the FET active area [89]. This structure is adventitious in terms of manufacturing complexity as it eliminates the hybrid mounting of the sensing electrode, required by HSG-FET and FG-FET sensors.

1.5. Compound semiconductor FET sensors

1.5.1. Limitations of Si-FET sensors

Silicon is the currently established material for most analog, digital and power microelectronics applications. Quality of substrates and microfabrication technologies of Si-based devices have reached maturity years ago and material costs have reduced drastically. Due to the low bandgap (1.12 eV) the maximum operating temperature of Si-based FET sensors is limited to approximately 200 °C. Above this temperature the intrinsic carrier concentration increases to values similar to p or n-well doping, which results in high leakage currents to the substrate and device failure [90]. Si is also not suitable for operation in corrosive environments as is it quite reactive and is etched by certain vapours.

Numerous applications and catalytic reactions require temperatures above the Si limit.

1.5.2. III-V SEMICONDUCTORS FOR FET-SENSORS

Other semiconductor materials, notably compounds of group III elements (i.e. B, Al, Ga, In) with group V elements (i.e. N, P, As, Sb) have been investigated in order to expand the field effect type sensor operating temperature range, enhance sensitivity and detect a wider variety of compounds. Indium phosphide (InP) Schottky diode with a Pd anode was demonstrated to detect 100 ppm of H_2 in N_2 ambient by C-V measurements [91]. Early gallium arsenide (GaAs) Schottky diode with Pt sensing layer also demonstrated detection of H_2 down to 6 ppm in N_2 and 200 ppm in air [92]. Molecular beam epitaxy (MBE) was used for the growth of low defect density GaAs which allowed to reduce Fermi level pinning. Pd-InP and GaAs were also applied for MOS Schottky diodes. The interfacial oxide was realized by thermal oxidation [93]. Under same conditions InP sensors demonstrated higher barrier shift ($\Delta\phi_b$) and sensitivity towards H_2. GaAs Schottky diodes with Pt, Pd and Ir as sensing electrodes were compared for detection of H_2 and NH_3 [94]. It was found that sensors with 100 nm thick Pd were most sensitive to H_2 and had fastest response. Porous 5nm Ir and Pt was suitable for NH_3 detection, with Ir showing higher response in N_2 ambient, while Pt in air. Besides SBDs, GaAs metal-semiconductor and metal-insulator-semiconductor field-effect transistors (MESFET and MISFET) H_2 sensors were also demonstrated [95, 96]. Gate electrodes of Pd and Pt were shown to detect H_2, NO_2, NH_3 and did not respond to humidity, CO, CO_2, CH_4 at tested temperatures. Schottky MS and MOS diodes utilizing ternary alloys of InGaP, AlGaAs, InAlP and InAlAs have also been implemented as H_2 sensors [97–100]. Later on, high electron mobility transistors (HEMT) with MS and MOS gates were also reported using the aforementioned alloys [101–104]. The FET and HEMT structures are advantageous due to higher response signal magnitude compared to SBD, as the gate potential variations are translated into output drain current change. A disadvantage of the III-V based sensors is that the device structures are typically grown on costly as well as fragile doped or semi-insulating InP and GaAs substrates. These substrates are also susceptible to damage from chemical etchants and corrosive environments.

1.5.3. WIDE-BANDGAP SEMICONDUCTOR FET-SENSORS

Wide-bandgap (WBG) semiconductors are defined as those having a bandgap >2 eV. Materials that are most promising and widely studied for various FET applications are silicon carbide (SiC), diamond, gallium oxide (Ga_2O_3) and gallium nitride (GaN).

SiC exists in numerous crystal structures, known as polymorphism. Depending on the polytype the bandgap of SiC can vary from 2.39 eV to 3.33 eV [105]. Only 4H and 6H polytype substrates are readily available for purchase at this time. The pioneering reseach in applying SiC for sensing FET sensor applications was carried out by NASA Lewis Research Center and Linköping University. They presented a MS Pt-Schottky diode [106] and a Pd/SiC-MOSCAP [35], fabricated on 6H-SiC substrates, respectively. These initial reports already demonstrated operating temperature up to 600 °C, which enabled detection of not only H_2 but also various saturated hydrocarbons. Stability of SiC allowed monitoring of exhaust gas mixtures and detect the air/fuel ratios in engine cylinders and exhaust pipes in automotive applications where fast response times and high operating temperatures are required [107]. Introducing a buffer layer of $TaSi_x$ above the gate oxide improved adhesion of Pt sensing layer, reduced signal drift and extended operating temperature above 700 °C. These devices required sensing activation at 550 °C using alternating pulses of H_2, ethane or propane in Ar and oxygen in Ar [108]. The first MOSFET high temperature H_2 sensor on 4H-SiC was also developed by ACREO and Linköping University [109]. This FET design had a burried gate structure with ion implanted source/drain extention regions fig. 1.17a. Such approach allowed to limit damage to the gate oxide and move the conductive channel away from the surface. By changing the channel region implatation dose, both enhancement and depletion mode devices were fabricated. The burried channel and high quality gate oxide permitted stable operation of sensors at 600 °C [37]. Pulsed laser ablation method of Pt deposition directly on SiO_2 of SiC MOSCAP demonstrated good adhesion without the need for barrier layer, which can interfere with gas detection [110]. Substituting the thermally grown SiO_2 with AlN had also improved adhesion of Pt, deposited by RF sputtering [111]. Metal oxide nano-particles (e.g. RuO_2) and metal-oxide films (e.g. $InSnO_x$) were also utilized as sensing electrodes for SiC MOSCAPs and depletion MOSFETs to detect H_2, C_3H_6, O_2 and NO_x [112, 113]. Another promising modification of the SiC SBD and MOSCAP sensors was to replace the thermally grown SiO_2 with a chemically sensitive metal oxide, thereby forming a metal-reactive insulator-semiconductor or MRIS devices. In such structure, both the catalytically active metal contact and the MOX are exposed to and react with target gas[114]. It was observed that compared to MOS-SiC devices, the MRISiC sensors had improved sensitivity and stability. Numerous MOX (e.g. SnO_2, CeO_2, Ga_2O_3, WO_3) were studied for MRISiC devices as reported in [115]. Furthermore, nanostructured MOX layers were also reported as interfacial layers for SiC sensors, which allowed to increase the gas sensitive surface area as nanostructures have higher surface-to-volume ratios compared to their thin film counterparts [116]. As the substrate quality and microfabrication developed the SiC-FET based sensors became more widely studied. Enhancement and depletion type device technology (figs. 1.17b and 1.17c) with improved long-term stability was developed by [117]. It worth noting that depletion mode devices did not require

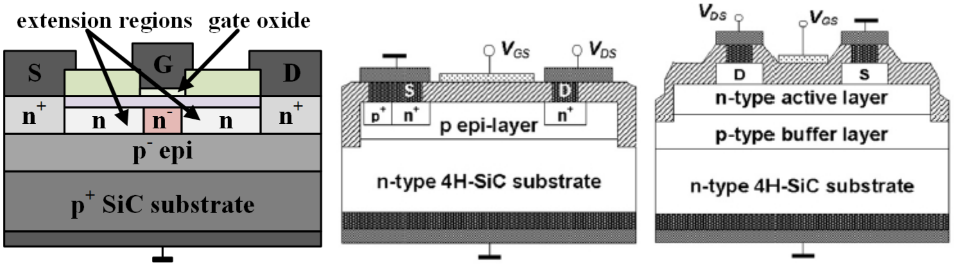

(a) (b) (c)

Figure 1.17: Cross-section diagram of (a) first generation burried gate SiC MISFET sensor, (b) enhacement and (c) depletion type second generation SiC MISFET sensors [117].

any ion implantation steps, thereby reducing processing costs and complexity. These sensors with different catalytic gate electrodes were utilized for detection of low concentrations of volatile organic compounds.

Diamond is another promising candidate material for FET sensing applications. The first diamond MIS diode type sensor was reported by Vanderbilt University [118]. Their device used PECVD to deposit a p-doped/undoped polycrystalline diamond on a tungsten substrate at 850 °C, Pd was employed as sensing electrode. High sensitivity to H_2 was obtained at 85 °C. The I-V characteristics of these sensors shifted from nearly ohmic in air, to rectifying when H_2 was introduced. A diode device that incorporated a SnO_x layer between the intrinsic i-diamond and Pt electrode was reported for detection of O_2 up to 300 °C [119] and later for CO sensing up to 500 °C [120]. Polycrystalline diamond MIS diode with Pd electrode was also reported for detection of benzene (C_6H_6) and toluene (C_7H_8). Sensitivity towards both gases increased with higher temperature, tested up to 250 °C. Higher sensitivity to benzene was attributed to lower activation energy, extracted from Arrhenius plots. Furthermore increasing the thickness of the i-diamond layer improved the diode rectifying characteristics and enhanced benzene detection sensitivity [121]. An interesting PIN diode type CO sensor with Pd/n-SnO_x/i-diamond/p^+-diamond/p^+-Si structure was reported by [122]. The diamond layers were grown using field-enhanced hot-wire CVD technique. The Si substrate was chemically pre-etched in KOH solution to form an array of pyramid-like structures with sharp nanotips. Textured surface sensors had a 12 % higher sensing response to 100 ppm CO compared to those with planar surface due to larger sensing area. Sensors fabricated on single crystal diamond have not been reported until now.

Gallium oxide (Ga_2O_3) is also an emerging WBG semiconductor for various electronics applications. Similarly to SiC, there are 5 known polymorths of Ga_2O_3. The most stable and extensively researched crystal structure is the monoclinic $\beta-Ga_2O_3$ with a melting point at approximately 1800 °C [123]. Resistive type gas sensors for high temperature applications with $\beta-Ga_2O_3$ as the sensing layer have been previously studied for oxygen and reducing gases [124, 125]. Only few reports on Ga_2O_3 based FET type gas sensors have been published thus far. A Pt/Ga_2O_3/SiC MRISiC SBD hydrogen and propane sensor was demostrated by [126]. The 90 nm thick oxide film was deposited on the SiC substrates by sol-gel process and spin coating, followed by annealing in air at 700 °C. The sensors were operated at high temperatures in the range of 300–650 °C and analyte concentrations of 0.06–1 % [127]. The first application of bulk crystalline $\beta-Ga_2O_3$ SBD H_2 sensor was reported by [128]. Substrates with (100) orientation and n-type doping concentration of 5×10^{17} cm^{-3} were used. The sensing Pt electrode was formed on the top and the ohmic contact on the backside. Increasing magitude of response (ΔV) to 200 ppm of H_2 was observed for ramping temperature up to 400 °C. Influence of background O_2 concentration was also studied, indicating that interaction of H_2 and O_2 affected the ΔV. They have also performed a comparitive study of $\beta-Ga_2O_3$ and 4H-SiC SBD H_2 sensors [129]. The $\beta-Ga_2O_3$ diode exhibited much larger ΔV compared to the SiC-based counterpart, especially at H_2 concentrations greater than 100 ppm. This difference was atributed to the presence of oxygen defect sites at the Pt/Ga_2O_3 interface, which provide adsorbtion sites for H atoms. A $\beta-Ga_2O_3$ thin film MESFET with Pt gate was used for H_2 detection by [130]. The 1 µm film was deposited on sapphire substrates by evaporating Ga in oxygen plasma ambient at 600 °C. In the tested temperature range of 400–550 °C the obtained H_2 detection limit was 100 ppm in 20 % O_2/N_2 ambient. Pt/$\beta-Ga_2O_3$ SBD sensors on bulk crystalline $\beta-Ga_2O_3$ substrates with ($\bar{2}$01) and (101) crystal orientations were recently investigated and compared for detection of H_2 [131]. The sensors were tested at room temperature in N_2 background and H_2 concentration range from 500 ppm to 4 %. Devices on ($\bar{2}$01) substrates were found to have 5x higher H_2 sensing response than (101). The observed sensitivity differences were attributed to characteristics of atomic configurations of the two surfaces. The ($\bar{2}$01) surface has 1.5x higher oxygen atom dangling bond density and those act as adsorption sites for hydrogen atoms. No response was observed towards CO, CH_4, CO_2, NO_2 and NH_3 at reported test conditions.

1.6. RESEARCH OBJECTIVE

Promoting broader adoption of chemical and gas sensing technologies across various application areas requires low cost, high volume, highly miniaturized, reliable and low power transducers. Field effect based sensors are highly promising candidates to meet the aforementioned requirements. In addition, operation under harsh environment conditions is essential for manufacturing, energy production and automotive industries. Si-based FETs are limited by maximum operating temperature, as discussed in section 1.5.1, therefore wide-bandgap semiconductors are required. SiC-based SBDs and FETs have been successfully applied as sensors for high temperature sensing (see section 1.5.3). The main drawbacks of SiC sensor technology are the high substrate costs and challenging fabrication, that requires several ion implantation and high temperature annealing steps. Ultra wide-bandgap Ga_2O_3 and diamond technology is in the early stages of processing method development, the substrate supply is limited and very costly.

Gallium nitride (GaN) is a highly promising wide-bandgap material with unique crystal properties. GaN based devices are being extensively studied for next generation power switching, high frequency power amplifier, optoelectronic and to lesser extent sensing applications. While bulk substrates are also costly, it is possible to grow high quality single crystal GaN layers on SiC, sapphire and Si substrates. Furthermore, heterojunction of GaN and AlGaN form highly conductive electron channel that can be utilized for field effect device fabrication.

The focus of this thesis is to develop a gas sensor platform utilizing GaN material system and design, fabricate and test field effect gas sensors. The following objectives need to be completed in order to realize the goals of this work:

1. Select the optimal epitaxial structure and substrate for AlGaN/GaN sensor fabrication.
2. Design and execute AlGaN/GaN HEMT sensor fabrication process flow.
3. Optimize the design of the gas sensing transducer to obtain higher sensing response.
4. Implement gas sensor testing methodology to test gas detection performance in air ambient.
5. Test gas sensor response towards H_2 and H_2S, which are a promising energy source and a toxic industrial pollutant, respectively.
6. Investigate the effects of gate recess on AlGaN/GaN HEMT sensor performance.

1.7. THESIS OUTLINE

The remainder of this thesis is structured as follows:

- **Chapter** 2 focuses on the physics of the GaN FET devices. First the material properties are discussed and the AlGaN/GaN high electron mobility transistor structure and its operating principles are presented. Afterwards, the baseline sensor fabrication process is presented in detail starting with epitaxial material description and finalizing with the chip packaging for gas testing.

- **Chapter** 3 discusses the design parameters and their impact on AlGaN/GaN HEMT sensor characteristics. Photolithograpy mask layout used for sensor fabrication is presented. The impact of sensor sensing electrode geometry on H_2 sensing response is studied. Modifications to the sensor design are made based on obtained results.

- **Chapter** 4 presents the application of Pt-AlGaN/GaN HEMT sensor towards detection of hydrogen sulfide (H_2S). Static and transient sensor response characteristics are studied, the sensing mechanism is discussed and sensing parameters are extracted. The importance of high temperature pre-treatment with H_2 gas, in order to extend the range of detection, is assessed.

- **Chapter** 5 investigates the impact of recessing the barrier layer under the gate electrode on the H_2 sensing characteristics of Pt-AlGaN/GaN HEMT sensor. A method to precisely etch the ultra-thin (several nanometers) AlGaN layer was developed, which involves cyclic oxidation and chemical oxide etching. Sensors with increasing depth of recess are compared in terms static and transient response to the analyte and sensing parameters are determined.

- **Chapter** 6 summarizes the obtained results on the GaN HEMT sensors studied during this research. Afterwards an outlook for related future research is presented in order to advance the adoption of this highly promising sensing technology.

REFERENCES

[1] *The McClean Report: A Complete Analysis and Forecast of the Integrated Circuit Industry,* (2018).

[2] R. Bogue, *Towards the trillion sensors market,* Sensor Review **34**, 137 (2014), https://doi.org/10.1108/SR-12-2013-755 .

[3] J. R. Partington, *Joan Baptista van Helmont,* Annals of Science **1**, 359 (1936), https://doi.org/10.1080/00033793600200291 .

[4] A. J. Ihde, *The development of modern chemistry* (Courier Corporation, 1970).

[5] R. Klockenkämper, A. von Bohlen, and L. Moens, *Analysis of pigments and inks on oil paintings and historical manuscripts using total reflection x-ray fluorescence spectrometry,* X-Ray Spectrometry **29**, 119 (2000).

[6] R. Pandeeswari and B. Jeyaprakash, *Vapour sensing property of metal oxide thin films at ambient condition: Influencing factors: A Review,* Research Journal of Pharmaceutical, Biological and Chemical Sciences **7**, 1221 (2016).

[7] A. Mills, *Humphrey Davy and the safety lamp: the use of metal gauze as a flame barrier,* Physics Education **50**, 673 (2015).

[8] A. B. Lamb, P. W. Carleton, W. S. Hughes, and L. W. Nichols, *The Copper Flame Test for Halogens in Air,* Journal of the American Chemical Society **42**, 78 (1920), https://doi.org/10.1021/ja01446a011 .

[9] J. K. Smart, *History of Chemical and Biological Detectors, Alarms, and Warning Systems,* Memo, U.S. Army, 84th Chemical Battalion, 3rd Chemical Brigade (2000).

[10] B. Kleven, *A Summary of Gas Detection,* Advanced Calibration Designs, Inc (2001).

[11] O. W. Johnson and P. S. Williams, *Combustible gas analysis apparatus,* US Patent, 2023731A (1931).

[12] D. A. MacInnes and M. Dole, *THE BEHAVIOR OF GLASS ELECTRODES OF DIFFERENT COMPOSITIONS,* Journal of the American Chemical Society **52**, 29 (1930), https://doi.org/10.1021/ja01364a005 .

[13] F. W. Dunmore, *An Electric Hygrometer and its Application to Radio-Meteorography,* Bulletin of the American Meteorological Society **19**, 225 (1938).

[14] E. Karrer and R. S. Orr, *A Photoelectric Refractometer,* J. Opt. Soc. Am. **36**, 42 (1946).

[15] P. Hersch, *Galvanic Determination of Traces of Oxygen in Gases,* Nature **169**, 792 (1952).

[16] W. H. Brattain and J. Bardeen, *Surface Properties of Germanium,* Bell System Technical Journal **32**, 1 (1953).

[17] A. Bielański, J. Dereń, and J. Haber, *Electric Conductivity and Catalytic Activity of Semiconducting Oxide Catalysts,* Nature **179**, 668 (1957).

[18] K. Kiukkola and C. Wagner, *Measurements on Galvanic Cells Involving Solid Electrolytes,* Journal of The Electrochemical Society **104**, 379 (1957), http://jes.ecsdl.org/content/104/6/379.full.pdf+html .

[19] J. Weissbart and R. Ruka, *Oxygen gauge,* Review of Scientific Instruments **32**, 593 (1961), https://doi.org/10.1063/1.1717447 .

[20] E. Pungor and E. Hollos-Rokosinyi, *The use of membrane electrodes in the analysis of ionic concentrations,* Acta Chimica Academiae Scientiarum Hungaricae **27**, 63 (1961).

[21] L. C. Clark and C. Lyons, *ELECTRODE SYSTEMS FOR CONTINUOUS MONITORING IN CARDIOVASCULAR SURGERY,* Annals of the New York Academy of Sciences **102**, 29 (1962).

[22] A. Baker, *Improvements in or relating to Electrically Heatable Filaments,* Great Britain Patent **892530** (1962).

[23] T. Seiyama, A. Kato, K. Fujiishi, and M. Nagatani, *A New Detector for Gaseous Components Using Semiconductive Thin Films,* Analytical Chemistry **34**, 1502 (1962), https://doi.org/10.1021/ac60191a001 .

[24] W. H. King, *Piezoelectric Sorption Detector,* Analytical Chemistry **36**, 1735 (1964), https://doi.org/10.1021/ac60215a012 .

[25] N. Taguchi, *Gas-detecting device,* (1971), US Patent US3695848A.

[26] P. Bergveld, *Development of an Ion-Sensitive Solid-State Device for Neurophysiological Measurements,* IEEE Transactions on Biomedical Engineering **BME-17**, 70 (1970).

[27] M. S. Frant, J. W. Ross, and J. H. Riseman, *Electrode indicator technique for measuring low levels of cyanide,* Analytical Chemistry **44**, 2227 (1972), https://doi.org/10.1021/ac60321a038 .

[28] K. Mosbach and B. Danielsson, *An enzyme thermistor,* Biochimica et Biophysica Acta (BBA) - Enzymology **364**, 140 (1974).

[29] K. I. Lundström, M. S. Shivaraman, and C. M. Svensson, *A hydrogen-sensitive Pd-gate MOS transistor,* Journal of Applied Physics **46**, 3876 (1975), https://doi.org/10.1063/1.322185 .

[30] H. Wohltjen and R. Dessy, *Surface acoustic wave probe for chemical analysis. I. Introduction and instrument description,* Analytical Chemistry **51**, 1458 (1979), https://doi.org/10.1021/ac50045a024 .

[31] J. Janata and R. J. Huber, *Chemically Sensitive Field Effect Transistors,* in *Ion-Selective Electrodes in Analytical Chemistry*, edited by H. Freiser (Springer US, Boston, MA, 1980) pp. 107–174.

[32] J. I. Peterson, S. R. Goldstein, R. V. Fitzgerald, and D. K. Buckhold, *Fiber optic pH probe for physiological use,* Analytical Chemistry **52**, 864 (1980), https://doi.org/10.1021/ac50056a022 .

[33] C. Nylander, B. Liedberg, and T. Lind, *Gas detection by means of surface plasmon resonance,* Sensors and Actuators **3**, 79 (1982).

[34] H. Lorenz, M. Peschke, H. Riess, J. Janata, and I. Eisele, *New suspended gate FET technology for physical deposition of chemically sensitive layers,* Sensors and Actuators A: Physical **23**, 1023 (1990).

[35] A. Arbab, A. Spetz, and I. Lundström, *Gas sensors for high temperature operation based on metal oxide silicon carbide (MOSiC) devices,* Sensors and Actuators B: Chemical **15**, 19 (1993).

[36] Z. Gergintschew, P. Kornetzky, and D. Schipanski, *The capacitively controlled field effect transistor (CCFET) as a new low power gas sensor,* Sensors and Actuators B: Chemical **36**, 285 (1996).

[37] H. Svenningstorp, L. Unéus, P. Tobias, I. Lundström, L.-G. Ekedahl, and A. Lloyd Spetz, *High Temperature Gas Sensors Based on Catalytic Metal Field Effect Transistors,* in *Silicon Carbide and Related Materials - 1999*, Materials Science Forum, Vol. 338 (Trans Tech Publications, 2000) pp. 1435–1438.

[38] Y. Cui, Q. Wei, H. Park, and C. M. Lieber, *Nanowire Nanosensors for Highly Sensitive and Selective Detection of Biological and Chemical Species,* Science **293**, 1289 (2001).

[39] J. Schalwig, G. Müller, O. Ambacher, and M. Stutzmann, *Group-III-Nitride Based Gas Sensing Devices,* physica status solidi (a) **185**, 39 (2001).

[40] G. Korotcenkov, in *Handbook of Gas Sensor Materials: Properties, Advantages and Shortcomings for Applications Volume 1: Conventional Approaches* (Springer New York, New York, NY, 2013) pp. 1–45.

[41] J. Hodgkinson and R. P. Tatam, *Optical gas sensing: a review,* Measurement Science and Technology **24**, 012004 (2013).

[42] R. Bogue, *Detecting gases with light: a review of optical gas sensor technologies,* Sensor Review **35**, 133 (2015).

[43] J. Fraden, *Chemical sensors,* in *Handbook of Modern Sensors: Physics, Designs, and Applications* (Springer New York, New York, NY, 2010) pp. 569–606.

[44] International Sensor Technologies, *Electrochemical sensors,* (2018).

[45] J. Janata, *Electrochemical sensors,* in *Principles of Chemical Sensors* (Springer US, Boston, MA, 2009) pp. 99–118.

[46] A. Alassi, M. Benammar, and D. Brett, *Quartz Crystal Microbalance Electronic Interfacing Systems: A Review,* Sensors **17** (2017), 10.3390/s17122799.

[47] G. Sauerbrey, *Verwendung von Schwingquarzen zur Wägung dünner Schichten und zur Mikrowägung,* Zeitschrift für Physik **155**, 206 (1959).

[48] H. Zhang, W. Pang, E. S. Kim, and H. Yu, *Micromachined silicon and polymer probes integrated with film-bulk-acoustic-resonator mass sensors,* Journal of Micromechanics and Microengineering **20**, 125008 (2010).

[49] J. Devkota, P. R. Ohodnicki, and D. W. Greve, *SAW Sensors for Chemical Vapors and Gases,* Sensors **17**, 801 (2017).

[50] A. Mujahid and F. L. Dickert, *Surface Acoustic Wave (SAW) for Chemical Sensing Applications of Recognition Layers,* Sensors **17**, 2716 (2017).

[51] M. Sepaniak, P. Datskos, N. Lavrik, and C. Tipple, *Peer Reviewed: Microcantilever Transducers: A new Approach in Sensor Technology,* Analytical Chemistry **74**, 568 A (2002), https://doi.org/10.1021/ac022156i .

[52] Citytech, *Pellistor schematic,* (2018).

[53] B. Szulczyński and J. Gębicki, *Currently Commercially Available Chemical Sensors Employed for Detection of Volatile Organic Compounds in Outdoor and Indoor Air,* Environments **4**, 21 (2017).

[54] W. Shin, K. Imai, N. Izu, and N. Murayama, *Thermoelectric Thick-Film Hydrogen Gas Sensor Operating at Room Temperature,* Japanese Journal of Applied Physics **40**, L1232 (2001).

[55] M. Schreiter, R. Gabl, J. Lerchner, C. Hohlfeld, A. Delan, G. Wolf, A. Blüher, B. Katzschner, M. Mertig, and W. Pompe, *Functionalized pyroelectric sensors for gas detection,* Sensors and Actuators B: Chemical **119**, 255 (2006).

[56] T. Hübert, L. Boon-Brett, G. Black, and U. Banach, *Hydrogen sensors – A review,* Sensors and Actuators B: Chemical **157**, 329 (2011).

[57] R. P. Kovacich, N. A. Martin, M. G. Clift, C. Stocks, I. Gaskin, and J. Hobby, *Highly accurate measurement of oxygen using a paramagnetic gas sensor,* Measurement Science and Technology **17**, 1579 (2006).

[58] M. Fleischer, *Advances in application potential of adsorptive-type solid state gas sensors: high-temperature semiconducting oxides and ambient temperature GasFET devices,* Measurement Science and Technology **19**, 042001 (2008).

[59] H. Shen, L. Li, and D. Xu, *Preparation of one-dimensional* SnO_2*–*In_2O_3 *nano-heterostructures and their gas-sensing property,* RSC Adv. **7**, 33098 (2017).

[60] B. Raman, D. C. Meier, J. K. Evju, and S. Semancik, *Designing and optimizing microsensor arrays for recognizing chemical hazards in complex environments,* Sensors and Actuators B: Chemical **137**, 617 (2009).

[61] J. F. McAleer, P. T. Moseley, J. O. W. Norris, and D. E. Williams, *Tin dioxide gas sensors. part 1.—aspects of the surface chemistry revealed by electrical conductance variations,* J. Chem. Soc., Faraday Trans. 1 **83**, 1323 (1987).

[62] M. Toohey, *Electrodes for nanodot-based gas sensors,* Sensors and Actuators B: Chemical **105**, 232 (2005).

[63] X. Vilanova, E. Llobet, J. Brezmes, J. Calderer, and X. Correig, *Numerical simulation of the electrode geometry and position effects on semiconductor gas sensor response,* Sensors and Actuators B: Chemical **48**, 425 (1998).

[64] A. B. Gadkari, T. J. Shinde, and P. N. Vasambekar, *Ferrite Gas Sensors,* IEEE Sensors Journal **11**, 849 (2011).

[65] G. Korotcenkov and B. Cho, *Metal oxide composites in conductometric gas sensors: Achievements and challenges,* Sensors and Actuators B: Chemical **244**, 182 (2017).

[66] Y.-F. Sun, S.-B. Liu, F.-L. Meng, J.-Y. Liu, Z. Jin, L.-T. Kong, and J.-H. Liu, *Metal Oxide Nanostructures and Their Gas Sensing Properties: A Review,* Sensors **12**, 2610 (2012).

[67] X. Liu, T. Ma, N. Pinna, and J. Zhang, *Two-Dimensional Nanostructured Materials for Gas Sensing,* Advanced Functional Materials **27**, 1702168 (2017).

[68] B. D. Kay, C. H. F. Peden, and D. W. Goodman, *Kinetics of hydrogen absorption by Pd(110),* Phys. Rev. B **34**, 817 (1986).

[69] R. Duś, R. Nowakowski, and E. Nowicka, *Chemical and structural components of work function changes in the process of palladium hydride formation within thin Pd film,* Journal of Alloys and Compounds **404-406**, 284 (2005).

[70] E. Lee, J. M. Lee, J. H. Koo, W. Lee, and T. Lee, *Hysteresis behavior of electrical resistance in Pd thin films during the process of absorption and desorption of hydrogen gas,* International Journal of Hydrogen Energy **35**, 6984 (2010).

[71] E. Lee, J. M. Lee, E. Lee, J.-S. Noh, J. H. Joe, B. Jung, and W. Lee, *Hydrogen gas sensing performance of Pd–Ni alloy thin films,* Thin Solid Films **519**, 880 (2010).

[72] G. Korotcenkov, *Polymers,* in *Handbook of Gas Sensor Materials: Properties, Advantages and Shortcomings for Applications Volume 1: Conventional Approaches* (Springer New York, New York, NY, 2013) pp. 117–152.

[73] A. J. Heeger, *Semiconducting and Metallic Polymers: The Fourth Generation of Polymeric Materials,* The Journal of Physical Chemistry B **105**, 8475 (2001).

[74] H. Bai and G. Shi, *Gas Sensors Based on Conducting Polymers,* Sensors **7**, 267 (2007).

[75] T. Ishihara and S. Matsubara, *Capacitive Type Gas Sensors,* Journal of Electroceramics **2**, 215 (1998).

[76] P. L. Kebabian and A. Freedman, *Fluoropolymer-based capacitive carbon dioxide sensor,* Measurement Science and Technology **17**, 703 (2006).

[77] A. M. Kummer, A. Hierlemann, and H. Baltes, *Tuning Sensitivity and Selectivity of Complementary Metal Oxide Semiconductor-Based Capacitive Chemical Microsensors,* Analytical Chemistry **76**, 2470 (2004).

[78] D. Neamen, *Semiconductor Physics And Devices* (McGraw-Hill Education, 2011).

[79] S. Dimitrijev, *Principles of Semiconductor Devices,* Oxford series in electrical and computer engineering (Oxford University Press, 2012).

[80] J. Janata, *Apparatus and method for measuring the concentration of components in fluids,* (1983), US Patent 4,411,741.

[81] C. Senft, P. Iskra, and I. Eisele, *Theory and Application of Suspended Gate FET Gas Sensors,* in *Solid State Gas Sensors - Industrial Application*, edited by M. Fleischer and M. Lehmann (Springer Berlin Heidelberg, Berlin, Heidelberg, 2012) pp. 79–112.

[82] I. Eisele, T. Doll, and M. Burgmair, *Low power gas detection with FET sensors,* Sensors and Actuators B: Chemical **78**, 19 (2001).

[83] Z. Gergintschew, P. Kornetzky, and D. Schipanski, *The capacitively controlled field effect transistor (CCFET) as a new low power gas sensor,* Sensors and Actuators B: Chemical **36**, 285 (1996).

[84] R. P. Gupta, Z. Gergintschew, D. Schipanski, and P. Vyas, *New gas sensing properties of high Tc cuprates,* Sensors and Actuators B: Chemical **56**, 65 (1999).

[85] M. Burgmair, M. Zimmer, and I. Eisele, *Humidity and temperature compensation in work function gas sensor FETs,* Sensors and Actuators B: Chemical **93**, 271 (2003).

[86] M. Burgmair, H.-P. Frerichs, M. Zimmer, M. Lehmann, and I. Eisele, *Field effect transducers for work function gas measurements: device improvements and comparison of performance,* Sensors and Actuators B: Chemical **95**, 183 (2003).

[87] C. Kim, I. Cho, J. Shin, K. Choi, J. Lee, and J. Lee, *A New Gas Sensor Based on MOSFET Having a Horizontal Floating-Gate,* IEEE Electron Device Letters **35**, 265 (2014).

[88] M. Wu, C.-H. Kim, J. Shin, Y. Hong, X. Jin, and J.-H. Lee, *Effect of a pre-bias on the adsorption and desorption of oxidizing gases in FET-type sensor,* Sensors and Actuators B: Chemical **245**, 122 (2017).

[89] Y. Hong, C.-H. Kim, J. Shin, K. Y. Kim, J. S. Kim, C. S. Hwang, and J.-H. Lee, *Highly selective ZnO gas sensor based on MOSFET having a horizontal floating-gate,* Sensors and Actuators B: Chemical **232**, 653 (2016).

[90] F. S. Shoucair, *Scaling, Subthreshold, and Leakage Current Matching Characteristics in High-Temperature (*25 °C-250 °C*) VLSI CMOS devices,* IEEE Transactions on Components, Hybrids, and Manufacturing Technology **12**, 780 (1989).

[91] M. Yousuf, B. Kuliyev, B. Lalevic, and T. Poteat, *Pd-InP Schottky diode hydrogen sensors,* Solid-State Electronics **25**, 753 (1982).

[92] L. M. Lechuga, A. Calle, D. Golmayo, P. Tejedor, and F. Briones, *A New Hydrogen Sensor Based on a Pt/GaAs Schottky Diode,* Journal of The Electrochemical Society **138**, 159 (1991).

[93] W.-C. Liu, H.-J. Pan, H.-I. Chen, K.-W. Lin, and C.-K. Wang, *Comparative Hydrogen-Sensing Study of Pd/GaAs and Pd/InP Metal-Oxide-Semiconductor Schottky Diodes,* Japanese Journal of Applied Physics **40**, 6254 (2001).

[94] L. Lechuga, A. Calle, D. Golmayo, and F. Briones, *Different catalytic metals (Pt, Pd and Ir) for GaAs Schottky barrier sensors,* Sensors and Actuators B: Chemical **7**, 614 (1992).

[95] M. Jaegle and K. Steiner, *Gas-sensitive GaAs-MESFETs,* Sensors and Actuators B: Chemical **34**, 543 (1996).

[96] K.-W. Lin, C.-C. Cheng, S.-Y. Cheng, K.-H. Yu, C.-K. Wang, H.-M. Chuang, J.-Y. Chen, C.-Z. Wu, and W.-C. Liu, *A novel Pd/oxide/GaAs metal-insulator-semiconductor field-effect transistor (MISFET) hydrogen sensor,* Semiconductor Science and Technology **16**, 997 (2001).

[97] W.-C. Liu, K.-W. Lin, H.-I. Chen, C.-K. Wang, C.-C. Cheng, S.-Y. Cheng, and C.-T. Lu, *A new Pt/oxide/*$In_{0.49}Ga_{0.51}P$ *MOS Schottky diode hydrogen sensor,* IEEE Electron Device Letters **23**, 640 (2002).

[98] C.-T. Lu, K.-W. Lin, H.-I. Chen, H.-M. Chuang, C.-Y. Chen, and W.-C. Liu, *A new Pd-oxide-*$Al_{0.3}Ga_{0.7}As$ *MOS hydrogen sensor,* IEEE Electron Device Letters **24**, 390 (2003).

[99] Y.-Y. Tsai, C.-W. Hung, S.-I. Fu, P.-H. Lai, H.-I. Chen, and W.-C. Liu, *On the Hydrogen Sensing Properties of a Pt-Oxide-* $In_{0.5}Al_{0.5}P$ *Schottky Diode,* Electrochemical and Solid-State Letters **9**, H108 (2006), http://esl.ecsdl.org/content/9/11/H108.full.pdf+html .

[100] C. Hung, H. Lin, H. Chen, Y. Tsai, P. Lai, S. Fu, and W. Liu, *A Novel Pt/*$In_{0.52}Al_{0.48}As$ *Schottky Diode-Type Hydrogen Sensor,* IEEE Electron Device Letters **27**, 951 (2006).

[101] C.-C. Cheng, Y.-Y. Tsai, K.-W. Lin, H.-I. Chen, W.-H. Hsu, C.-W. Hong, and W.-C. Liu, *Characteristics of a Pd–oxide–*$In_{0.49}Ga_{0.51}P$ *high electron mobility transistor (HEMT)-based hydrogen sensor,* Sensors and Actuators B: Chemical **113**, 29 (2006).

[102] C.-C. Cheng, Y.-Y. Tsai, K.-W. Lin, H.-I. Chen, W.-H. Hsu, C.-W. Hung, R.-C. Liu, and W.-C. Liu, *Pd-oxide-* $Al_{0.24}Ga_{0.76}As$ *(MOS) high electron mobility transistor (HEMT)-based hydrogen sensor,* IEEE Sensors Journal **6**, 287 (2006).

[103] T.-H. Tsai, H.-I. Chen, C.-F. Chang, P.-S. Chiu, Y.-C. Liu, L.-Y. Chen, T.-P. Chen, and W.-C. Liu, *Hydrogen sensing properties of a metamorphic high electron mobility transistor,* Applied Physics Letters **94**, 012102 (2009).

[104] T.-H. Tsai, H.-I. Chen, T.-Y. Chen, L.-Y. Chen, Y.-J. Liu, C.-C. Huang, K.-S. Hsu, and W.-C. Liu, *Hydrogen sensing properties of a Pd/oxide/InAlAs metamorphic-based transistor,* International Journal of Hydrogen Energy **35**, 3903 (2010).

[105] W. Choyke and G. Pensl, *Physical Properties of SiC,* MRS Bulletin **22**, 25–29 (1997).

[106] G. W. Hunter, P. G. Neudeck, G. Jefferson, G. Madzsar, C. Liu, and Q. Wu, *The development of hydrogen sensor technology at NASA Lewis Research Center,* 4th Annual Space System Health Management Technology Conference (1993).

[107] A. Baranzahi, A. L. Spetz, P. Tobias, I. Lundström, P. Mårtensson, M. Glavmo, A. Göras, J. Nytomt, P. Salomonsson, and H. Larsson, *Fast Responding Air/Fuel Sensor for Individual Cylinder Combustion Monitoring,* in *SAE Technical Paper* (SAE International, 1997).

[108] A. L. Spetz, D. Schmeißer, A. Baranzahi, B. Wälivaara, W. Göpel, and I. Lundström, *X-ray photoemission and Auger electron spectroscopy analysis of fast responding activated metal oxide silicon carbide gas sensors,* Thin Solid Films **299**, 183 (1997).

[109] S. Savage, A. O. Konstantinov, A. Saroukhan, and C. I. Harris, *High Temperature 4H-SiC FET for Gas Sensing Applications,* in *Silicon Carbide and Related Materials - 1999*, Materials Science Forum, Vol. 338 (Trans Tech Publications, 2000) pp. 1431–1434.

[110] A. Samman, S. Gebremariam, L. Rimai, X. Zhang, J. Hangas, and G. Auner, *Silicon-carbide MOS capacitors with laser-ablated Pt gate as combustible gas sensors,* Sensors and Actuators B: Chemical **63**, 91 (2000).

[111] A. Samman, S. Gebremariam, L. Rimai, X. Zhang, J. Hangas, and G. W. Auner, *Platinum–aluminum nitride–silicon carbide diodes as combustible gas sensors,* Journal of Applied Physics **87**, 3101 (2000), https://doi.org/10.1063/1.372305 .

[112] S. Roy, A. Salomonsson, A. L. Spetz, C. Aulin, P.-O. Käll, L. Ojamäe, M. Strand, and M. Sanati, *Metal Oxide Nanoparticles as Novel Gate Materials for Field-Effect Gas Sensors,* Materials and Manufacturing Processes **21**, 275 (2006), https://doi.org/10.1080/10426910500464651 .

[113] M. Ali, V. Cimalla, V. Lebedev, T. Stauden, G. Ecke, V. Tilak, P. Sandvik, and O. Ambacher, *SiC-based FET for detection of* NO_x *and* O_2 *using* $InSnO_x$ *as a gate material,* Sensors and Actuators B: Chemical **122**, 182 (2007).

[114] A. Trinchi, K. Galatsis, W. Wlodarski, and Y. X. Li, *A Pt/*Ga_2O_3*-ZnO/SiC Schottky diode-based hydrocarbon gas sensor,* IEEE Sensors Journal **3**, 548 (2003).

[115] A. Trinchi, S. Kandasamy, and W. Wlodarski, *High temperature field effect hydrogen and hydrocarbon gas sensors based on SiC MOS devices,* Sensors and Actuators B: Chemical **133**, 705 (2008).

[116] M. T. Soo, K. Y. Cheong, and A. F. M. Noor, *Advances of SiC-based MOS capacitor hydrogen sensors for harsh environment applications,* Sensors and Actuators B: Chemical **151**, 39 (2010).

[117] M. Andersson, R. Pearce, and A. L. Spetz, *New generation SiC based field effect transistor gas sensors,* Sensors and Actuators B: Chemical **179**, 95 (2013).

[118] W. P. Kang, Y. Gurbuz, J. L. Davidson, and D. V. Kerns, *A New Hydrogen Sensor Using a Polycrystalline Diamond-Based Schottky Diode,* Journal of The Electrochemical Society **141**, 2231 (1994), http://jes.ecsdl.org/content/141/8/2231.full.pdf+html .

[119] Y. Gurbuz, W. Kang, J. Davidson, and D. Kerns, *A novel oxygen gas sensor utilizing thin film diamond diode with catalyzed tin oxide electrode,* Sensors and Actuators B: Chemical **36**, 303 (1996).

[120] Y. Gurbuz, W. Kang, J. Davidson, and D. Kerns, *High-temperature tolerant diamond diode for carbon monoxide gas detection,* Journal of applied physics **84**, 6935 (1998).

[121] Y. Gurbuz, W. P. Kang, J. L. Davidson, and D. V. Kerns, *Diamond microelectronic gas sensor for detection of benzene and toluene,* Sensors and Actuators B: Chemical **99**, 207 (2004).

[122] F. Juang, H. Chiu, Y. Fang, K. Cho, and Y. Chen, *An n-*SnO_x*/i-Diamond/p-Diamond Diode With Nanotip Structure for High-Temperature CO Sensing Applications,* IEEE Transactions on Electron Devices **59**, 1786 (2012).

[123] S. J. Pearton, J. Yang, P. H. Cary, F. Ren, J. Kim, M. J. Tadjer, and M. A. Mastro, *A review of Ga_2O_3 materials, processing, and devices,* Applied Physics Reviews **5**, 011301 (2018).

[124] M. Fleischer and H. Meixner, *Gallium oxide thin films: A new material for high-temperature oxygen sensors,* Sensors and Actuators B: Chemical **4**, 437 (1991).

[125] M. Fleischer and H. Meixner, *Improvements in Ga_2O_3 sensors for reducing gases,* Sensors and Actuators B: Chemical **13**, 259 (1993).

[126] A. Trinchi, W. Wlodarski, and Y. Li, *Hydrogen sensitive GA2O3 Schottky diode sensor based on SiC,* Sensors and Actuators B: Chemical **100**, 94 (2004).

[127] A. Trinchi, W. Wlodarski, Y. X. Li, G. Faglia, and G. Sberveglieri, *Pt/Ga_2O_3/SiC MRISiC devices: a study of the hydrogen response,* Journal of Physics D: Applied Physics **38**, 754 (2005).

[128] S. Nakagomi, M. Kaneko, and Y. Kokubun, *Hydrogen Sensitive Schottky Diode Based on $\beta-Ga_2O_3$ Single Crystal,* Sensor Letters **9**, 31 (2011).

[129] S. Nakagomi, M. Ikeda, and Y. Kokubun, *Comparison of Hydrogen Sensing Properties of Schottky Diodes Based on SiC and $\beta-Ga_2O_3$ Single Crystal,* Sensor Letters **9**, 616 (2011).

[130] S. Nakagomi, T. Sai, and Y. Kokubun, *Hydrogen gas sensor with self temperature compensation based on $\beta-Ga_2O_3$ thin film,* Sensors and Actuators B: Chemical **187**, 413 (2013).

[131] S. Jang, S. Jung, J. Kim, F. Ren, S. J. Pearton, and K. H. Baik, *Hydrogen Sensing Characteristics of Pt Schottky Diodes on ($\bar{2}01$) and (010) Ga_2O_3 Single Crystals,* ECS Journal of Solid State Science and Technology **7**, Q3180 (2018).

2

GaN sensor technology and fabrication

Gallium nitride is a highly promising semiconductor for future microelectronic devices. This chapter discuses the GaN material properties, the device physics and operating principles AlGaN/GaN HEMTs. Afterwards the HEMT based sensor structure is introduced and an overview of previously reported GaN-based gas sensors is given. The remainder of the chapter is dedicated to the development of sensor microfabrication process in a university cleanroom. This includes the selection of starting epitaxial structure and device isolation. Afterwards, the formation of low resistance ohmic contacts is investigated, including the metal stack selection, optimization of high temperature annealing conditions and electrical characterization. Then gate electrode patterning is discussed followed by interconnection layer processing, sensor passivation and finally chip dicing and packaging.

2.1. GaN MATERIAL PROPERTIES

2.1.1. PHYSICAL AND ELECTRICAL PROPERTIES OF GaN

Si technology reached maturity some years ago and it is predicted that the next generation of high power switches are going to be implemented using GaN and SiC. The wide-bandgap, high critical electric field and saturation velocity of GaN are advantageous for reducing switching losses and enhancing efficiency. The main properties of GaN are listed and compared with Si and other semiconductors in table 2.1.

The critical electric field of GaN is one order higher than of Si, which means it can sustain much larger bias voltages or have a ~10x lower device footprint for the equivalent breakdown voltage rating. The high electron saturation velocity combined with rather high electron mobility is critical for very high switching frequency power amplifiers.

The wide-bandgap of GaN is of critical importance for FET-type gas sensor applications. The low intrinsic carrier density enables reliable operation at high temperatures significantly above 200 °C to extend the range of detectable analytes and shorten the reaction times. Good thermal conductivity also aids high temperature operation as resistive heat is dissipated more effectively. Sensing in harsh environments requires chemical stability, which in the case of GaN has been demostrated by resistance to most known wet etchants even at elevated temperatures [4]. The chemical as well as radiation resistance is attributed to the wide-bandgap and strong chemical bonds of GaN.

An exceptional feature of GaN is the ability to form alloys such as like $Al_xGa_{1-x}N$ and $In_xGa_{1-x}N$ which allows to tune the bandgap in the 0.7–6.2 eV range. The AlGaN/GaN heterojunction is necessary to form the electron channel, known as two dimensional

Table 2.1: Material properties of GaN compared to Si and other semiconductors [1–3].

Property	**Si**	**GaAs**	**4H-SiC**	**GaN**	**$\beta-Ga_2O_3$**	**Diamond**
Bandgap (eV)	1.12	1.42	3.26	3.42	4.85	5.47
Dielectric constant	11.8	12.8	9.7	9	10	5.5
Critical electric field (MV/cm)	0.3	0.4	3	3.3	8	10
Electron mobility (cm^2/Vs)	1500	8400	800	1000	300	2000
Saturation velocity (10^7 cm/s)	1	1.3	2	2.5	2	2
Thermal conductivity (W/cm K)	1.5	0.5	4.9	2.5	0.3	20
Intrinsic carrier concentration (cm^{-3})	1.5×10^{10}	1.8×10^6	8.2×10^{-9}	1.7×10^{-10}	1.8×10^{-22}	1×10^{-26}

electron gas (2DEG) with high electron mobility up to 2000 $\mathrm{cm}^2/\mathrm{Vs}$ (see section 2.1.3).

2.1.2. III-N SEMICONDUCTOR CRYSTAL STRUCTURE

Gallium nitride (GaN) along with AlN and InN are binary group III nitride semiconductors. These materials can crystallize into zincblende (ZB), wurtzite (WZ) and rocksalt (RS) crystal structures as shown in fig. 2.1 [5]. GaN of the wurtzite polytype is the most thermodynamically stable under normal ambient conditions and therefore widely applied for device fabrication. In this structure each cation (i.e. Ga, Al, In) atom is bonded to 4 equidistant anion (N) atoms, and vice versa, in a tetrahedral arrangement, as shown in fig. 2.2a.

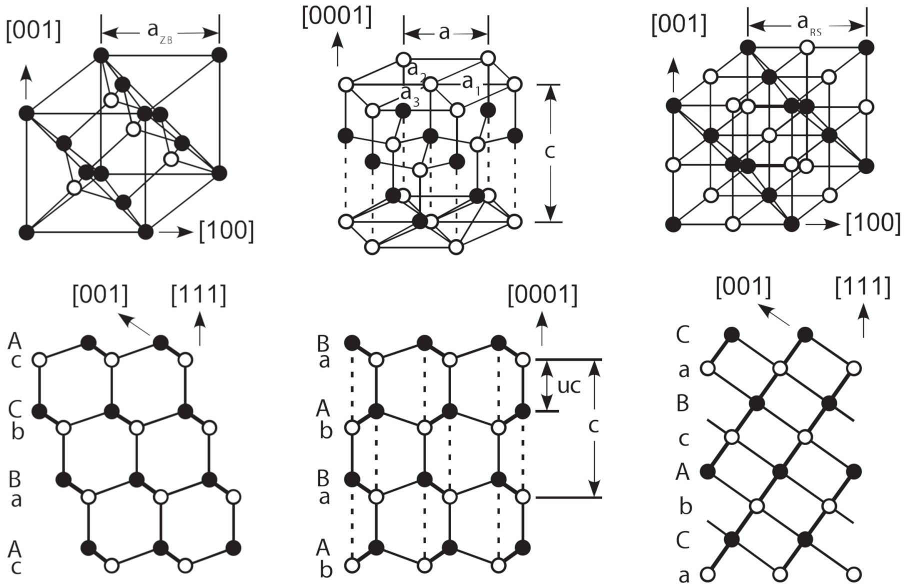

(a) (b) (c)

Figure 2.1: Zincblende (a), wurtzite (b) and rocksalt (c) crystal structures. Full circles represent cations and open circles–anions [5].

Wurtzite crystals belong to hexagonal crystal family and hence have two lattice constants (see fig. 2.1b) i.e. the base side length constant a and the unit cell height c. The ideal lattice constant ratio of a WZ cell is $c/a = \sqrt{8/3} = 1.633$. The wurtzite structure consists of two interpenetrating hexagonal close-packed (hcp) sublattices, with one type of atom each and offset by the anion-cation bond length u along the [0001] direction or c-axis. The crystal is made up of alternating layers of close-packed group III metal atoms and nitrogen atoms, therefore the stacking sequence is AaBbAa in the [0001] direction

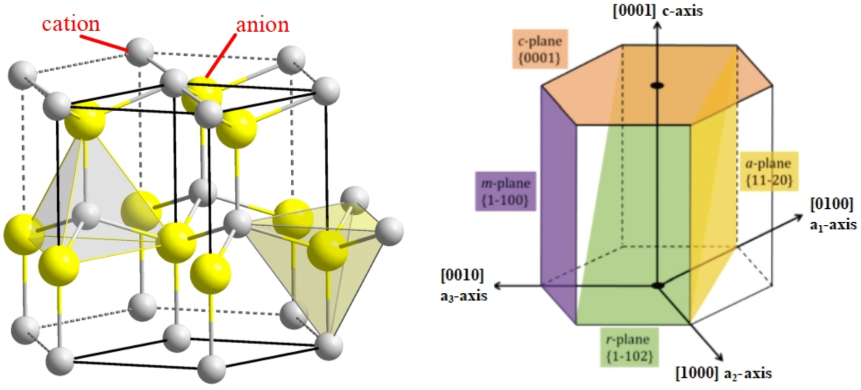

(a) (b)

Figure 2.2: Lattice structure of wurtzite crystal with the tetrahedral bonds shown with intersecting planes (a). Schematic representation of a-, m-, c- and r-planes of a wurtzite crystal (b).

(fig. 2.1b bottom). To obtain highest quality material of WZ GaN, crystal growth is commonly done perpendicular to the polar c-plane fig. 2.2b, while growth along non-polar a-plane and m-plane or the semi-polar r-plane is more challenging and results in lower quality films.

The chemical bonds of compound semiconductors are of mixed covalent-ionic character because of the electronegativity differences of bonded atoms, which leads to dipole formation between, for example Ga and As or Ga and N. Bond ionicity of III-N semiconductors is more pronounced due to large electronegativity of nitrogen. Zincblende crystals, such as GaAs, are centrosymmetric, therefore each dipole is cancelled out by a dipole of another bond. Wurtzite structure is non-centrosymetric along the c-axis, which results in net polarization parallel to this axis, called spontaneous polarization P_{SP} as it is present without applying any external strain or stress. The magnitude of P_{SP} depends on the c/a ratio. There is electrostactic attraction between anions and cations indicated by dashed lines in fig. 2.1b, hence experimental data of GaN obtained c/a=1.6296, resulting in P_{SP}=−0.029 C/m^2, while P_{SP}=−0.018 C/m^2 for ideal $c/a = \sqrt{8/3}$ [6].

2.1.3. PHYSICS OF ALGAN/GAN HETEROSTRUCTURE

GaN grown in the c-axis direction exhibits polarization effects due to lack of inversion symmetry and therefore there exist two distinct polarities of epitaxially grown films. By convention, starting from the substrate, if the parallel bonds are pointing from the Ga atoms towards the N atoms, the crystal is of [0001] orientation, or Ga-face (fig. 2.3). If the bonds are instead pointing from N to Ga atoms the polarity [000$\bar{1}$] or N-face. Crystal ori-

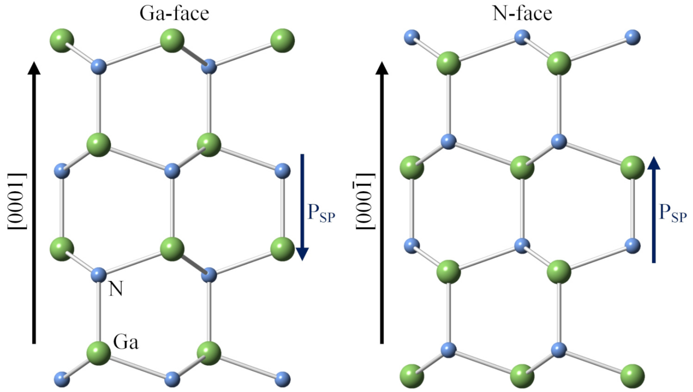

Figure 2.3: Schematic diagram of wurtzite GaN with Ga-face and N-face crystal polarity.

entation is a bulk property, which means that whether the surface is terminated with Ga or N atoms does not impact the polarity [7]. The polarity of GaN films can be controlled by the growth technique, substrate selection, surface treatment and insertion of interfacial layers. The polarity of GaN has profound impact on device fabrication and characteristics. Ga-face surfaces typically have lower surface roughness and higher chemical inertness. The spontaneous polarization vector is parallel to the c-axis and is directed from the anion towards the cation, which in the case of Ga-polarity (see fig. 2.3) results in net positive charge ($+\sigma$) on the N-face and negative charge ($-\sigma$) on the Ga-face.

The ability to form alloys such as $Al_xGa_{1-x}N$ and grow AlGaN/GaN heterojuctions is a requisite for enhancing the performance of numerous III-V devices such as LEDs, SBDs and high electron mobility transistors (HEMTs). The alloy composition in terms of Al incorporation alters the lattice constants a and c according to Vegard's law:

$$a_{Al_xGa_{1-x}N} = 3.189 - 0.077x \text{ [Å]} \tag{2.1}$$

and

$$c_{Al_xGa_{1-x}N} = 5.185 - 0.203x \text{ [Å]} \tag{2.2}$$

where x is the Al mole fraction. The bandgap also depends on the alloy composition, expressed as:

$$E_g(x) = xE_{g(AlN)} + (1-x)E_{g(GaN)} - bx(1-x) \text{ [eV]} \tag{2.3}$$

where b is the bowing parameter, which depends on material quality. The variation of E_g versus a and Al % in AlGaN alloy is shown in fig. 2.4. The magnitude of spontaneous

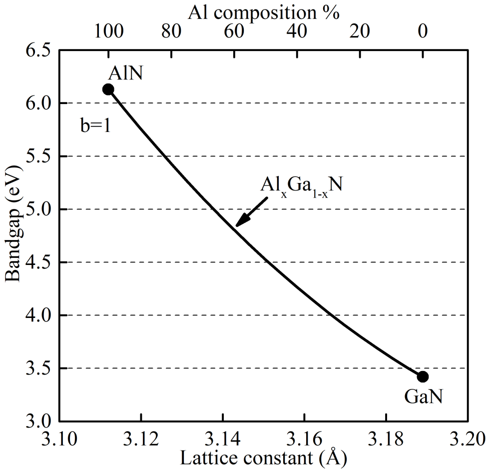

Figure 2.4: Variation of bandgap versus lattice constant and Al incorporation of AlGaN alloy.

polarization in AlGaN is also composition dependent:

$$P_{SP}(x) = -0.052x - 0.029\ [\mathrm{C/m^2}] \tag{2.4}$$

The AlGaN/GaN heterostructure of HEMTs is typically formed by growing a Ga-face 1–5 µm GaN buffer layer on a foreign substrate, followed by a 10–30 nm pseudomorphic AlGaN barrier layer. As the lattice constant a of AlGaN is smaller than GaN, the grown film is under tensile strain and additionally exhibits piezoelectric polarization (P_{PE}) parallel to spontaneous polarization as shown in fig. 2.5. The magnitude of piezoelectric

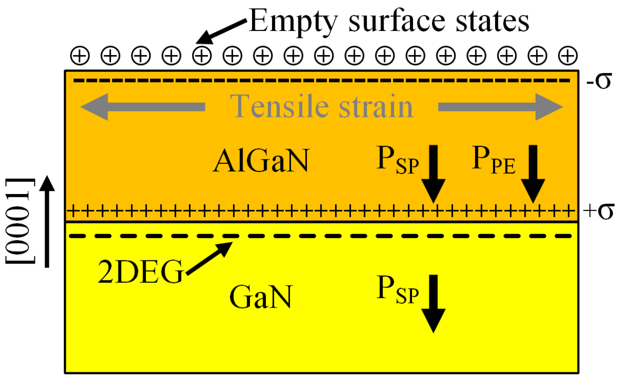

Figure 2.5: Orientation of polarization vectors at the Ga-face AlGaN/GaN heterostructure with AlGaN under tensile strain. Polarization induced charges (σ) are also indicated.

polarization in the strained AlGaN is expressed as:

$$P_{PE}(x) = 2\frac{a(0) - a(x)}{a(x)}\left(e_{31}(x) - e_{33}(x)\frac{C_{13}(x)}{C_{33}(x)}\right) \tag{2.5}$$

where $a(0)$ and $a(x)$ are the lattice constants of the GaN buffer and relaxed barrier layer from eq. (2.1), respectively, $e_{31}(x)$, $e_{33}(x)$ and $C_{13}(x)$, $C_{33}(x)$ are the Al % dependent piezoelectric coefficients and elastic constants [8]. The P_{PE} of tensile strained AlGaN is negative because $a > a_0$ and $\left[e_{31}(x) - e_{33}(x)\frac{C_{13}(x)}{C_{33}(x)}\right] < 0$ for the whole range of mole fractions. Due to differences in polarization values of the barrier and buffer layers a net fixed charge is present at the interface. This sheet charge density can be expressed as:

$$|\sigma(x)| = P_{AlGaN} - P_{GaN} = P_{SP}(x) + P_{PE}(x) - P_{SP}(0) \tag{2.6}$$

For a Ga-face AlGaN/GaN junction the polarization charge at the interface is positive ($\sigma+$). To compensate for the $\sigma+$, electrons will flow to and accumulate at the interface forming the 2DEG, confined in a triangular quantum well, as evident from the band diagram in fig. 2.6. The electron sheet carrier density at the interface can be estimated

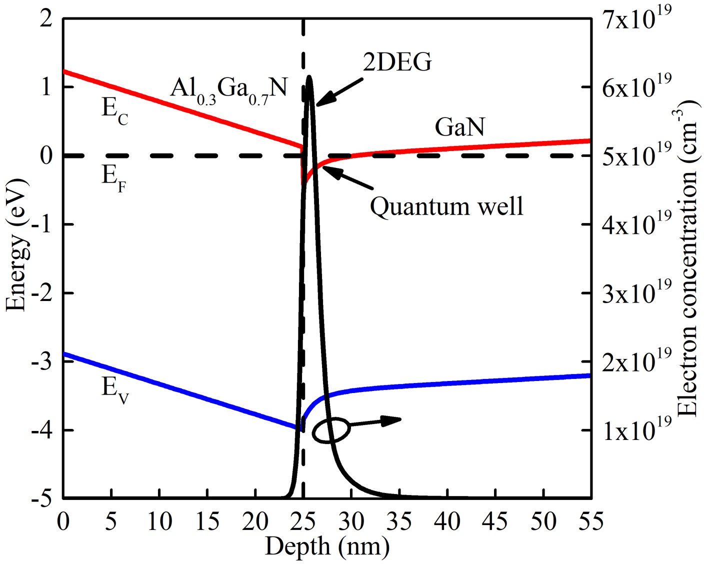

Figure 2.6: Simulated energy band diagram of AlGaN/GaN heterostructure and electron concentration profile.

according to:

$$n_s(x) = \frac{+\sigma(x)}{e} - \left(\frac{\epsilon_0\epsilon(x)}{de^2}\right)[e\phi_b(x) + E_F(x) - \Delta E_C(x)] \tag{2.7}$$

where d is the thickness of AlGaN barrier, $\epsilon(x)$ is the dielectric constant, $e\phi_b(x)$ is the Schottky barrier height of the gate contact, $E_F(x)$ is the Fermi level with respect to GaN conduction band edge and $\Delta E_C(x)$ is the conduction band offset at the AlGaN/GaN interface. The n_s increases with larger thickness of the barrier layer and Al incorporation. Increasing the barrier thickness too much will however result in strain relaxation while high Al% will cause excessive lattice mismatch both of which negatively impact device reliability [9].

As the AlGaN/GaN heterojunctions are frequently grown without any intentional doping, the origin of electrons in the 2DEG was not immediately understood. The current widely accepted explanation is that electrons are supplied from donor-like surface states (or traps), which are neutral when occupied with an electron and positively charged when empty [10]. It is considered that these surface states are below the conduction band (E_C) edge. The traps are neutral if they are below the Fermi level (E_F), which is the case when the AlGaN barrier is less than the critical thickness and 2DEG=0. As the barrier is grown thicker the donor states energy reaches the E_F. The electrons are then transferred to the junction interface by the polarization induced electric field. These electrons then fill the triangular quantum well and form the 2DEG, while the empty surface states screen the surface $-\sigma$ and the dipole induced field [11].

2.2. GaN HEMT-based sensors

2.2.1. AlGaN/GaN HEMT operating principle

The first AlGaN/GaN HEMT utilizing the 2DEG as conductive channel was reported by Khan et al. [12]. The schematic structure of a HEMT is shown in fig. 2.7. Like other FETs, it is a 3 terminal device. When a bias voltage is applied between the ohmic source and drain contacts current flows through the device along the 2DEG. The magnitude of the drain current is controlled by the voltage applied to the Schottky gate terminal (V_{GS}).

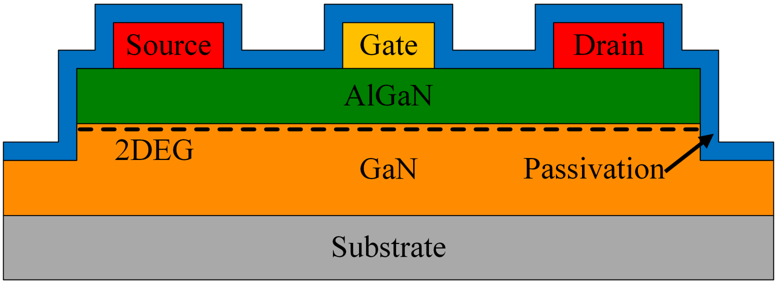

Figure 2.7: Schematic of a AlGaN/GaN high electron mobility transistor (HEMT).

Individual devices are separated by cutting of the 2DEG outside of the active area using plasma etching or ion implantation.

At gate bias of $V_{GS} = 0\,\mathrm{V}$ the 2DEG density is high and large current can flow through the transistor. Applying negative V_{GS} with increasing magnitude causes the extension of a depletion region under the gate electrode. The density of 2DEG gradually reduces until it is completely pinched-off when threshold voltage is reached, $V_{GS} = V_{TH}$. The typical AlGaN/GaN HEMT is therefore a depletion mode device. The effect of gate bias on the sheet carrier density can be expressed by modifying eq. (2.7):

$$n_s(x) = \frac{+\sigma(x)}{e} - \left(\frac{\epsilon_0\epsilon(x)}{de^2}\right)[e(\phi_b(x) - V_{GS}) + E_F(x) - \Delta E_C(x)] \tag{2.8}$$

2.2.2. GaN-based gas sensors

Sensors based on AlGaN/GaN heterostructure are shown in fig. 2.8. The most commonly utilized structures are the HEMT and the Schottky barrier diode. Lateral designs are typical to take advantage of the 2DEG channel. The main structural difference of a AlGaN/GaN-sensor compared to a HEMT is the gate electrode. While the ohmic electrodes are covered by a passivation layer, the gate/anode surface of the sensor must be exposed to the ambient in order directly interact with any analyte present. The sensing electrode is made of gas reactive material i.e. catalytic metal or reactive metal oxide. The morphology and thickness of the gate is also important in sensing applications.

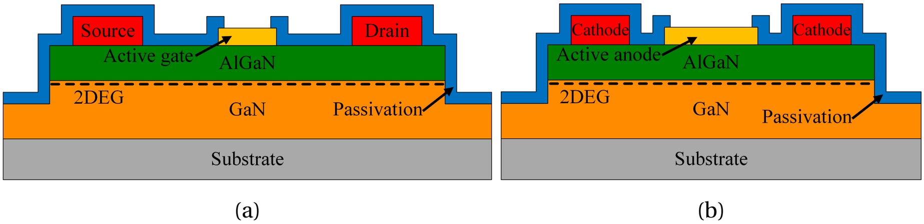

(a) (b)

Figure 2.8: Schematic of AlGaN/GaN based sensor structures: (a) HEMT and (b) SBD.

The first GaN based field effect sensor was demonstrated by Luther [13]. It was a lateral n-GaN Schottky diode with a Pt anode. GaN was grown on sapphire wafer by HVPE. Sensing response towards H_2 and propane (C_3H_8) in Ar background at temperatures of 200–400 °C was tested. H_2 was detected down to 2.5 ppm at 200 °C and response to 0.1 % propane was highest at 400 °C. Sensor reliability was tested by holding the samples at 400 °C for 500 h in Ar and O_2 in Ar ambient. No degradation of electrical or sensing characteristics was observed. The first AlGaN/GaN heterostructure HEMT sensor with Pt gate was demostrated by Schalwig [14]. Their structure was grown by PIMBE on sapphire starting with a 2 µm GaN buffer, followed by 25 nm AlGaN barrier with 30 % Al concentration and capped by 3 nm GaN on top. These sensors were tested towards H_2, C_2H_4 and CO at 300 °C. High response current increases were observed towards H_2, while CO response was approximately 6x lower in 4 % oxygen background as shown in fig. 2.9. Soon after, the same group tested response to NO and NO_2 and extended the operating temperature to 400 °C [15]. No response was observed to NO, while NO_2 response was of opposite direction, with current reducing when the oxidizing gas was introduced. A MOS diode on AlGaN/GaN structure was introduced by [16]. The structures were grown by MOCVD on sapphire. Scandium oxide (Sc_2O_3), deposited by PIMBE, was used as the insulator under the Pt sensing anode. Response to 10 % H_2 in N_2 was studied at room temperature. A voltage shift of 0.4 V in the I-V curve was observed when H_2 was introduced, which was 2x larger than that of a GaN SBD tested under similar conditions [17]. These MOS diodes where later applied for detecting ethylene (C_2H_4) and were ramped up to 400 °C operating temperature to increase the response current [18]. The same group also demonstrated A MOS-HEMT with Sc_2O_3 gate dialectic and Pt metal for room temperature H_2 sensing [19]. The current increase was 5x and 10x larger compared with the aforementioned MOS diode and GaN SBD, respectively. A SBD differential pair consisting of Pt contact active and Ti/Au reference devices was also utilized for H_2 sensing [20]. Such configuration allows to suppress false readings caused by voltage drift and temperature variations. Hydrogen sensing up to 800 °C in N_2 ambient using AlGaN/GaN SBD with Pt anode was reported in [21]. This very high temperature stability was attributed to passivation by PECVD SiN_x and post-passivation annealing at 700 °C for 10 min in N_2 after Pt anode was deposited during device fabrication. Going from

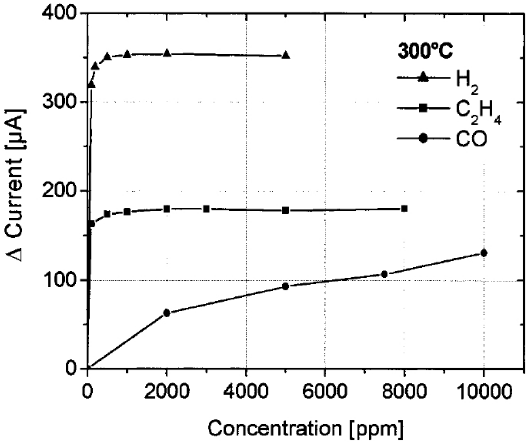

Figure 2.9: Response of a Pt-AlGaN/GaN HEMT towards reducing gases at 300 °C [14].

200 °C to 800 °C the sensing response towards 5 % H_2 increased from 6 % to 175 %. At 900 °C devices degraded due to Pt diffusion towards the AlGaN/GaN interface. The same group also compared high temperature H_2 response of Pt-SBD to sensors with Ir/Pt and Pd/Ag sensing layer stacks [22]. The sensitivity towards 5 % H_2 in N_2 as a function of operating temperature is shown in fig. 2.10. At temperatures under 300 °C the Pd/Ag structure demonstrated highest sensitivity, which gradually reduced with increasing temperature. The highest overall response was observed for Ir/Pt at 700 °C. Stability of Pd/Ag devices degraded rapidly above 400 °C due to sensing layer delamination. Sensitivity of Ir/Pt devices reduced above 700 °C due to the formation of eutectic phase. A comparison between Pd-AlGaAs, Pd-InGaP and Pd-GaN SBD H_2 sensors was made by [23, 24]. It was found that GaN diodes exhibited a larger Schottky barrier variation ($\Delta\phi_b$), higher response signal upon exposure to H_2 and larger operating temperature range (tested up to 297 °C). At lower temperatures Pd-GaN sensors demonstrated slower response rate, but much faster recovery rate.

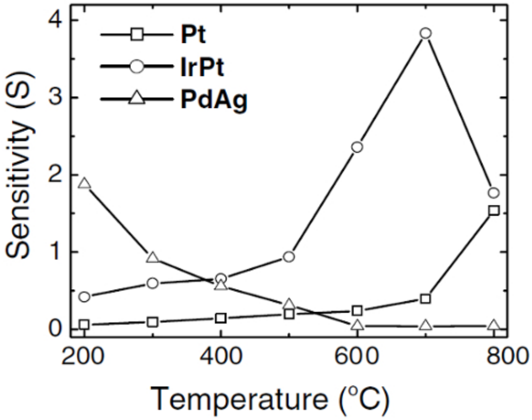

Figure 2.10: Comparison of H_2 detection sensitivity of Pt, Ir/Pt and Pd/Ag gated AlGaN/GaN Schottky diodes at different temperatures [22].

The majority of reported GaN based gas sensors are applied to detect hydrogen. Except for above mentioned results other notable works are summarized here. A Pt-GaN MOS diode with PECVD SiO_2 as insulator demonstrated supperior H_2 sensing response compared to MS diode [25]. The highest forward bias sensing response towards 9970 ppm H_2/air of the MOS and MS diodes were 14685 and 603.9 respectively and the tested temperature was up to 576 °C. Another type of MOS diode sensor was fabricated by thermally oxidizing the GaN surface prior to Pt anode deposition [26]. This sensor exhibited a shift from rectifying to ohmic behaviour as a consiquence of a large reduction in Schottky barrier height when exposed to H_2. Higher $\Delta\phi_b$ under same H_2 concentration was obsered in O_2 free carrier gas i.e. N_2. Another type of demonstrated MOS diode structure was Pt/$\beta-Ga_2O_3$/GaN [27]. The $\beta-Ga_2O_3$ was formed by photoelectrochemical oxidation and annealing at 700 °C in O_2. The inclusion of an oxide layer between the catalytic sensing electrode and GaN creates more hydrogen adsorption sites than the semiconductor surface leading to higher $\Delta\phi_b$ as compared to MS SBDs. Using a gas sensitive, reactive oxide (e.g. Ga_2O_3) provides additional sensitivity because the electrical characteristics are altered by the analyte, resulting in changes of the series resistance and ideality factor of the diodes.

The highest operating temperature of a Pt-AlGaN/GaN HEMT H_2 sensor was reported in [28]. Devices were operated up to 800 °C in N_2. Detection limit of 10 ppb H_2 was obtained at 450 °C. The impact of gate and drain bias voltage on sensor sensitivity was studied. The highest H_2 sensitivity was obtained at $V_{GS} \approx V_{TH}$ and V_{DS} was at the knee voltage. The application of N-face GaN for Schottky diode type H_2 sensors was demonstrated by [29, 30]. Hydrogen has higher affinity to N-face GaN and preferentially adsorbs on N sites. The SBDs on $(000\bar{1})$ GaN changed from rectifying in N_2 to nearly ohmic behaviour in 4 % H_2. This results in much larger current variation, especially under reverse bias, when compared to Ga-face GaN or AlGaN/GaN SBDs. Relative current change was 10^6 % and 170 % for N-face SBD and Ga-face AlGaN/GaN SBD, respectively. It was observed that N-face sensors had very rapid response towards H_2 but once the gas was purged with N_2 they did not recover to the initial baseline value like the Ga-face sensors. This was attributed to strong H–N bonds [30]. H_2 sensing with Pt/Pd-Schottky diodes on non-polar a-plane GaN were also demonstrated by [31]. Compared to Ga-face diodes, these sensors exhibited much larger current increase upon H_2 exposure, however they did not recover to their initial values, similarly to N-face SBDs. A-plane diodes remained rectifying upon H_2 injection and had similar maximum relative current variation(10^6 %) at room temperature as N-face diodes. The same group later reported GaN SBD diodes fabricated on semipolar $(11\bar{2}2)$ plane [32]. When compared to polar N-face and non-polar a-plane SBDs these sensors exhibited as high relative current change upon H_2 exposure and fast response time. Furthermore, like Ga-face, these sensors demonstrated signal recovery to the baseline level value when the ambient was switched to pure N_2.

A method to enhance sensing response of Pt-GaN SBDs by plasma treatment was proposed by [33]. Before anode metal (Pt) deposition the GaN surface was treated with Cl_2 plasma using ICP-RIE. The surface roughness increased from 0.8 nm to 3.36 nm after the ICP-IRE treatment. The maximum sensing response towards 1 % H_2 in air at RT increased from 1.02×10^4 to 2.05×10^5 when comparing devices without and with plasma treatment. Increased surface roughness produced more hydrogen adsorption sites resulting in higher current variation. Plasma treated sensors also demonstrated faster response times at every tested temperature. The frequently employed method to deposit the sensing electrode on GaN-based sensors is e-beam evaporation. Some researchers have attempted other methods of metal deposition in order to enhance performance. The sensitization and activation processes were used to from a Pd seed layer followed by electroless plating deposition (EP) of Pd or Pt gate electrodes for AlGaN/GaN HEMT H_2 sensors [34, 35]. These devices showed higher thermal stability compared to thermally evaporated gates. Electrophoretic deposition (EPD) of Pd gate for HEMT sensors was also demonstrated [36]. The advantage of EP and EPD methods is low deposition temperature and low damage Schottky interfaces. A solution phase method for depositing Pt with a nanonetwork structure was reported in [37]. The Pt nanonetworks were synthesized from a solution of K_2PtCl_4 and spin coated on the gate area of AlGaN/GaN HEMT. These sensors exhibited a ΔI_{DS} shift of 4.5 mA while reference devices with e-beam Pt gate only had ΔI_{DS}=0.7 mA towards 500 ppm of H_2 in air at RT. The increase in sensor response was attributed to a much larger surface area of the nanonetwork gate that provides more H_2 adsorption sites. Another approach to increase the surface-to-volume ratio was to form pyramid line nanostructures on top of the sensing electrode [38]. The AlGaN/GaN SBDs with 3D structured anodes were formed by first depositing the Pd planar contacts by e-beam. These were then coated with polystyrene nanospheres followed by another Pd e-beam evaporation. The anodes were finalized by removing the nanospheres in a solvent solution. The obtained sensors demonstrated a remarkably low 10 ppb H_2 in air detection limit while the reference planar contact devices could detect H_2 only down to 1 ppm. Overall pyramid nanostructured sensors had a wider detection range and sensing response compared to planar ones. A method to increase the effective electrode surface area by depositing SiO_2 nanoparticles (NP) on the AlGaN surface prior to Pd deposition was investigated in [39]. Different wt % of nanoparticles were dispersed in methanol and spin coated on the devices. Some trade-offs towards H_2 detection were observed between SiO_2 NP and reference SBDs. Devices with highest NP concentration had highest sensing response towards 1 % H_2, but their the detection limit was 10 ppm, while sensors with lower NP wt % could detect 1 ppm. Response times decreased with increasing NP wt%, however recovery times increased.

The presence of humidity in the environment was found to inhibit the hydrogen response of GaN-based sensors [40]. Water adsorbed on Pt or Pd is dissociated to form OH groups which block H_2 adsorption sites as well react with atomic H to form H_2O. To overcome cross-sensitivity towards humidity it was proposed to encapsulate the GaN-based SBD sensors in PMMA or PMGI [41, 42]. These polymers are widely applied in semiconductor industry and are processed by spin coating and photolithography. The moisture barriers did not hinder the diffusion of H_2 towards the catalytic electrode, hence the response of coated and bare sensors was equivalent in dry atmosphere. The PMMA encapsulated sensors can be operated up to 100 °C and PMGI remained stable at 300 °C.

An interesting CO_2 sensor based on AlGaN/GaN HEMT structure with a polyethylenimine (PEI)/starch sensing layer spin-coated on the gate region was demonstrated in [43]. Starch was added to PEI in order to enhance water absorption into the sensitive film. The sensing mechanism was described as reaction of PEI main chain with CO_2 and water present in the ambient resulting in $-NH_3^+$ and $OCOOH^-$ ions. This leads to charge redistribution in the polymer film which alters the surface charges on the AlGaN surface and consequently the 2DEG density. These sensors demonstrated a wide CO_2 detection range from 0.9 % to 50 % in N_2 ambient at 108 °C. The drain current of the sensor increased when CO_2 gas was introduced, indicating that additional positive charges were induced at the gate area leading to the increase in electron density inside the 2DEG.

Carbon monoxide detection with GaN based devices was also demonstrated in several reports. An AlGaN/GaN Pt-SBD demonstrated low detection limit of 8 ppm CO in N_2 when operated at 300 °C [44]. A zinc oxide nanowire gated HEMT was reported to detect CO at room temperature [45]. The ZnO nanowires were grown on GaN templates by chemical vapour deposition (CVD) and separated from the substrates by ultrasonication in ethanol. The solution was then deposited on the gate area by drop casting. Repeatable response down to 400 ppm CO in N_2 was observed. HEMT sensors to detect even lower CO concentrations using sol-gel grown ZnO nanorods were also presented [46]. In this case the nano-structures were grown directly on HEMT substrates and patterned on the gate area by wet etching. The obtained CO detection limit at room temperature was 100 ppm and was enhanced down to 30 ppm by raising the sensing temperature to 150 °C.

Ammonia sensors based on AlGaN/GaN SBD were repoted in [47]. E-beam deposited Pt with thickness 20 nm was the sensing electrode. The NH_3 response was tested with increasing temperature from 25 °C to 200 °C. The highest response of 182.7 was obtained at 150 °C towards 1 % NH_3/air and the detection limit was as low as 35 ppm NH_3/air. The same group also demonstrated NH_3 detection utilizing Pt-gated AlGaN/GaN HEMT [48]. Equivalent detection limit of 35 ppm NH_3/air was obtained, in this case at 30 °C. Electroless plating of Pt was found to be advantageous for low concentration NH_3 sensing with AlGaN/GaN SBD [49]. High sensing response of 16.22 was obtained for 1000 ppm NH_3 at 115 °C. The limit of NH_3 detection was 1 ppm in air at 25 °C and down to 10 ppb at 115 °C. Another report demonstrated detection of low NH_3 concentrations with ZnO nanorod gated AlGaN/GaN HEMT [50]. The nanorods were formed by sol-gel, equivalently to [45]. Sensitivity increased at higher temperature up to 300 °C and NH_3 was detected down to 0.1 ppm even at 25 °C.

An AlGaN/GaN HEMT with InZnO (IZO) gate oxygen sensor was shown by [51]. The gate material was deposited by RF magnetron cosputtering using In_2O_3 and ZnO targets, resulting in In/Zn=0.5 atomic ratio and 6 nm thickness. Drain current decreased when the sensor was exposed to 5 % O_2. The IZO gate is n-type with many oxygen vacancies, where gaseous O_2 can adsorb casing increased film resistivity and change in surface potential which in turn reduces the HEMT drain current. It was observed that after a few O_2 exposure cycles at 50 °C the sensitivity reduced as the bonding sites became occupied by oxygen atoms and were not reactivated during N_2 purge cycles. Increasing the operating temperature to 120 °C allowed to mitigate the quenching effect. Adding a pre-annealing step at 350 °C in N_2 before each oxygen exposure produced additional adsorption sites and enhanced O_2 response. An oxygen sensitive HEMT device with SnO_2 sensing gate prepared by hydrothermal synthesis process was studied by [52]. Annealing the MOX at 400 °C was observed to increase the grain size and improve crystallinity. When exposed to O_2 the drain current once again decreased, however the gradual sensitivity reduction was not observed as in the case of IZO-gated sensors. At 100 °C operating temperature oxygen concentration down to 1 % was detected.

Nitric oxide (NO) and nitrogen dioxide (NO_2) are serious environmental pollutants and their concentration in air has to be strictly monitored. It was reported that in the presence of humidity the exposed AlGaN surface of the AlGaN/GaN heterostructure can detect 1 ppb variations in NO_2 concentration at room temperature [53]. The water film on the AlGaN induces additional positive surface charge, which is neutralized by NO_2 and the measured sensor resistance increases. Sensitivity increased at higher relative humidity levels, while response and recovery times were reduced. In synthetic air ambient the response and recovery times of these sensors were on the order of hours i.e. too slow for continuous monitoring applications [54]. The same group also studied the impact of recessing the AlGaN surface and showed that sensitivity increased with deeper recess and predicted the limit of NO_2 detection to be in the ppt range [55]. A Pd-ZnO/GaN heterojunction diode (HJD) NO and NO_2 sensor was demonstrated by [56]. The 10 nm thick ZnO layer was grown by ALD on GaN templates grown on sapphire and the Pd thickness was 10 nm. These diodes showed proper rectifying characteristics at RT and 250 °C. Response to NO_2 was ~1 mA and 3x larger than to NO. Signal saturation was observed at 20 ppm for both gases. The sensing mechanism was described as increase in Schottky barrier height and tunnelling length caused by gas adsorption. The gas molecules dissociate and negatively charged oxygen atoms deplete the charge carrier electrons around the junction. Response to NO, NO_2 and NH_3 by Pt-AlGaN/GaN HEMTs at 300–600 °C in N_2 was shown by [57]. Low NH_3 detection limit of 3 ppm was obtained, while NO and NO_2 concentrations down to 100 ppm were detected. Response times towards all three gases reduced significantly at 600 °C. Sensors with similar structure reported in [15] did not respond to NO under 4 % O_2 in N_2 ambient. The authors suggested that sensing NO was made possible by optimizing sensor layout design and using a thinner (15 nm) Pt sensing electrode. Furthermore, response towards NO using Pt/GaN SBDs at 500 °C was compared under pure N_2 and 20 % O_2 in N_2 by [58]. In the presence of O_2 the sensitivity towards NO was significantly diminished. They have also compared NO response of sensors with different Pt thickness and found that voltage shift for 500 ppm NO increased from 0.42 mV to 4 mV when Pt thickness was reduced from 40 nm to 8 nm.

Methane detection was also reported using Pt-AlGaN/GaN SBDs [59]. This was possible mainly due to high temperature operation capability of GaN-based devices. Response to CH_4 from 0.5 % to 2 % was measured at 450 °C. The high operating temperature is necessary for C-H bonds to break on the Pt surface.

An ethanol sensor using AlGaN/GaN Schottky diode with a 10 nm thick silver anode was demonstrated by [60]. The sensing electrode was deposited by e-beam evaporation. The highest sensitivity was obtained at 250 °C and the detection limit was 58 ppm in N_2.

2.3. AlGaN/GaN HEMT SENSOR FABRICATION

The microfabrication of GaN-based devices differs greatly from well established MOSFET manufacturing technology. A significant part of this research was devoted to developing the GaN sensor fabrication process. The first generation of sensors was processed in the research cleanroom of the Institute of Semiconductors, Chinese Academy of Sciences in Beijing. The fabricated devices were successfully applied for measurement of various gases as is demonstrated in the later chapters of this thesis. The technology developed in Beijing cleanroom was later transferred to the university cleanroom of Southern University of Science and Technology, in Shenzhen, where it was further improved and the second generation of sensors was processed. The specifics of each process step are discussed in detail in the following sections.

2.3.1. STARTING MATERIAL SELECTION

Most of the commercially available GaN structures are grown heteroepitaxially due to current high costs, limited availability and small size of bulk GaN substrates. Instead, sapphire, silicon carbide and silicon substrates are typically utilized for epitaxial growth. There is always lattice constant and thermal expansion coefficient (TEC) mismatch when

GaN is grown on foreign substrates, as summarized in table 2.2. Differences in lattice constants between GaN and the substrate result in the appearance of misfit and threading dislocation type defects inside the grown film and degrades the electrical characteristics. TEC mismatch causes thermal stress during substrate cool down and can result in large bowing, film cracking or even substrate shattering unless proper strain engineering layers are included during the growth process.

Table 2.2: Properties of substrates for GaN epitaxial growth [61].

Substrate	**Sapphire**	**Si**	**4H-SiC**	**GaN**
Lattice mismatch (%)	16	-17	3.1	0
TEC mismatch (%)	-34	53.6	21.4	0
Substrate size (mm)	150	300	150	30
Substrate price	Medium	Very low	High	Very High

With optimized growth conditions and strain management the threading dislocation density on all three substrates can be reduced to 10^8 cm^{-2}. SiC substrates have the lowest TEC and lattice mismatch to GaN therefore material growth is the least complex. GaN-based high reliability and power RF amplifiers utilize SiC substrates due their high thermal conductivity, however presently they have the highest cost per chip area. Recently, Si substrates have gotten much attention for HEMT power device manufacturing due to the availability of low cost, large diameter substrates with decent thermal conductivity.

For this research HEMT structures grown 50 mm sapphire substrates were used. GaN-on-sapphire is the most mature growth technology that has been widely applied in the LED industry. Sapphire is also chemically stable, making it suitable for harsh environment sensing applications. The epitaxial structure was supplied by a commercial vendor Suzhou Nanowin Science and Technology. The details of the used epitaxial HEMT layer structure are shown in fig. 2.11. It was grown by metal organic chemical vapour depo-

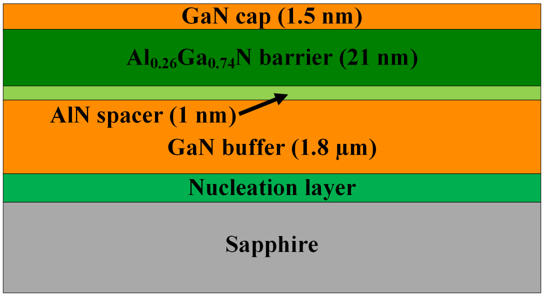

Figure 2.11: AlGaN/GaN HEMT epitaxial structure used for gas sensor fabrication.

sition (MOCVD), which is the leading industry method due to higher growth rate, the ability to precisely control the layer composition and compatibility with larger wafers. Starting from the substrate the material growth began with the nucleation layer, required to reduce the lattice mismatch between GaN and the substrate. The exact parameters of this layer are vendor proprietary, however AlN is typically used. The buffer layer is necessary to reduce the number of dislocation type defects. Furthermore, it provides isolation between the channel and the substrate to sustain high electric fields in high voltage transistors. Surface roughness of the buffer must be minimized in order to enhance the confinement of the active channel and form and abrupt junction with the barrier layer. Among available options, the composition and thickness of the AlGaN barrier were chosen to be Al 26 % and 21 nm, respectively to obtain high 2DEG carrier density. Inserting an ultra thin 1 nm AlN spacer between the buffer and barrier layers increases the effective conduction band offset (ΔE_C) [62]. As a result, alloy scattering reduces and electron mobility is improved. A slight increase in carrier density is also observed. Conduction band diagrams of AlGaN/GaN and AlGaN/AlN/GaN structures are shown in fig. 2.12, demonstrating the differences in ΔE_C. The structure is finalized by a 1.5 nm GaN capping layer. This layer helps to reduce the gate leakage current by increasing the effective Schottky barrier height [63]. It is also effective in reducing the current collapse phenomenon and lowering top surface roughness. The vendor specified electrical properties of the used AlGaN/GaN wafers are: sheet carrier density $n_s = 1 \times 10^{13}\,\mathrm{cm}^{-2}$, electron mobility $\mu = 1300\,\mathrm{cm}^2/\mathrm{Vs}$ and sheet resistance $R_{sh} = 330\,\Omega/\mathrm{sq}$.

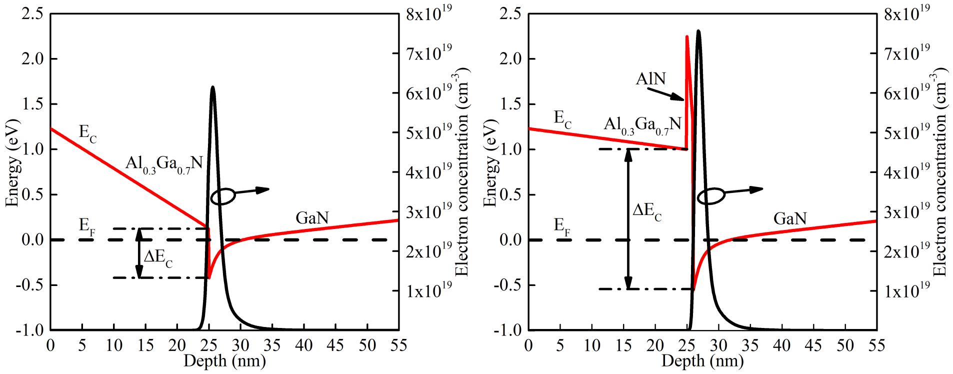

(a) (b)

Figure 2.12: Simulated conduction band diagrams of (a) AlGaN/GaN and (b) AlGaN/AlN/GaN heterostructures.

2.3.2. INDIVIDUAL DEVICE ISOLATION

The 2DEG channel is formed across the entire substrate during MOCVD growth. Individual devices must be isolated from one another by terminating the 2DEG outside the active area. The two most widely applied methods for device isolation are ion implantation and plasma etching. The former uses multiple energy and dose ions in order to form high resistivity regions with uniform dopant concentration extending through the barrier layer and part of the buffer (fig. 2.13a). Ion implantation damages the GaN lattice and forms energy states that capture free electrons. Numerous ion species have been reported for GaN device isolation such as O, N, Ar, Al, C or Fe [64]. The advantage of implantation isolation is that substrate surface remains planar afterwards. Etching is a straight forward isolation method, where the AlGaN/GaN is plasma etched into the buffer layer, significantly below the 2DEG (fig. 2.13b) to define separate regions (mesas) where devices are subsequently formed.

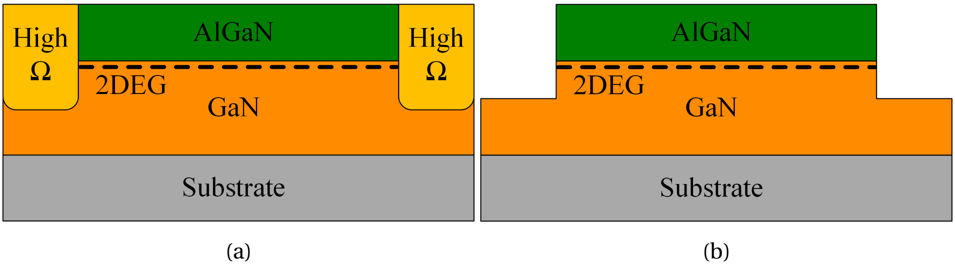

(a) (b)

Figure 2.13: Schematic diagram of HEMT isolation via (a) ion implantation and (b) plasma etching.

We have implemented mesa isolation method by inductively couple plasma reactive ion etching (ICP-RIE). Chlorine containing plasma is known to etch GaN with low surface damage. ICP based etching is advantageous as it allows more control over the etching conditions. The plasma density can be varied by adjusting the ICP coil power, while the RF power determines the energy of the ions impinging on the substrate. Mesa etching of the first generation devices was performed in an AST Cirie-200 etcher. The gases used for GaN etching were Cl_2 and BCl_3. By increasing the ICP power from 150 to 300 W the etching rate increased from 0.59 to 0.73 nm/s. The lower rate recipe was used for device fabrication. The 2nd generation devices were etched using Naura GSE 200 Plus system and the etching rate was 0.95 nm/s. The etching recipe details of both systems are presented in table 2.3. Prior to mesa etching, the substrates were cleaned with a 3:1 sulfuric acid and hydrogen peroxide piranha solution, acetone, isopropyl alcohol (IPA) and DI water. Positive tone photoresist (PR) AZ-6130 or RZJ-304 was used to pattern the mesas and the target etching depth was 110 ± 10 nm. Figure 2.14a shows the top view

Table 2.3: Recipe details for GaN ICP-RIE etching.

Tool name	**AST Cirie-200**	**GSE 200 Plus**
Sensor gen	I	II
Etching gas	Cl_2=40 sccm BCl_3=5 sccm Ar=5 sccm	Cl_2=45 sccm BCl_3=15 sccm Ar=5 sccm
Base pressure (mtorr)	8	10
ICP power (W)	150	100
RF power (W)	15	25

optical image of the etched mesa structure and fig. 2.14b shows the AFM step profile.

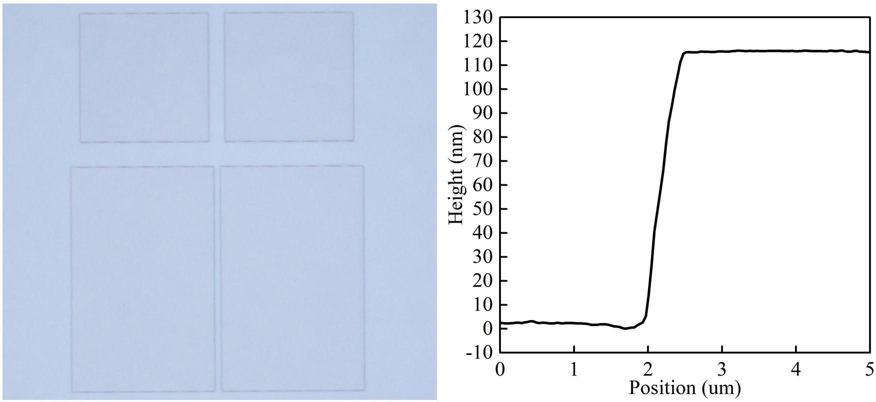

(a) (b)

Figure 2.14: Mesa structure etched by ICP-RIE: (a) top view optical image and (b) AFM step profile.

2.3.3. OHMIC CONTACT FORMATION

PATTERNING OF METAL LAYERS

Metal-semiconductor contacts are of critical importance for any semiconductor device. Ohmic contacts are required to provide low resistance interface between the active area and the outside circuit. Source and drain contacts of AlGaN/GaN HEMTs must fulfil the requirement of lowest possible contact resistance (R_C) in order to maximize the current flow across the device and minimize on-resistance (R_{ON}). Furthermore, ohmic contacts must be non-rectifying and stable during the lifetime of the device.

The process of forming ohmic contacts started with the photolithographic pattern definition. Afterwards the metal layers were deposited by electron beam (e-beam) evaporation followed by lift-off patterning. Finally high temperature rapid thermal annealing was used to form the ohmic contacts.

Lift-off method available at the Institute of Semiconductors uses DNR-L300 negative photoresist. In this case, the exposure dose and development time are tuned to produce a sidewall profile with a negative slope. After metal deposition, discontinuities in the film are formed due to poor step coverage of e-beam evaporation, as shown in fig. 2.15. The patterns are then formed by removing the sacrificial photoresist layer using acetone or a resist stripper. The photoresist stripping duration was approximately 90 min, after which defective patterns, where the metal was not completely removed, still remained, as shown fig. 2.16. To reduce the process time a physical metal strip was implemented.

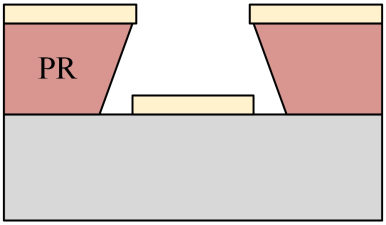

Figure 2.15: Schematic of single layer lift-off process with negative photoresist.

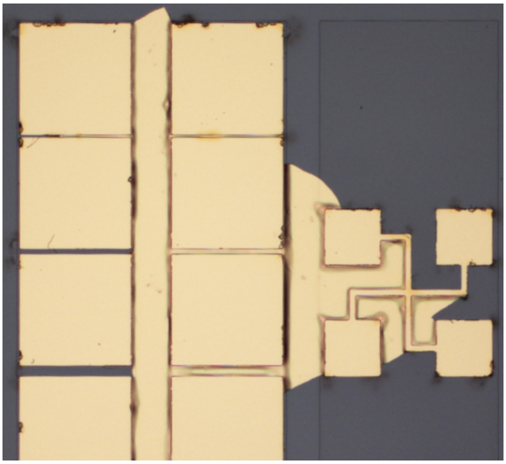

Figure 2.16: Defects remaining after single layer lift-off process.

This procedure involved sticking a piece of blue dicing foil on the samples and carefully peeling off the bulk of the metal layer from the PR surface followed by a 10 min acetone soak to lift-off the remaining patterns. This method was well suited for metal layers under 250 nm. Thicker layers were observed to have rough edges, peeling or incomplete metal removal along line edges (fig. 2.17). These issues are attributed to insufficient un-

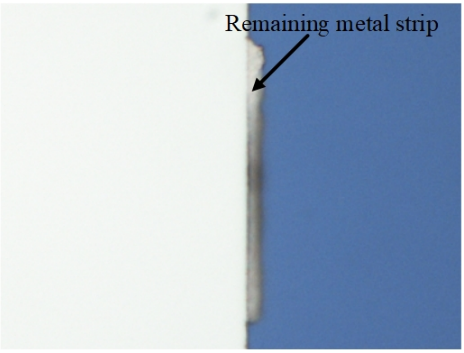

Figure 2.17: A metal pattern after lift-off with physical peeling. A metal strip defect still remains.

dercut of the negative photoresist profile which leads to partial metal coverage on the sidewalls and prevent the solvent coming into contact with the sacrificial layer.

A bilayer lift-off process was developed in Shenzhen cleanroom to obtain high quality pattern transfer for 2nd generation of sensors. In this approach, lift-off resist LOR 5A is first spin-coated on the substrate and prebaked at 170 °C for 8 min. Afterwards standard positive photoresist (RZJ-304) is spin-coated on top of the LOR layer and patterned as normal. During development with TMAH 2.38 % based developer the top imaging photoresist is patterned anisotropically while the LOR develops isotropically forming a large undercut favourable for lift-off. The LOR undercut rate in the developer depends on the prebaking temperature and development time. SEM images of the undercut calibration after 70 s and 100 s in the developer are shown fig. 2.18. It is clearly visible that after e-beam evaporation the sidewalls of the photoresist are coated with metal. Thanks to the LOR undercut the metal is discontinuous between the substrate and photoresist, having a sufficient gap for the solvent to reach the sacrificial layers. An optimal development time of 80 s was chosen. Lift-off was done using N-Methylpyrollidone (NMP) or Dimethyl Sulfoxide (DMSO) photoresist stripper. The solvent was poured into a glass petri dish, heated on a hot plate to 60 °C and the substrates were placed inside to remove the double layer resist. The required time to complete lift-off was highly dependent on the metal thickness and was between 15 min to 50 min, longer for thicker layers. After the bulk of the metal was separated from the substrates they were transferred into a second solvent dish to clean off any remaining metal particles. The process was completed with IPA dip and DI rinse. Figure 2.19 shows high quality metal patterns obtained by using bilayer lift-off. No pattern damage or incomplete film removal was observed.

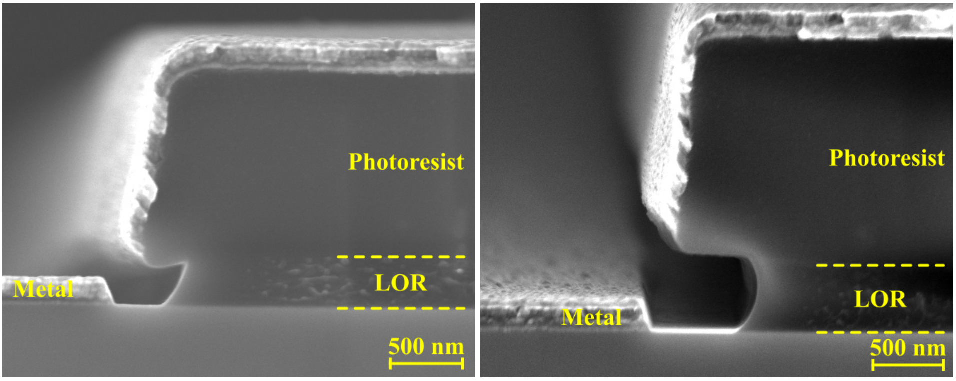

(a) (b)

Figure 2.18: SEM images of a bilayer lift-off stack after development for (a) 70 s and (b) 100 s.

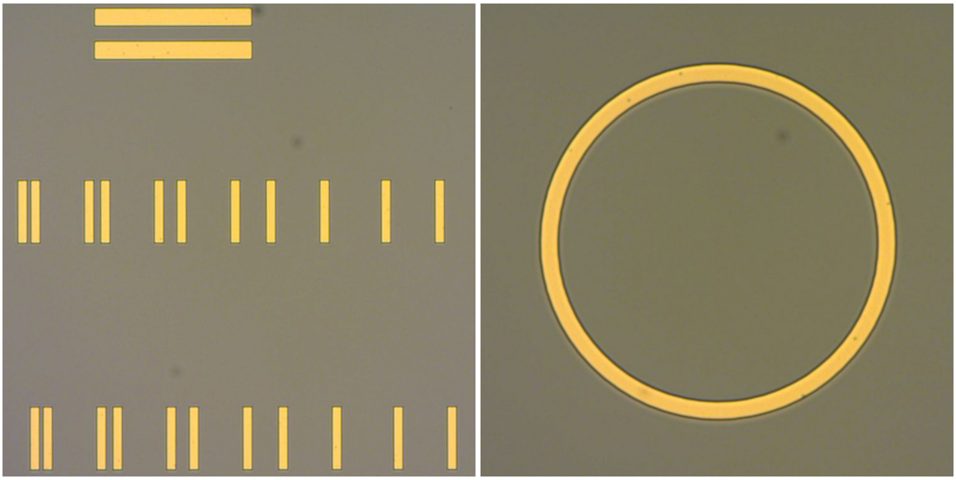

Figure 2.19: Optical images of metal patterns after bilayer lift-off.

OHMIC CONTACT METALIZATION

Continuous research efforts have established that most promising ohmic metallization for AlGaN/GaN is based on Ti/Al bilayer as both these metals have low work functions (Ti=4.33 eV, Al=4.28 eV) [65]. Soon after, a four layer stack of Ti/Al/Ni/Au was reported to achieve low resistance ohmic contacts on GaN [66]. Numerous stacks with the Ti/Al/X/Au structure, where X is the barrier metal e.g. Ti, Ta, Ni, Mo, Ir, Pt were demonstrated afterwards to achieve low contact resistance on GaN and AlGaN/GaN [67]. Titanium is used as the first contact layer due to the high reactivity with GaN. During the contact annealing process titanium nitride forms at the interface, lowering the Schottky barrier height. The N atoms are supplied by out-diffusion from GaN resulting in nitrogen vacancies that act as donors leading to an increase in the carrier concentration below the contacts. Aluminium is the second layer that forms low work function and low resistivity compounds with the remaining metals and is called the overlayer. The third metal acts as barrier to reduce inter-diffusion of the first two metals with the 4th layer. As previously mentioned several metals have been used for the barrier. During the high temperature annealing these metals impact the formation of alloys inside the multilayer that determines the resulting surface morphology and contact resistance. The top gold layer is used for capping the structure and preventing surface oxidation [68].

During process development of the 1st sensor generation we utilized the Ti/Al/X/Au ohmic contact structure with Ni and Ti as the diffusion barrier and the thickness of each layer was 20/110/40/50 nm, deposited by e-beam evaporation. Ni is a widely used barrier metal and a well optimized contact process on AlGaN/GaN was reported to obtain low contact resistance of R_C=0.2 Ω mm [69]. In our case it was observed that after lift-off using negative resist the top gold layer was partially peeled off, if Ni was used as barrier metal, as shown in fig. 2.20a. Adhesion between Ni and Au was not sufficient to withstand lift-off with physical peeling. Substituting Ni with Ti yielded better results as shown in fig. 2.20b. No delamination of Au was observed, therefore further ohmic contact optimization was carried out with Ti as the barrier layer.

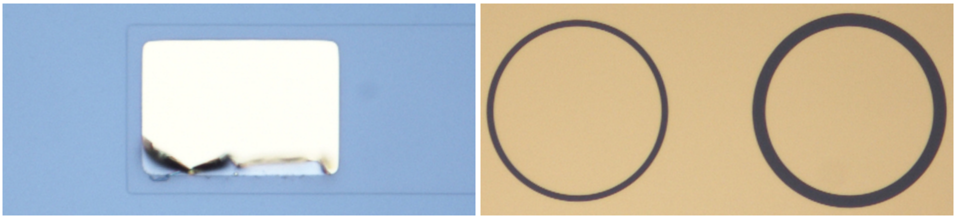
(a) (b)

Figure 2.20: Optical image of Au peeling after lift-off of ohmic contacts with Ni barrier (a). Successful lift-off of ohmic contacts with Ti barrier (b).

OHMIC CONTACT CHARACTERIZATION

To accurately determine ohmic contact resistance the transmission line model (TLM) test structures were added to our photolithography masks [70]. The linear TLM structure consists of a series of same size metal pads with increasing gap between them as shown in fig. 2.21. Total resistance (R_M) between the two adjacent pads can be expressed as:

$$R_M = \frac{R_S}{W}(S + 2L_T) \tag{2.9}$$

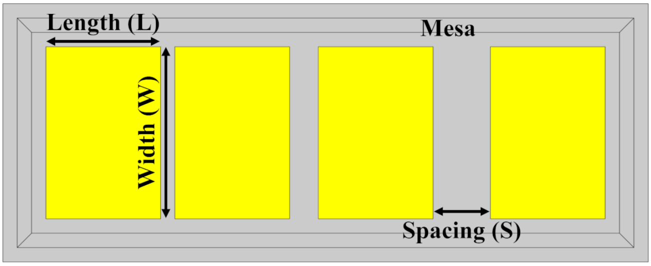

Figure 2.21: Schematic of a linear TLM structure showing equal size pads separated by increasing spaces.

where R_S is the semiconductor sheet resistance, W is the width of the metal contact, S is the spacing between the pads and L_T is transfer length, which is expressed as $L_T = \sqrt{\frac{\rho_C}{R_S}}$, where ρ_C is the specific contact resistance in $\Omega\,\text{cm}^2$. Plotting the R_M versus the pad spacing (S) graph allows to extract the R_S, R_C and L_T values. Linear fitting is performed through the measured data points and the R_S is determined from the slope, the y-axis intercept is $R_M = 2R_C$ and the intercept with x-axis is $2L_T$, as shown in fig. 2.22. The contact resistance is normalized to the pad width ($R_C W$) to obtain values in $\Omega\,$mm. One drawback of linear TLM structures is that there will be current spreading around the pad corners due to current crowding, which leads to underestimation of R_C. This issue can be avoided with mesa etching around the periphery of the test structure (see fig. 2.21).

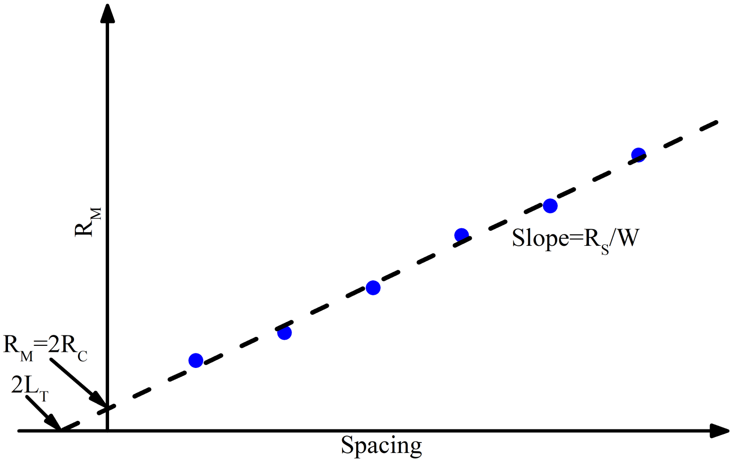

Figure 2.22: Example TLM measurement of R_M versus pad spacing. The R_S is extracted from the slope of the linear fit, L_T from x-axis and R_C from y-axis intercept, respectively.

To reduce the number of process steps during initial contact resistance optimization, circular TLM (CTLM) test structure was implemented [71]. It consists of round pads separated from a shared large contact by rings with increasing width as shown in fig. 2.23. Round contacts allow to avoid current crowding, therefore CTLM structure does not require mesa isolation and is fabricated with only one optical lithography step. Similarly to eq. (2.9) the total measured resistance is:

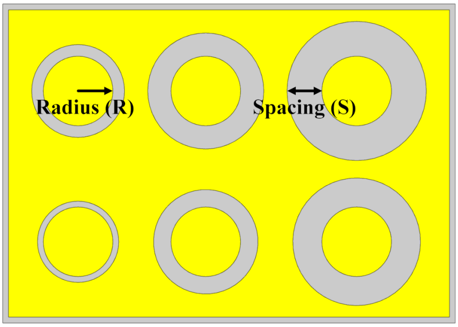

Figure 2.23: Schematic of a circular TLM structure showing equal size circular pads separated from a large common pad by rings of increasing width.

$$R_M = \frac{R_S}{2\pi R}(S + 2L_T)c \tag{2.10}$$

where R is the radius of the round contact and c is the correction factor. This factor is calculated for every contact spacing as:

$$c = \frac{R}{S}\ln\left(\frac{R+S}{R}\right) \tag{2.11}$$

The measured R_M values need to be devided by the corresponding c to obtain proper linear fitting of the R_M/c versus S data [71]. The R_S, R_C and L_T are then determined the same way as for linear TLM. The normalized contact resistance is obtained by $R_C(2\pi R)$.

OPTIMIZATION OF CONTACT ANNEALING PARAMETERS

Previously reported results on ohmic contacts to AlGaN/GaN have demonstrated a wide range of annealing process conditions, that depend on the AlGaN barrier thickness, Al % incorporation, defect density and specifics of different annealing tools.

Test samples on our device wafers were fabricated to optimize the annealing process and obtain ohmic contacts with acceptable $R_C < 1\,\Omega\text{mm}$. After lithographic patterning of the CTLM test structures native oxide (Ga_2O_3) was removed by dipping the samples in 1:4 HCl:H_2O solution for 60 s [72]. The wafers were then immediately loaded into the e-beam evaporator for contact metal deposition. After lift-off the test wafers were quartered and a series of annealing temperature experiments was carried out in the range of

750–900 °C under N_2 ambient using RTP-500 rapid thermal processing system. Based on literature [68], the initial rapid thermal anneal (RTA) time was chosen to be 40 s. Samples were loaded into the RTA chamber and a nitrogen purge was done for 5 min to remove any oxygen before starting the temperature ramp.

Annealed samples were measured using Keithley 4200-SCS semiconductor characterization system. Resistance measurements were performed using the four-point probe method. Current was supplied between the CTLM pads using one pair of probes and the voltage drop was sensed using the second pair of probes. This method eliminates the impact of the measurement cables, probe contact resistance and internal resistance of the measurement unit, which are in series with the device under test. The extracted contact resistance (R_C) and specific contact resistance (ρ_C) values at tested annealing temperatures are shown in fig. 2.24. With increasing temperature both values decreased with minimum values of $R_C = 1.42\,\Omega$mm and $\rho_C = 4.15 \times 10^{-5}\,\Omega\text{cm}^2$ obtained at 870 °C. At 750 °C and 800 °C the contacts were still slightly rectifying, while at 900 °C the resistance values increased. Based on the obtained results optimization of annealing time was conducted at 870 °C. By increasing the time to 45 s the average contact resistance was reduced to $0.56 \pm 0.24\,\Omega$mm. The average R_M vs S for the optimized annealing conditions is shown in fig. 2.25. Good linear fit was obtained for the measured resistance data after correction factors (c) were applied. A characteristic increase in surface roughness was observed after high temperature annealing of Au-based contacts, however surface defects such as blistering or cracking did not occur (fig. 2.26).

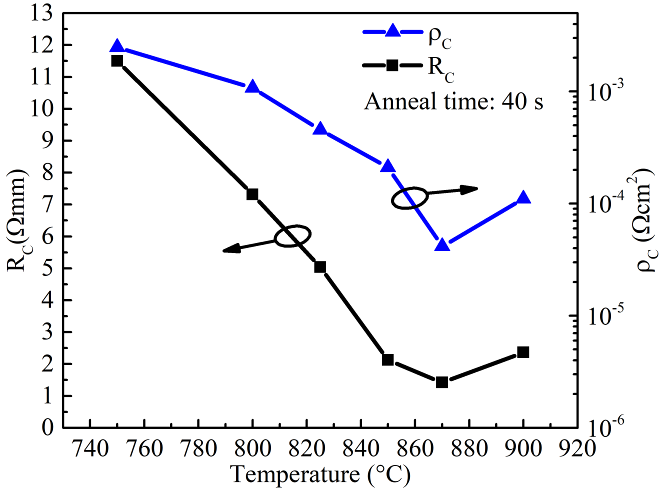

Figure 2.24: Extracted R_C and ρ_C values from CTLM measurements of ohmic contacts annealed at 750–900 °C for 40 s.

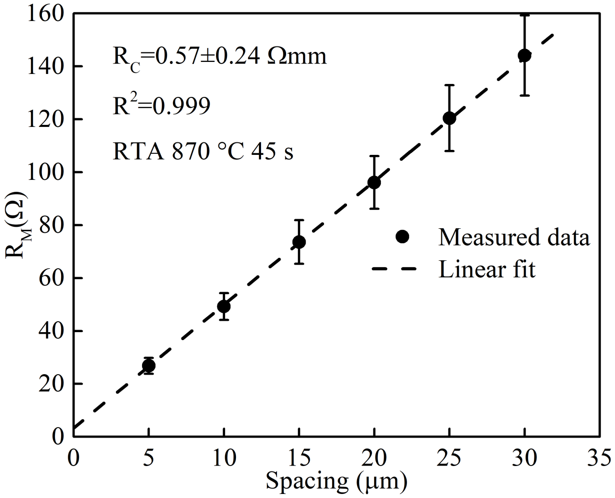

Figure 2.25: Total measured resistance R_M versus CTLM gap spacing of ohmic contacts annealed at 870 °C for 45 s.

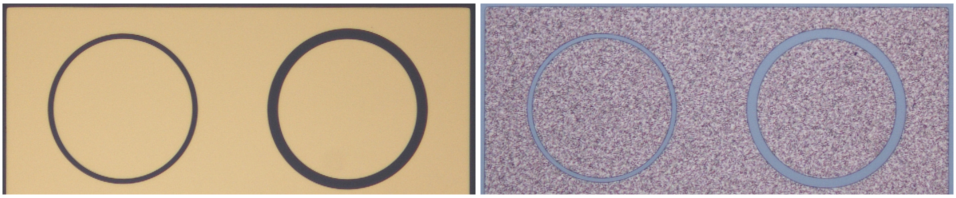

(a)

(b)

Figure 2.26: Optical image of Au-based contacts (a) before and (b) after annealing at 870 °C for 45 s.

The ohmic contact formation mechanism in Au-based contacts annealed at high temperature is attributed to the Au assited formation of TiN protrusions through the AlGaN layer [73]. A metal like contact directly to the 2DEG is formed and results in low contact resistance [74]. The TiN protrusions are preferentially formed along threading dislocations of the AlGaN. Part of Au diffuses through the metal stack to the interface with GaN and causes Ga out-diffusion. The initial TiN protrusion along the defect site expands to form islands as Ga is depleted to form Au-Ga compounds [75]. As TiN is a known diffusion barrier, no Au was found inside the TiN islands.

Ohmic contact fabrication process in the Shenzhen cleanroom followed similar process as mentioned above with two distinctions: bilayer lift-off metal patterning and different annealing conditions. The latter was done using Annealsys AS-One RTP system and the optimized conditions to obtain $R_C < 1\,\Omega\text{mm}$ were 850 °C for 45 s.

2.3.4. SCHOTTKY CONTACT FORMATION

The metallization for rectifying Schottky gate electrodes of AlGaN/GaN HEMTs must possess high barrier height to minimize gate leakage current, low resistivity and good adhesion. A typical gate metallization of GaN-based HEMTs consists of a Ni/Au bilayer as nickel has a high work function (5.15 eV). HEMT-based sensors present further requirements for gate metals. The metal of choice must be catalytically active towards the target analyte, furthermore it must be chemically and thermally stable as the gate contact is directly exposed to the ambient. Platinum (Pt), palladium (Pd) and iridium (Ir) are suitable candidates with well studied catalytic properties.

Platinum was used for sensing gate electrode fabrication, due to high work function (5.65 eV) and barrier height to GaN of 1.1 eV as well as high temperature stability [21, 76]. Two processing approaches were attempted for gate electrode fabrication. The first approach was to passivate the GaN surface with a dielectric layer (e.g. SiN_x) after ohmic contact processing, as shown in fig. 2.27a. Openings for the gate electrode were then etched, followed by 10 nm Pt e-beam evaporation and lift-off as shown in fig. 2.27b. Such sequence was used to protect the GaN surface from contamination during further processing steps. After Pt gate patterning it was observed that parts of the gate structure that were deposited on the insulator have severely delaminated, as shown in fig. 2.28a, however areas of the pattern deposited directly on GaN did not delaminate. A structure with properly patterned gate is shown in fig. 2.28b, but yield was very low. Adhesion of noble metals is highly dependent on the underlying substrate and deposition method. Based

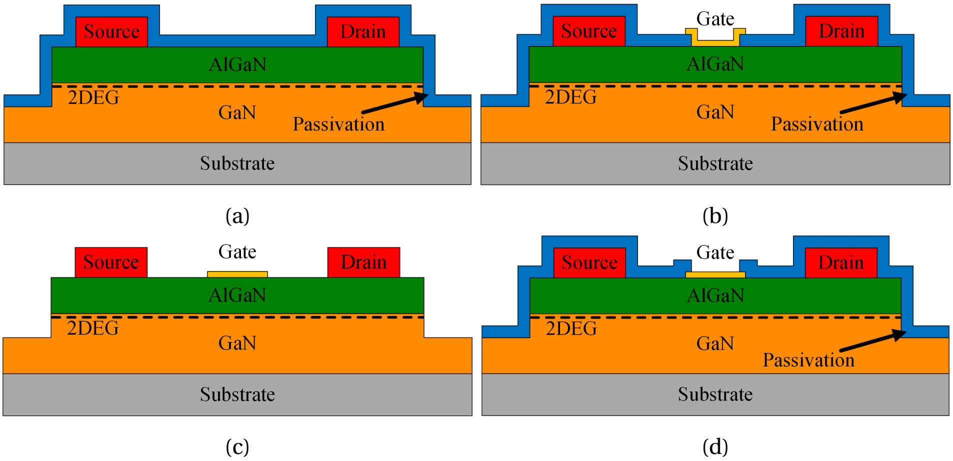

Figure 2.27: Gate processing approaches with surface passivation before (a, b) and after (c, d) gate metal deposition.

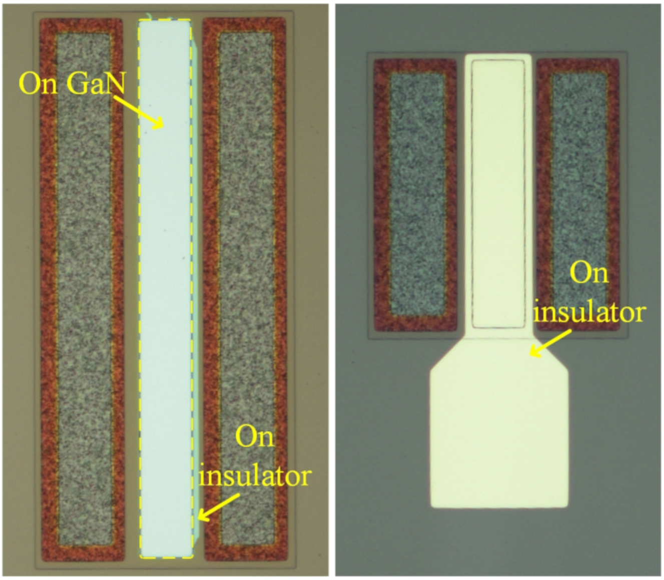

(a) (b)

Figure 2.28: Optical image of Pt gate delamination on insulator (a). Gate structure without defects is shown for comparison (b).

on these results, the second gate process approach where, the gate metal was patterned directly on GaN (fig. 2.27c), was studied. In this case the surface passivation was done at end of device processing (fig. 2.27d). This approached resulted in good Pt adhesion and high yield as shown in fig. 2.29.

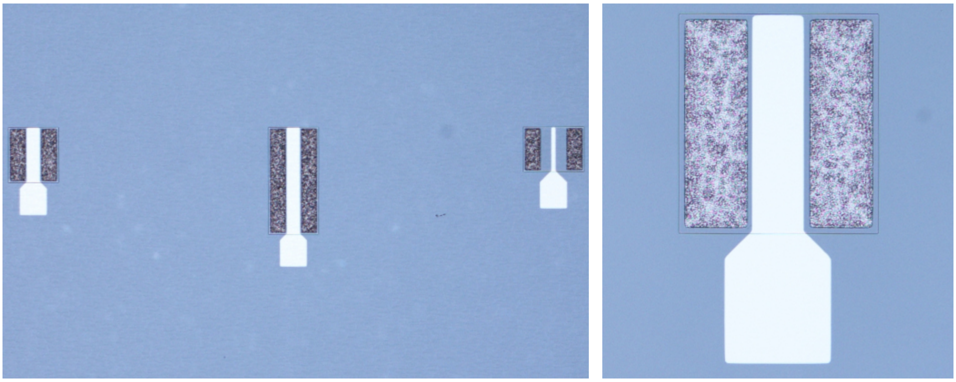

(a) (b)

Figure 2.29: Optical image of devices with Pt gate patterned before insulator deposition (a). A higher magnification image of a single device (b).

2.3.5. FINAL METALLIZATION, PASSIVATION AND PACKAGING

After forming the Schottky gate, the final wireboding and interconnection metal layer was formed by e-beam evaporation. A Ti/Au stack with thickness of 15/300 nm was deposited and patterned by lift-off. The thin Ti layer is required to enhance adhesion to the substrate and Au to reduce the interconnect sheet resistance and facilitate wire bonding.

The final processing step was passivation of the device surface with a dielectric layer to enhance stability as well as protect the top metal from scratching during subsequent sensor packaging and testing. 200 nm of SiN_x was deposited by PECVD at 350 °C as passivation. To open the active gate area and bondpads the SiN_x was patterned by ICP-RIE etching down to ~50 nm followed by BOE etch to selectively remove the remaining insulator residues. The active area and bondpads of a completed device are shown in fig. 2.30.

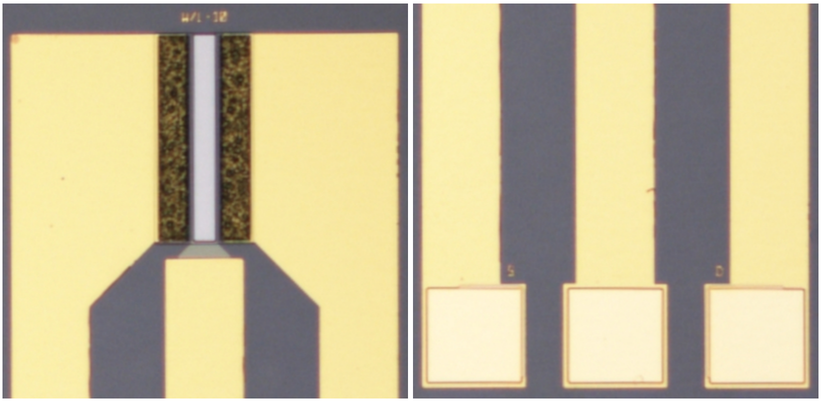

(a) (b)

Figure 2.30: Optical image of (a) the active area and (b) the wire-bonding pads of a completed Pt-AlGaN/GaN HEMT sensor.

Processed wafers were diced into single chips for packaging and testing. The process of sapphire wafer dicing started with backside grinding down to 150 µm. Laser scribing was then done from the front side to the depth of 100 µm and chips were separated by breaking and expanding.

In order to interface the chips with the gas sensor testing chamber they were die-attached and wire bonded to custom designed ceramic PCBs that can withstand high ambient temperatures.

REFERENCES

[1] H. Umezawa, *Recent advances in diamond power semiconductor devices,* Materials Science in Semiconductor Processing **78**, 147 (2018).

[2] S. J. Pearton, J. Yang, P. H. Cary, F. Ren, J. Kim, M. J. Tadjer, and M. A. Mastro, *A review of* Ga_2O_3 *materials, processing, and devices,* Applied Physics Reviews **5**, 011301 (2018).

[3] D. Ueda, *Properties and Advantages of Gallium Nitride,* in *Power GaN Devices: Materials, Applications and Reliability*, edited by M. Meneghini, G. Meneghesso, and E. Zanoni (Springer International Publishing, Cham, 2017) pp. 1–26.

[4] D. Zhuang and J. Edgar, *Wet etching of GaN, AlN, and SiC: a review,* Materials Science and Engineering: R: Reports **48**, 1 (2005).

[5] T. Hanada, *Basic Properties of ZnO, GaN, and Related Materials,* in *Oxide and Nitride Semiconductors: Processing, Properties, and Applications*, edited by T. Yao and S.-K. Hong (Springer Berlin Heidelberg, Berlin, Heidelberg, 2009) pp. 1–19.

[6] H. Morkoç, *General properties of nitrides,* in *Nitride Semiconductor Devices* (John Wiley & Sons, Ltd, 2013) Chap. 1, pp. 1–61.

[7] E. S. Hellman, *The Polarity of GaN: a Critical Review,* MRS Internet Journal of Nitride Semiconductor Research **3**, E11 (1998).

[8] O. Ambacher, J. Smart, J. R. Shealy, N. G. Weimann, K. Chu, M. Murphy, W. J. Schaff, L. F. Eastman, R. Dimitrov, L. Wittmer, M. Stutzmann, W. Rieger, and J. Hilsenbeck, *Two-dimensional electron gases induced by spontaneous and piezoelectric polarization charges in N- and Ga-face AlGaN/GaN heterostructures,* Journal of Applied Physics **85**, 3222 (1999).

[9] O. Ambacher, B. Foutz, J. Smart, J. R. Shealy, N. G. Weimann, K. Chu, M. Murphy, A. J. Sierakowski, W. J. Schaff, L. F. Eastman, R. Dimitrov, A. Mitchell, and M. Stutzmann, *Two dimensional electron gases induced by spontaneous and piezoelectric polarization in undoped and doped AlGaN/GaN heterostructures,* Journal of Applied Physics **87**, 334 (2000).

[10] J. P. Ibbetson, P. T. Fini, K. D. Ness, S. P. DenBaars, J. S. Speck, and U. K. Mishra, *Polarization effects, surface states, and the source of electrons in AlGaN/GaN heterostructure field effect transistors,* Applied Physics Letters **77**, 250 (2000).

[11] I. P. Smorchkova, C. R. Elsass, J. P. Ibbetson, R. Vetury, B. Heying, P. Fini, E. Haus, S. P. DenBaars, J. S. Speck, and U. K. Mishra, *Polarization-induced charge and electron mobility in AlGaN/GaN heterostructures grown by plasma-assisted molecular-beam epitaxy,* Journal of Applied Physics **86**, 4520 (1999).

[12] M. Asif Khan, A. Bhattarai, J. N. Kuznia, and D. T. Olson, *High electron mobility transistor based on a* $GaN-Al_xGa_{1-x}N$ *heterojunction,* Applied Physics Letters **63**, 1214 (1993).

[13] B. Luther, S. Wolter, and S. Mohney, *High temperature Pt Schottky diode gas sensors on n-type GaN,* Sensors and Actuators B: Chemical **56**, 164 (1999).

[14] J. Schalwig, G. Müller, O. Ambacher, and M. Stutzmann, *Group-III-Nitride Based Gas Sensing Devices,* physica status solidi (a) **185**, 39 (2001).

[15] J. Schalwig, G. Müller, M. Eickhoff, O. Ambacher, and M. Stutzmann, *Gas sensitive GaN/AlGaN-heterostructures,* Sensors and Actuators B: Chemical **87**, 425 (2002).

[16] B. S. Kang, F. Ren, B. P. Gila, C. R. Abernathy, and S. J. Pearton, *AlGaN/GaN-based metal–oxide–semiconductor diode-based hydrogen gas sensor,* Applied Physics Letters **84**, 1123 (2004).

[17] J. Kim, B. Gila, C. Abernathy, G. Chung, F. Ren, and S. Pearton, *Comparison of Pt/GaN and Pt/4H-SiC gas sensors,* Solid-State Electronics **47**, 1487 (2003).

[18] B. S. Kang, S. Kim, F. Ren, K. Ip, Y. W. Heo, B. Gila, C. R. Abernathy, D. P. Norton, and S. J. Pearton, *Detection of* C_2H_4 *Using Wide-Bandgap Semiconductor Sensors : AlGaN/GaN MOS Diodes and Bulk ZnO Schottky Rectifiers,* Journal of The Electrochemical Society **151**, G468 (2004).

[19] B. S. Kang, R. Mehandru, S. Kim, F. Ren, R. C. Fitch, J. K. Gillespie, N. Moser, G. Jessen, T. Jenkins, R. Dettmer, D. Via, A. Crespo, B. P. Gila, C. R. Abernathy, and S. J. Pearton, *Hydrogen-induced reversible changes in drain current in* Sc_2O_3*/AlGaN/GaN high electron mobility transistors,* Applied Physics Letters **84**, 4635 (2004).

[20] H.-T. Wang, T. J. Anderson, F. Ren, C. Li, Z.-N. Low, J. Lin, B. P. Gila, S. J. Pearton, A. Osinsky, and A. Dabiran, *Robust detection of hydrogen using differential AlGaN/GaN high electron mobility transistor sensing diodes,* Applied Physics Letters **89**, 242111 (2006).

[21] J. Song, W. Lu, J. S. Flynn, and G. R. Brandes, *Pt-AlGaN/GaN Schottky diodes operated at* 800 °C *for hydrogen sensing,* Applied Physics Letters **87**, 133501 (2005).

[22] J. Song, W. Lu, J. S. Flynn, and G. R. Brandes, *AlGaN/GaN Schottky diode hydrogen sensor performance at high temperatures with different catalytic metals,* Solid-State Electronics **49**, 1330 (2005).

[23] J.-R. Huang, W.-C. Hsu, Y.-J. Chen, T.-B. Wang, K.-W. Lin, H.-I. Chen, and W.-C. Liu, *Comparison of hydrogen sensing characteristics for Pd/GaN and Pd/*$Al_0.3Ga_0.7As$ *Schottky diodes,* Sensors and Actuators B: Chemical **117**, 151 (2006).

[24] W. C. Hsu, J.-R. Huang, K.-W. Lin, H.-I. Chen, and W.-C. Liu, *High Performance GaN-based Hydrogen Sensors,* ECS Transactions **6**, 163 (2007).

[25] T.-H. Tsai, J.-R. Huang, K.-W. Lin, C.-W. Hung, W.-C. Hsu, H.-I. Chen, and W.-C. Liu, *Improved Hydrogen-Sensing Properties of a Pt/SiO2/GaN Schottky Diode,* **10**, J158 (2007).

[26] Y.-Y. Tsai, K.-W. Lin, H.-I. Chen, I.-P. Liu, C.-W. Hung, T.-P. Chen, T.-H. Tsai, L.-Y. Chen, K.-Y. Chu, and W.-C. Liu, *Hydrogen sensing properties of a Pt-oxide-GaN Schottky diode,* Journal of Applied Physics **104**, 024515 (2008).

[27] J.-T. Yan and C.-T. Lee, *Improved detection sensitivity of Pt/*$\beta-Ga_2O_3$*/GaN hydrogen sensor diode,* Sensors and Actuators B: Chemical **143**, 192 (2009).

[28] J. Song and W. Lu, *Operation of Pt/AlGaN/GaN-Heterojunction Field-Effect-Transistor Hydrogen Sensors With Low Detection Limit and High Sensitivity,* IEEE Electron Device Letters **29**, 1193 (2008).

[29] Y.-L. Wang, F. Ren, U. Zhang, Q. Sun, C. D. Yerino, T. S. Ko, Y. S. Cho, I. H. Lee, J. Han, and S. J. Pearton, *Improved hydrogen detection sensitivity in N-polar GaN Schottky diodes,* Applied Physics Letters **94**, 212108 (2009).

[30] Y.-L. Wang, B. Chu, C. Chang, K. Chen, Y. Zhang, Q. Sun, J. Han, S. Pearton, and F. Ren, *Hydrogen sensing of N-polar and Ga-polar GaN Schottky diodes,* Sensors and Actuators B: Chemical **142**, 175 (2009).

[31] Y.-L. Wang, F. Ren, W. Lim, S. Pearton, K. H. Baik, S.-M. Hwang, Y. G. Seo, and S. Jang, *Hydrogen sensing characteristics of non-polar a-plane GaN Schottky diodes,* Current Applied Physics **10**, 1029 (2010).

[32] K. Hyeon Baik, H. Kim, S.-N. Lee, E. Lim, S. J. Pearton, F. Ren, and S. Jang, *Hydrogen sensing characteristics of semipolar ($11\bar{2}2$) GaN Schottky diodes,* Applied Physics Letters **104**, 072103 (2014).

[33] T.-Y. Chen, H.-I. Chen, C.-C. Huang, C.-S. Hsu, P.-S. Chiu, P.-C. Chou, and W.-C. Liu, *Improved hydrogen-sensing performance of a Pd/GaN Schottky diode with a surface plasma treatment approach,* Sensors and Actuators B: Chemical **159**, 159 (2011).

[34] C. Huang, H. Chen, T. Chen, C. Hsu, C. Chen, P. Chou, J. Liou, and W. Liu, *On an Electroless Plating (EP)-Based Pd/AlGaN/GaN Heterostructure Field-Effect Transistor (HFET)-Type Hydrogen Gas Sensor,* IEEE Electron Device Letters **33**, 788 (2012).

[35] C.-C. Chen, H.-I. Chen, I.-P. Liu, P.-C. Chou, J.-K. Liou, C.-C. Huang, and W.-C. Liu, *Hydrogen sensing characteristics of a Pt/AlGaN/GaN heterostructure field-effect transistor (HFET) prepared by sensitization, activation, and electroless plating (EP) approaches,* Sensors and Actuators B: Chemical **212**, 127 (2015).

[36] C.-C. Chen, H.-I. Chen, I.-P. Liu, P.-C. Chou, J.-K. Liou, Y.-J. Chiou, H.-Y. Liu, and W.-C. Liu, *On a transistor-type hydrogen gas sensor prepared by an electrophoretic deposition (EPD) approach,* International Journal of Hydrogen Energy **39**, 13320 (2014).

[37] H. Kim and S. Jang, *AlGaN/GaN HEMT based hydrogen sensor with platinum nanonetwork gate electrode,* Current Applied Physics **13**, 1746 (2013).

[38] P.-C. Chou, H.-I. Chen, I.-P. Liu, W.-C. Chen, C.-C. Chen, J.-K. Liou, C.-J. Lai, and W.-C. Liu, *On a Schottky diode-type hydrogen sensor with pyramid-like Pd nanostructures,* International Journal of Hydrogen Energy **40**, 9006 (2015).

[39] P.-C. Chou, H.-I. Chen, I.-P. Liu, C.-C. Chen, J.-K. Liou, C.-J. Lai, and W.-C. Liu, *Hydrogen sensing characteristics of Pd/SiO2-nanoparticles (NPs)/AlGaN metal-oxide-semiconductor (MOS) diodes,* International Journal of Hydrogen Energy **39**, 20313 (2014).

[40] C. F. Lo, C. Y. Chang, B. H. Chu, S. J. Pearton, A. Dabiran, P. P. Chow, and F. Ren, *Effect of humidity on hydrogen sensitivity of Pt-gated AlGaN/GaN high electron mobility transistor based sensors,* Applied Physics Letters **96**, 232106 (2010).

[41] S. Jung, K. H. Baik, F. Ren, S. J. Pearton, and S. Jang, *Pt-AlGaN/GaN Hydrogen Sensor With Water-Blocking PMMA Layer,* IEEE Electron Device Letters **38**, 657 (2017).

[42] S. Jung, K. H. Baik, F. Ren, S. J. Pearton, and S. Jang, *Temperature and Humidity Dependence of Response of PMGI-Encapsulated Pt-AlGaN/GaN Diodes for Hydrogen Sensing,* IEEE Sensors Journal **17**, 5817 (2017).

[43] C. Y. Chang, B. S. Kang, H. T. Wang, F. Ren, Y. L. Wang, S. J. Pearton, D. M. Dennis, J. W. Johnson, P. Rajagopal, J. C. Roberts, E. L. Piner, and K. J. Linthicum, *CO_2 detection using polyethylenimine/starch functionalized AlGaN/GaN high electron mobility transistors,* Applied Physics Letters **92**, 232102 (2008).

[44] G. Zhao, W. Sutton, D. Pavlidis, E. L. Piner, J. Schwank, and S. Hubbard, *A novel Pt-AlGaN/GaN heterostructure Schottky diode gas sensor on Si,* Ieice Transactions on Electronics **86**, 2027 (2003).

[45] S. C. Hung, C. W. Chen, C. Y. Shieh, G. C. Chi, R. Fan, and S. J. Pearton, *High sensitivity carbon monoxide sensors made by zinc oxide modified gated GaN/AlGaN high electron mobility transistors under room temperature,* Applied Physics Letters **98**, 223504 (2011).

[46] C.-F. Lo, L. Liu, B.-H. Chu, F. Ren, S. J. Pearton, S. Doré, C.-H. Hsu, J. Kim, A. M. Dabiran, and P. P. Chow, *Carbon monoxide detection sensitivity of ZnO nanorod-gated AlGaN/GaN high electron mobility transistors in different temperature environments,* Journal of Vacuum Science & Technology B **30**, 010606 (2012).

[47] T.-Y. Chen, H.-I. Chen, Y.-J. Liu, C.-C. Huang, C.-S. Hsu, C.-F. Chang, and W.-C. Liu, *Ammonia sensing characteristics of a Pt/AlGaN/GaN Schottky diode,* Sensors and Actuators B: Chemical **155**, 347 (2011).

[48] T. Chen, H. Chen, C. Hsu, C. Huang, C. Chang, P. Chou, and W. Liu, *On an Ammonia Gas Sensor Based on a Pt/AlGaN Heterostructure Field-Effect Transistor,* IEEE Electron Device Letters **33**, 612 (2012).

[49] P.-C. Chou, H.-I. Chen, I.-P. Liu, C.-W. Hung, C.-C. Chen, J.-K. Liou, and W.-C. Liu, *Study of an electroless plating (EP)-based Pt/AlGaN/GaN Schottky diode-type ammonia sensor,* Sensors and Actuators B: Chemical **203**, 258 (2014).

[50] S. Jung, K. H. Baik, F. Ren, S. J. Pearton, and S. Jang, *Detection of ammonia at low concentrations (0.1–2 ppm) with ZnO nanorod-functionalized AlGaN/GaN high electron mobility transistors,* Journal of Vacuum Science & Technology B **35**, 042201 (2017).

[51] Y.-L. Wang, C. Y. Chang, W. Lim, S. J. Pearton, D. P. Norton, B. H. Chu, C. F. Lo, F. Ren, J. W. Johnson, P. Rajagopal, J. C. Roberts, E. L. Piner, and K. J. Linthicum, *Oxygen gas sensing at low temperature using indium zinc oxide-gated AlGaN/GaN high electron mobility transistors,* Journal of Vacuum Science & Technology B **28**, 376 (2010).

[52] S.-T. Hung, C.-J. Chang, C. C. Chen, C. F. Lo, F. Ren, S. J. Pearton, and I. I. Kravchenko, *SnO_2-gated AlGaN/GaN high electron mobility transistors based oxygen sensors,* Journal of Vacuum Science & Technology B **30**, 041214 (2012).

[53] P. Offermans, R. Vitushinsky, M. Crego-Calama, and S. H. Brongersma, *Gas Sensing with AlGaN/GaN 2DEG Channels,* Procedia Engineering **25**, 1417 (2011), eurosensorsXXV.

[54] P. Offermans, R. Vitushinsky, M. Crego-Calama, and S. H. Brongersma, *Ultrasensitive NO2 detection with AlGaN/GaN 2DEG channels for air quality monitoring,* in *SENSORS, 2012 IEEE* (2012) pp. 1–3.

[55] R. Vitushinsky, M. Crego-Calama, S. H. Brongersma, and P. Offermans, *Enhanced detection of NO_2 with recessed AlGaN/GaN open gate structures,* Applied Physics Letters **102**, 172101 (2013).

[56] M. Miyoshi, S. Fujita, and T. Egawa, *Demonstration of NOx gas sensing for Pd/ZnO/GaN heterojunction diodes,* Journal of Vacuum Science & Technology B **33**, 013001 (2015).

[57] Y. Halfaya, C. Bishop, A. Soltani, S. Sundaram, V. Aubry, P. Voss, J.-P. Salvestrini, and A. Ougazzaden, *Investigation of the Performance of HEMT-based NO, NO_2 and NH_3 Exhaust Gas Sensors for Automotive Antipollution Systems,* Sensors **16**, 273 (2016).

[58] V. Tilak, K. Matocha, and P. Sandvik, *Pt/GaN Schottky diodes for harsh environment NO sensing applications,* physica status solidi (c) **2**, 2555 (2005).

[59] Y. Xi, L. Liu, F. Ren, S. J. Pearton, J. Kim, A. Dabiran, and P. P. Chow, *Methane detection using Pt-gated AlGaN/GaN high electron mobility transistor based Schottky diodes,* Journal of Vacuum Science & Technology B **31**, 032203 (2013).

[60] S. Jung, K. H. Baik, F. Ren, S. J. Pearton, and S. Jang, *Silver-Functionalized AlGaN/GaN Heterostructure Diode for Ethanol Sensing,* Journal of The Electrochemical Society **164**, B417 (2017).

[61] S. Keller, *Substrates and materials,* in *Power GaN Devices: Materials, Applications and Reliability*, edited by M. Meneghini, G. Meneghesso, and E. Zanoni (Springer International Publishing, Cham, 2017) pp. 27–52.

[62] L. Shen, S. Heikman, B. Moran, R. Coffie, N. . Zhang, D. Buttari, I. P. Smorchkova, S. Keller, S. P. DenBaars, and U. K. Mishra, *AlGaN/AlN/GaN high-power microwave HEMT,* IEEE Electron Device Letters **22**, 457 (2001).

[63] E. T. Yu, X. Z. Dang, L. S. Yu, D. Qiao, P. M. Asbeck, S. S. Lau, G. J. Sullivan, K. S. Boutros, and J. M. Redwing, *Schottky barrier engineering in III–V nitrides via the piezoelectric effect,* Applied Physics Letters **73**, 1880 (1998).

[64] A. Taube, E. Kamińska, M. Kozubal, J. Kaczmarski, W. Wojtasiak, J. Jasiński, M. A. Borysiewicz, M. Ekielski, M. Juchniewicz, J. Grochowski, M. Myśliwiec, E. Dynowska, A. Barcz, P. Prystawko, M. Zając, R. Kucharski, and A. Piotrowska, *Ion implantation for isolation of AlGaN/GaN HEMTs using C or Al,* physica status solidi (a) **212**, 1162 (2015), https://onlinelibrary.wiley.com/doi/pdf/10.1002/pssa.201431724 .

[65] M. E. Lin, Z. Ma, F. Y. Huang, Z. F. Fan, L. H. Allen, and H. Morkoç, *Low resistance ohmic contacts on wide band-gap GaN,* Applied Physics Letters **64**, 1003 (1994).

[66] Z. Fan, S. N. Mohammad, W. Kim, z. Aktas, A. E. Botchkarev, and H. Morkoç, *Very low resistance multilayer Ohmic contact to n-GaN,* Applied Physics Letters **68**, 1672 (1996).

[67] F. M. Mohammed, L. Wang, I. Adesida, and E. Piner, *The role of barrier layer on Ohmic performance of Ti/Al-based contact metallizations on AlGaN/GaN heterostructures,* Journal of Applied Physics **100**, 023708 (2006).

[68] G. Greco, F. Iucolano, and F. Roccaforte, *Ohmic contacts to Gallium Nitride materials,* Applied Surface Science **383**, 324 (2016).

[69] B. Jacobs, M. Kramer, E. Geluk, and F. Karouta, *Optimisation of the Ti/Al/Ni/Au ohmic contact on AlGaN/GaN FET structures,* Journal of Crystal Growth **241**, 15 (2002).

[70] G. K. Reeves and H. B. Harrison, *Obtaining the specific contact resistance from transmission line model measurements,* IEEE Electron Device Letters **3**, 111 (1982).

[71] J. H. Klootwijk and C. E. Timmering, *Merits and limitations of circular TLM structures for contact resistance determination for novel III-V HBTs,* in *Proceedings of*

the 2004 International Conference on Microelectronic Test Structures (IEEE Cat. No.04CH37516) (2004) pp. 247–252.

[72] R. Sohal, P. Dudek, and O. Hilt, *Comparative study of NH_4OH and HCl etching behaviours on AlGaN surfaces,* Applied Surface Science **256**, 2210 (2010).

[73] L. Wang, F. M. Mohammed, and I. Adesida, *Differences in the reaction kinetics and contact formation mechanisms of annealed Ti/Al/Mo/Au Ohmic contacts on n-GaN and AlGaN/GaN epilayers,* Journal of Applied Physics **101**, 013702 (2007).

[74] F. Iucolano, G. Greco, and F. Roccaforte, *Correlation between microstructure and temperature dependent electrical behavior of annealed Ti/Al/Ni/Au Ohmic contacts to AlGaN/GaN heterostructures,* Applied Physics Letters **103**, 201604 (2013).

[75] A. Shriki, R. Winter, Y. Calahorra, Y. Kauffmann, G. Ankonina, M. Eizenberg, and D. Ritter, *Formation mechanism of gold-based and gold-free ohmic contacts to AlGaN/GaN heterostructure field effect transistors,* Journal of Applied Physics **121**, 065301 (2017).

[76] L. Wang, M. I. Nathan, T. Lim, M. A. Khan, and Q. Chen, *High barrier height GaN Schottky diodes: Pt/GaN and Pd/GaN,* Applied Physics Letters **68**, 1267 (1996).

3

AlGaN/GaN HEMT sensor layout optimization

This chapter focuses on design and layout optimization of Pt-AlGaN/GaN HEMT-sensors. The impact of sensor geometry was analysed in order to enhance hydrogen sensing performance. The gas testing methodology and experimental setup that includes software controlled MFCs and sealed chamber with temperature control is presented. Sensors with gate width and length ratios W_g/L_g from 0.25 to 10 were designed, fabricated and tested for the detection of hydrogen gas at 200 °C. Sensing response, drain current variation and transient response were found to be directly related to the sensor gate electrode W_g/L_g ratio. The obtained results demonstrated a 2.2x increase in sensing response and 46.3x increase in sensing current variation at 500 ppm H_2 when W_g/L_g went from 0.25 to 10. In addition, the detection limit was lowered to 5 ppm. Transient characteristics demonstrated faster sensor response to H_2, but slower recovery rates with increasing ratio. Design improvements for 2nd device generation were made based on the obtained results.

Parts of this chapter have been published in 2017 IEEE SENSORS, (2017)[1].

3.1. SENSOR PHOTOLITHOGRAPHY MASK DESIGN

A new set of photolithography masks was designed with several sensor geometries. For the first sensor generation masks were fabricated on 4 inch reticles. A single die size was 7 mm × 7 mm. It contains 14 individual chips with dimensions of 3.5 mm × 1 mm as shown in fig. 3.1. The active area of each chip is on the top part and the bonding pads for interconnection with testing the PCB are at the bottom. The top row contains sensors with the metal sensing gate of different geometries. The bottom row are gateless 2-terminal structures that are applicable to chemical or pH sensors. The length of chips was extended to ease handling and packaging as well as to prevent shorts in case of testing in liquids. The bottom right chip contains numerous test structures for material and fabrication process characterization. These include TLM and CTLM for contact resistance measurements, metal sheet resistance test structures for all metal layers, Hall measurement structures, mesa isolation leakage test structures, small size HEMTs and metal-oxide-metal capacitors.

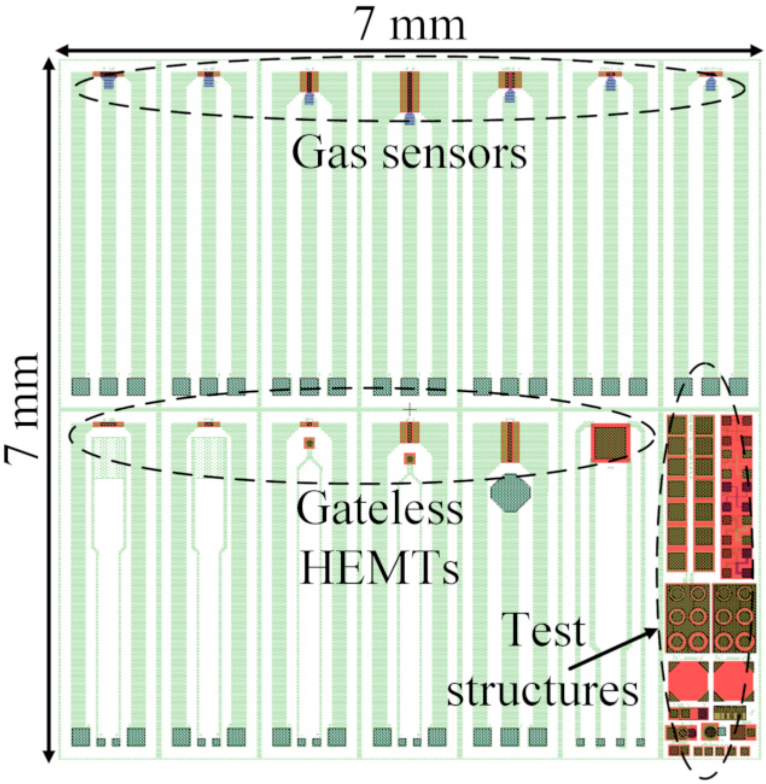

Figure 3.1: Layout of a single die of the HEMT sensor photolithography mask.

A schematic view of a AlGaN/GaN HEMT or sensor with specific geometry parameters is demonstrated in fig. 3.2. The design parameters are the gate length L_g and width W_g, gate to source distance L_{gs} and gate to drain distance L_{gd}. Gate electrode dimensions directly impact the drain-source current (I_{DS}) magnitude and extrinsic transconductance (g_m) of any FET device including HEMT (see eqs. (1.14) and (1.15)) according to:

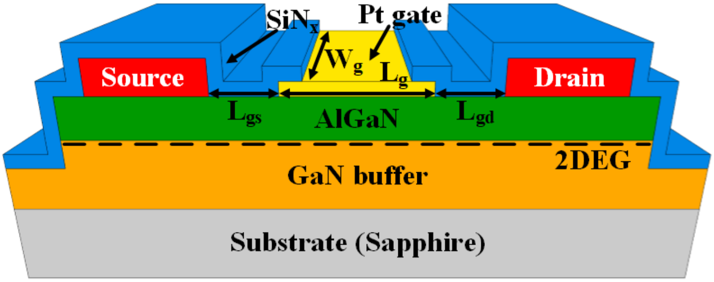

Figure 3.2: Schematic cross section of AlGaN/GaN HEMT with indicated physical parameters.

$$I_{DS}; g_m \propto \frac{W_g}{L_g} \tag{3.1}$$

Therefore higher W_g/L_g ratios result in increased output current and transconductance. AlGaN/GaN sensors with various gate electrode dimensions have been previously demonstrated. Large gate area devices have been reported in [2–4] with W_g/L_g ratios of 7, 1 or 5 respectively, while others [5, 6] used typical HEMT layouts with a few micron gate length and large width resulting in ratios on the order of 50 to 100. However the reasons for the design choices were not stated.

It is therefore of great interest to investigate how layout design can be optimized in terms of sensing response, signal variation magnitude and transient response. Previously, the effects of gate length for hydrogen sensor based on GaN MESFET were reported in [7]. The obtained results showed that longer gate and consequently larger gate area (lower W_g/L_g) resulted in higher variation of the sensing signal. However, unlike conventional FET, their device did not exhibit saturation across entire bias range and operated only in the resistive region. AlGaN/GaN HEMT sensor layout modelling was performed by [8] in order to determine the optimal design. The results suggested that there is a trade-off between device sensing response (S) and absolute signal variation (ΔI) with larger W_g/L_g resulting in lower S and increased ΔI. Based on their model the optimal design was fabricated with gate dimensions 2 µm × 200 µm ($L_g \times W_g$) while different geometries were not tested.

3.2. HYDROGEN RESPONSE WITH DIFFERENT SENSOR DESIGNS

To investigate the impact of Pt-AlGaN/GaN HEMT sensor geometry on sensing response, current variation and transient characteristics, structures with increasing W_g/L_g ratios of 0.25, 0.5, 5 and 10 have been included in the 1st generation mask set. The studied sensing gate geometries were designed by extending multiples of a 40 µm × 40 µm single cell either length ($W_g/L_g < 1$) or width ($W_g/L_g > 1$) wise. The fabricated devices with $W_g/L_g = 0.25$ to $W_g/L_g = 10$ are shown in fig. 3.3. The gate-source (L_{gs}) and gate-drain (L_{gd}) distances were set at 6 µm for every device. Electrode ratios are defined based on the gate area exposed to the ambient, while the actual gate length footprint was 8 µm longer for all geometries, to allow edge encapsulation with SiN_x for improving gate electrode adhesion. H_2 was chosen as the test gas for geometry optimization study since it

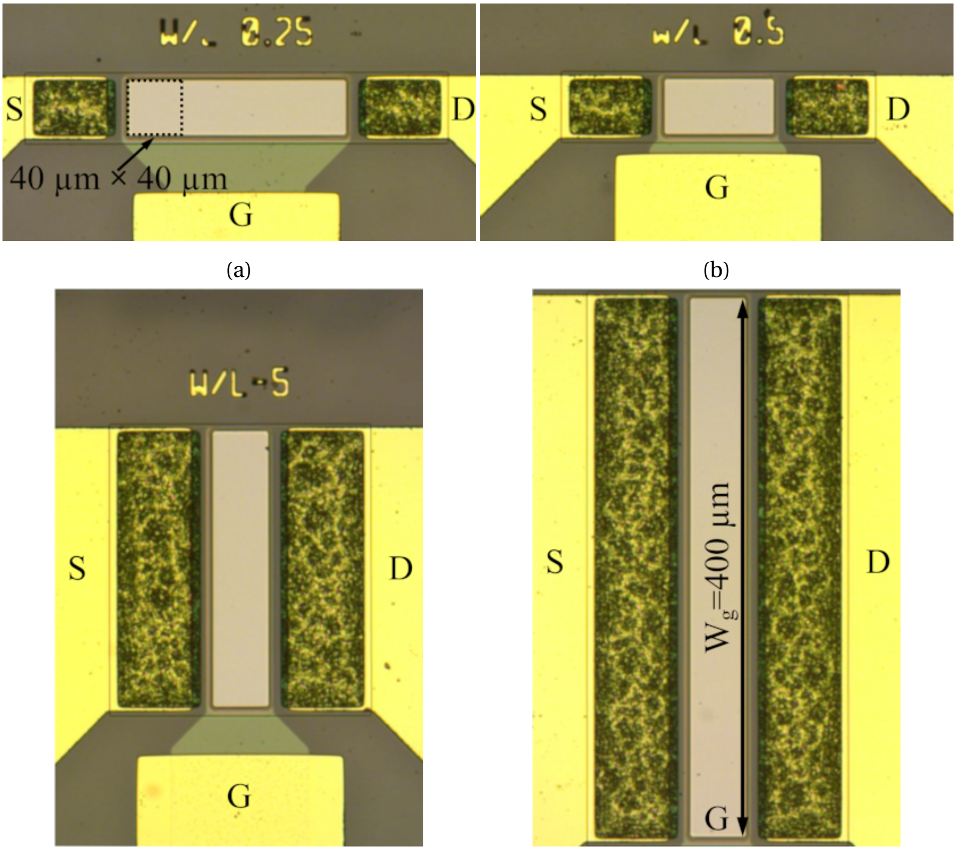

(a) (b) (c) (d)

Figure 3.3: Fabricated AlGaN/GaN HEMT sensors with W_g/L_g of (a) 0.25, (b) 0.5, (c) 5, (d) 10.

is considered to be a source of renewable energy for future automotive, aerospace industries, fuel cells and as replacement of fossil fuels. H_2 is also widely used by chemical, manufacturing industries and in food processing. On the other hand, it is a colourless, odourless gas and is flammable if concentration exceeds 4 %. Continuous H_2 monitoring down to ppm concentrations is therefore crucial for industrial process monitoring, leakage detection and safety.

Gas testing experiments were conducted using a gas mixing system from Beijing Elite Tech Co. The testing system schematic is shown in fig. 3.4. It contains software controlled mass flow controllers that precisely set the specified gas concentration, flow rate and duration. Dilute H_2 gas in N_2 was supplied by a local vendor in steel gas cylinders. The sensors chips, mounted on ceramic PCBs, were loaded inside a stainless steel test chamber connected to gas supply lines. The chamber has a temperature controlled hotplate, temperature and humidity sensors, probe needles and electrical feedthroughs. The testing temperature was fixed at 200 °C and the hydrogen concertation range was warried form 5 ppm to 500 ppm in dry synthetic air (O_2/N_2=21 %/79 %) as background gas. The total gas flow rate was fixed at 300 sccm during all experiments. Sensor characteristics were measured using a pair of Keithley 2450 source meters controlled using PC software.

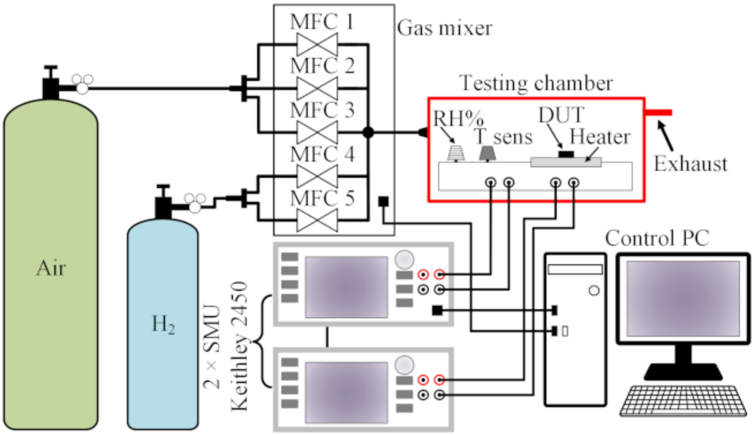

Figure 3.4: Block diagram of the gas sensor characterization system.

The output characteristics ($I_{DS} - V_{DS}$) of the studied Pt-AlGaN/GaN sensors with different gate geometries at 30 °C are shown in fig. 3.5. Proper FET operation with clearly identifiable triode and saturation regions was obtained for all gate ratios. The corresponding transfer characteristics ($I_{DS} - V_{GS}$) are shown in fig. 3.6. The HEMTs are depletion mode as the threshold voltage is negative and they are in the on state at $V_{GS} = 0\,\mathrm{V}$.

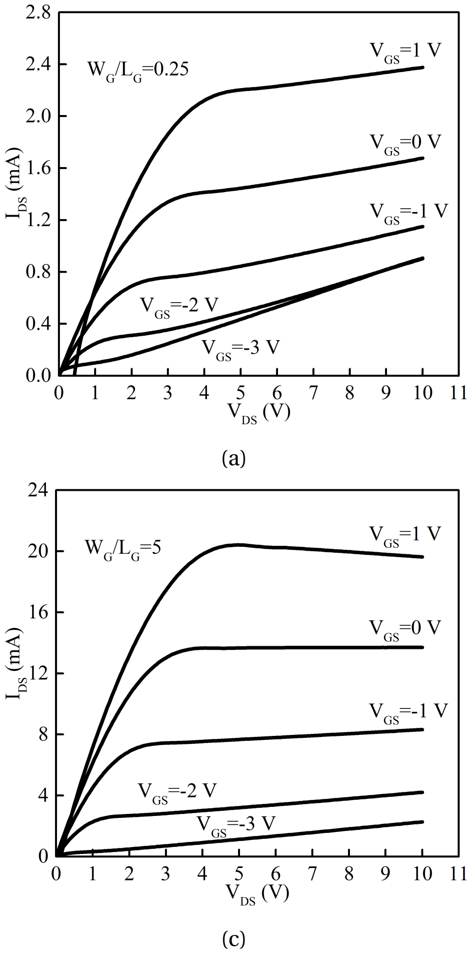

(a) (b)

(c) (d)

Figure 3.5: Sensor output characteristics ($I_{DS} - V_{DS}$) at 30 °C with W_g/L_g of (a) 0.25, (b) 0.5, (c) 5, (d) 10.

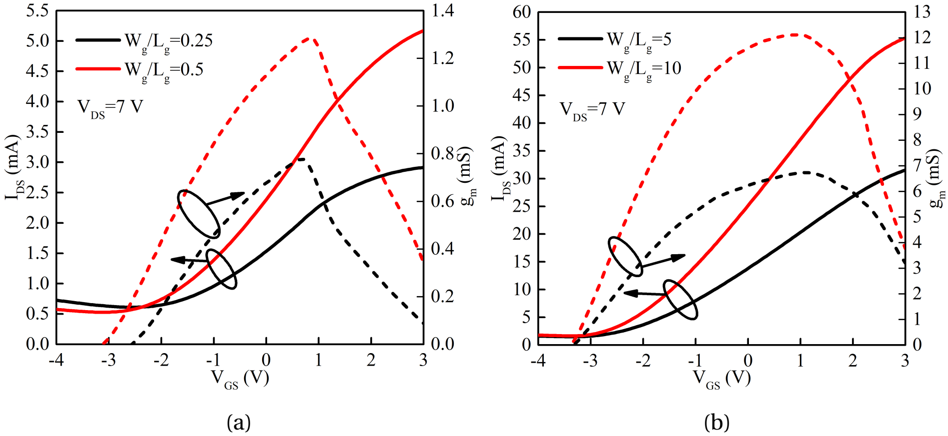

(a) (b)

Figure 3.6: Sensor transfer characteristics ($I_{DS} - V_{GS}$) at 30 °C with W_g/L_g of (a) 0.25, 0.5 and (b) 5, 10.

The drain saturation current and transconductance have increased with increasing the W_g/L_g ratio as expected according to eq. (3.1).

The sensors maintained transistor like operation at 200 °C. The output characteristics of the studied Pt-AlGaN/GaN sensors with different gate geometries exposed to H_2 gas at V_{GS}=0 V are shown in fig. 3.7. Drain current increase with increasing H_2 concentration is evident. The detection mechanism is attributed to catalytic dissociation of hy-

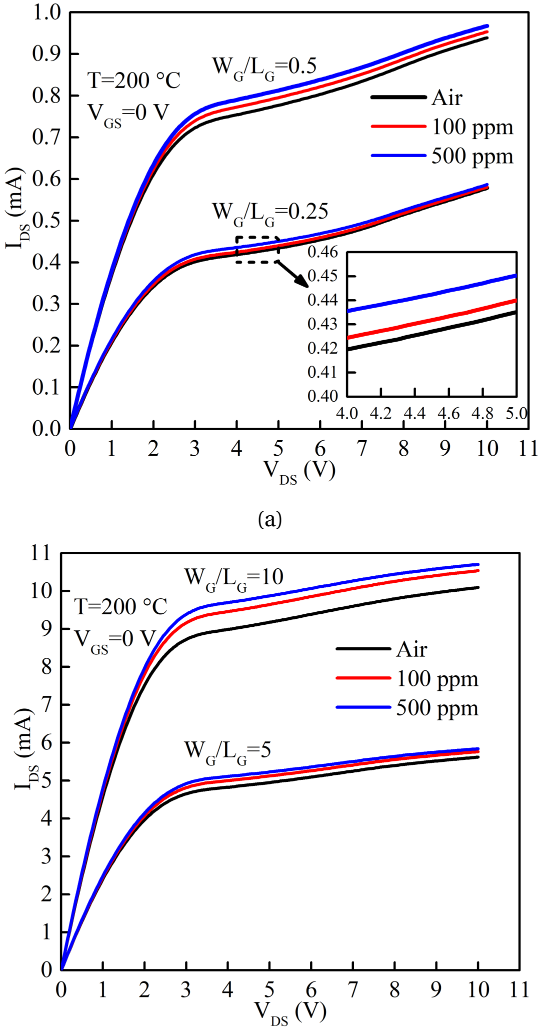

(a)

(b)

Figure 3.7: Drain current versus drain-source voltage characteristics of the HEMT sensors upon exposure to H_2 gas in air with W_g/L_g (a) 0.25, 0.5 and (b) 5, 10.

drogen molecules at the Pt-gate surface, followed by H atom diffusion through the metal. A dipole layer forms at the interface resulting in the lowering of the Schottky barrier [9].

To evaluate the impact of W_g/L_g ratio on the sensing characteristics of HEMT-sensors, drain current variation:

$$\Delta I_{DS} = I_{DS,\mathrm{H}_2} - I_{DS,air} \tag{3.2}$$

and sensing response:

$$S = \frac{I_{DS,\mathrm{H}_2} - I_{DS,air}}{I_{DS}} \times 100\% \tag{3.3}$$

where I_{DS,H_2} and $I_{DS,air}$ are drain current values in H_2 containing and pure air ambient were extracted at $V_{DS} = 5\,\mathrm{V}$ and $V_{GS} = 0\,\mathrm{V}$ and are shown in fig. 3.8. Both S and ΔI_{DS} increased with increasing W_g/L_g. These findings appear to differ from modeling results of [8], that predicted reduction in sensing response with shorter L_g. In our case however, the higher S could be attributed to a lesser increase in baseline current value. ΔI_{DS} increases due to a higher baseline I_{DS}. For 500 ppm H_2 concentration the S increased from 3.5 % for $W_g/L_g = 0.25$ to 7.6 % for $W_g/L_g = 10$ (2.2x increase), while ΔI_{DS} increased from 15 µA to 695 µA (46.3x increase). These results clearly demonstrate that larger W_g/L_g will result in superior DC performance of the HEMT sensor. One additional consideration for HEMT sensor design is that power consumption will increase due to higher current flowing through the HEMT with larger W_g/L_g. However, the 3 terminal FET type sensor allows to tune the operating point via gate and drain bias voltage to optimize the sensing or power consumption characteristics [4].

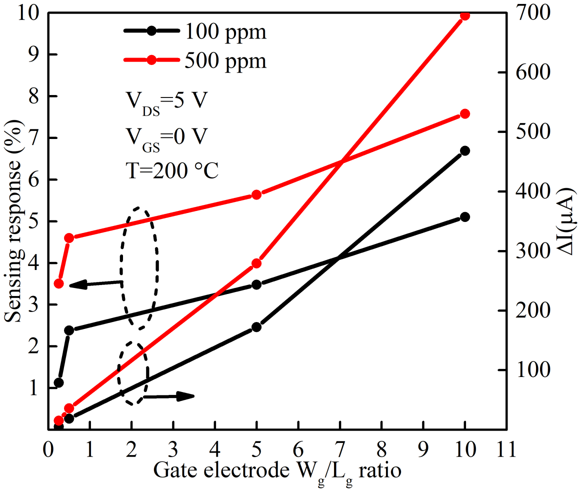

Figure 3.8: HEMT-sensor sensing response and sensing current variation dependency on the gate electrode W_g/L_g ratio.

Transient characteristics of the studied geometries were tested in order to determine H_2 gas detection limits, as well as the response and recovery rates. Figure 3.9 shows drain current variation with time ($I_{DS} - t$) for the studied sensors with increasing H_2 concentration in the range of 5 ppm to 500 ppm. Gas was supplied for 25 min for each injection cycle and purged with dry air until the signal recovered to the baseline level. Structure with $W_g/L_g = 0.25$ had a detection limit above 20 ppm, while below this concentration the sensing response was not distinguishable from signal noise and some baseline drift. For a $W_g/L_g = 0.5$ the sensor was able to detect 20 ppm H_2, but not 5 ppm, while for

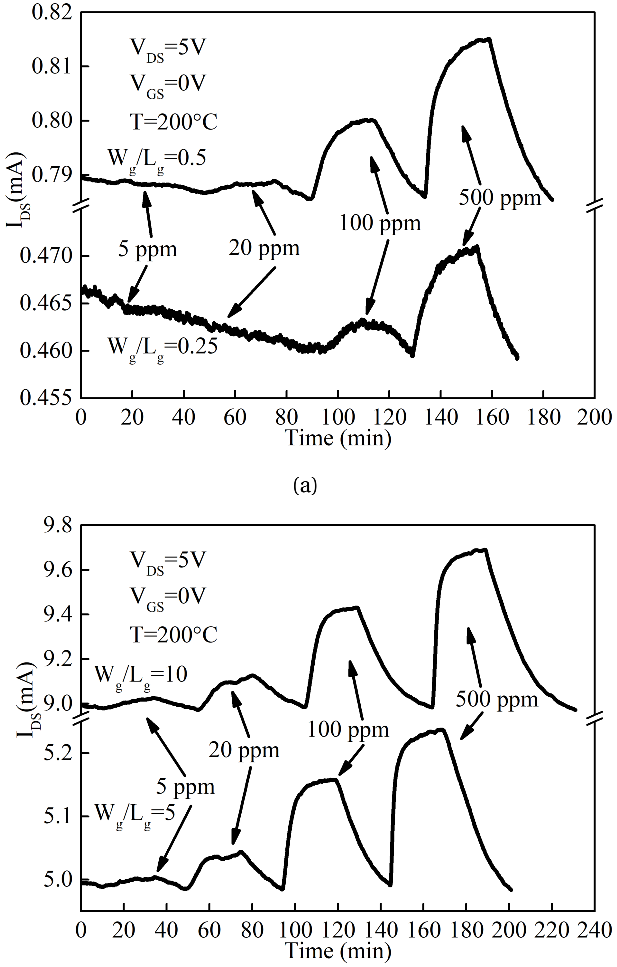

(a)

(b)

Figure 3.9: Transient response of the HEMT sensors with (a) $W_g/L_g < 1$ and (b) $W_g/L_g > 1$ to various H_2 gas concentrations.

$W_g/L_g > 1$ the sensors were sensitive across the entire tested range. Sensing dynamics of all structures, at 500 ppm concentration, were compared using rise (t_R) and fall (t_F) times, defined as the time required for the signal to rise/fall from 10 % to 90 % of the steady state. The response time (t_R) reduced with increasing W_g/L_g, while the recovery (t_F) time increased as shown in table 3.1. Therefore, by optimizing the sensor geometry the response characteristics can be tuned to comply with application requirements.

Table 3.1: Transient parameters of the studied sensor layouts.

Ratio W_g/L_g	**t_R (min)**	**t_F (min)**
0.25	13.7	11.55
0.5	11.95	17.45
5	7.05	21.2
10	5.7	25.65

3.3. DESIGN OF 2ND GENERATION SENSORS

Based on the above results photolithography mask re-design was carried out to further improve sensing performance in accordance with the requirements of Shenzhen cleanroom. A single die of the 2^{nd} generation HEMT sensor mask is shown in fig. 3.10. Devices with larger W_g/L_g ratios up to 100 were added in order to increase the magnitude of the

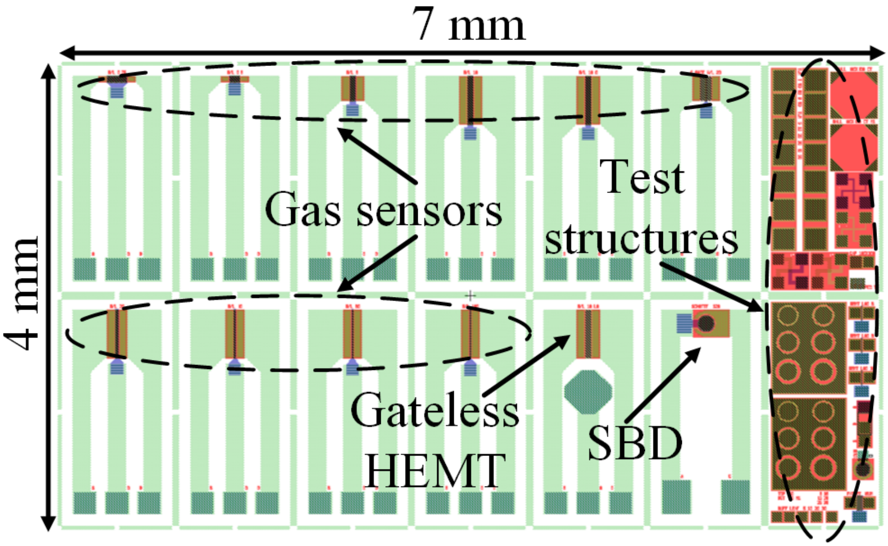

Figure 3.10: Layout of the 2^{nd} generation single die of the HEMT sensor photolithography mask.

sensing signal variation. Most of the gateless structures were removed and a SBD device was included. The chip length was reduced to 2 mm in order to fit more devices per wafer, while maintaining ease of packaging.

3.4. CONCLUSIONS

In this chapter the design of AlGaN/GaN sensor layout was analyzed. The parameters that impact device characteristics are gate dimensions W_g and L_g and spacings between source, gate and drain electrodes. Mask layout was designed with extended interconnections in order to simplify packaging for gas testing. Testing equipment and testing methodology were introduced. Afterwards, the effects of gate electrode geometry on the H_2 gas detection performance of Pt-AlGaN/GaN HEMT sensors with varying W_g/L_g ratios was studied. A significant increase in sensing response of 2.2x and signal variation of 46.3x was measured with larger ratio devices. W_g/L_g ratios >1 enabled the detection of H_2 across the entire tested range (5 ppm–500 ppm). Transient characteristics demonstrated a trade-off between response and recovery times with larger W_g/L_g leading to faster response to H_2, but a slower signal recovery to the baseline value. Based on these results a new set of photolithography masks was designed with larger W_g/L_g ratios to further enhance signal variation.

REFERENCES

[1] R. Sokolovskij, E. Iervolino, C. Zhao, F. Wang, H. Yu, F. Santagata, P. M. Sarro, and G. Q. Zhang, *Pt-AlGaN/GaN HEMT-sensor layout optimization for enhancement of hydrogen detection,* in *2017 IEEE SENSORS* (2017) pp. 1–3.

[2] J. Schalwig, G. Müller, M. Eickhoff, O. Ambacher, and M. Stutzmann, *Gas sensitive GaN/AlGaN-heterostructures,* Sensors and Actuators B: Chemical **87**, 425 (2002).

[3] M. Jaegle and K. Steiner, *Gas-sensitive GaAs-MESFETs,* Sensors and Actuators B: Chemical **34**, 543 (1996).

[4] J. Song and W. Lu, *Operation of Pt/AlGaN/GaN-Heterojunction Field-Effect-Transistor Hydrogen Sensors With Low Detection Limit and High Sensitivity,* IEEE Electron Device Letters **29**, 1193 (2008).

[5] B. S. Kang, R. Mehandru, S. Kim, F. Ren, R. C. Fitch, J. K. Gillespie, N. Moser, G. Jessen, T. Jenkins, R. Dettmer, D. Via, A. Crespo, B. P. Gila, C. R. Abernathy, and S. J. Pearton, *Hydrogen-induced reversible changes in drain current in Sc_2O_3/AlGaN/GaN high electron mobility transistors,* Applied Physics Letters **84**, 4635 (2004).

[6] C. Huang, H. Chen, T. Chen, C. Hsu, C. Chen, P. Chou, J. Liou, and W. Liu, *On an Electroless Plating (EP)-Based Pd/AlGaN/GaN Heterostructure Field-Effect Transistor (HFET)-Type Hydrogen Gas Sensor,* IEEE Electron Device Letters **33**, 788 (2012).

[7] T. Higuchi, S. Nakagomi, and Y. Kokubun, *Field effect hydrogen sensor device with simple structure based on GaN,* Sensors and Actuators B: Chemical **140**, 79 (2009).

[8] C. Bishop, Y. Halfaya, A. Soltani, S. Sundaram, X. Li, J. Streque, Y. El Gmili, P. L. Voss, J. P. Salvestrini, and A. Ougazzaden, *Experimental Study and Device Design of NO, NO_2, and NH_3 Gas Detection for a Wide Dynamic and Large Temperature Range Using Pt/AlGaN/GaN HEMT,* IEEE Sensors Journal **16**, 6828 (2016).

[9] J. Schalwig, G. Müller, U. Karrer, M. Eickhoff, O. Ambacher, M. Stutzmann, L. Görgens, and G. Dollinger, *Hydrogen response mechanism of Pt–GaN Schottky diodes,* Applied Physics Letters **80**, 1222 (2002).

4

H_2S detection properties of Pt-gated AlGaN/GaN HEMT-sensor

In this chapter AlGaN/GaN high electron mobility transistor (HEMT)-based sensors with catalytic platinum gate were micro-fabricated on commercially available epitaxial wafers and extensively characterized for ppm level hydrogen sulfide (H_2S) detection for industrial safety applications. As fabricated devices exhibited sensing signal saturation at 30 ppm H_2S exposure in dry air. A pre-treatment using H_2 pulses in dry air ambient at 250 °C was applied to extend the detection range of the sensor. The H_2 treated H_2S gas sensor was able to detect a higher H_2S concentration up to 90 ppm at 250 °C without complete saturation. High operating temperature above 150 °C enabled large signal variation (ΔI_{DS}) of 2.17 mA and sensing response of 112 % for 90 ppm H_2S in dry air as well as high stability across a wide range of biasing conditions. Transient response measurements demonstrated stable operation, superb response and recovery, with good repeatability. The measured sensing signal rise (fall) times reduced from 476 (1316) s to 219 (507) s when the temperature was increased from 200 °C to 250 °C. The response to 90 ppm H_2S was 4.5x larger than to H_2 and the device showed stable operation over an extended time period.

Parts of this chapter have been published in Sensors and Actuators B: Chemical, **274**, (2018) [1].

4.1. INTRODUCTION

With the continuous and rapid industrial growth, environmental pollution monitoring and assurance of worker safety raise increasing concerns. H_2S is a toxic, flammable, colorless gas with characteristic pungent odor [2]. It is naturally produced from sewage, liquid manure, sulfur hot springs and biogas [3]. H_2S is also a by-product of coal mining, petroleum and natural gas refinement industries [4]. Extended exposure to 10–500 ppm H_2S concentrations can cause symptoms varying from rhinitis to loss of consciousness and even respiratory failure. Furthermore, continuous inhalation of concentration above 100 ppm will cause inhibition of sensing the characteristic odor, due to olfactory fatigue [3, 5], which can result in false assumption of the gas being dissipated. Hence, portable, wearable and reliable detectors, capable of sensing low ppm levels of H_2S are of crucial importance to ensure worker safety for the fossil fuel and other energy production industries.

The first solid state gas sensor based on silicon metal oxide semiconductor (MOS) field effect transistor (FET), using palladium (Pd) as hydrogen (H_2) sensitive layer, was reported in 1975 [6]. Numerous modifications of the original transducer were further developed to enhance performance in terms of sensor sensitivity and expand the range of detectable gases. These devices include the suspended gate FET (SG-FET) [7], hybrid SG-FET [8], capacitively controlled FET (CCFET) [9], floating gate FET (FG-FET) [10] and most recently the horizontal FG-FET [11]. However, because of the narrow energy bandgap of Si (1.12 eV), these GasFETs are not able of operating at temperatures above 200 °C. In fact, initial reports on silicon Pd-MOS H_2S sensors have demonstrated operation at temperature up to 150 °C [12, 13]. To overcome the limitations related to the use of Si, wider bandgap 2^{nd} generation compound III-V semiconductors, including InP [14], GaAs [15, 16], InGaP [17], InAlAs [18], have been previously investigated for gas sensing applications. While these devices achieved improved sensing performance, the requirement of costly and fragile GaAs or InP substrates for layer epitaxy limits their large-scale adoption. 3^{rd} generation wide bandgap (>3 eV) silicon carbide (SiC) and gallium nitride (GaN) materials are favourable for development of high performance gas sensors. The price of SiC substrates is currently very high, while GaN can be grown on cost effective sapphire or Si wafers. Hence gallium nitride, with a bandgap of 3.4 eV is particularly advantageous for harsh environment, high temperature electronics and sensor applications [19]. AlGaN/GaN heterostructure Schottky diode and high electron mobility transistor (HEMT) based H_2 sensors have been demonstrated operating at 800 °C under N_2 ambient [20, 21]. While most studies refer to H_2 sensors [22–24], AlGaN/GaN sensors were also demonstrated for CO, CO_2, NO, NO_2, NH_3, Cl_2, CH_4, C_2H_2 [25–31].

Very few results of H_2S detection with wide bandgap semiconductor devices have been reported so far. A GaN Schottky diode with Pt gas sensing layer has been demonstrated for 0.1~10 ppm H_2S detection under N2 ambient [32]. A Silicon carbide FET with Pt and Ir gates was also shown to sense H_2S, however signal saturation was observed at low concentration of 6~8 ppm under 5% oxygen atmosphere [33, 34]. In this chapter, we present a comprehensive study of DC and transient characteristics at different temperatures and H_2S concentrations in dry air atmosphere. Moreover, the measured signal variations and sensing responses at different bias points are evaluated and sensor stability, selectivity and repeatability are demonstrated.

4.2. EXPERIMENTAL

4.2.1. FABRICATION OF SENSORS

The epitaxial structure used for device fabrication was purchased from a commercial vendor, Suzhou Nanowin Co. The material was grown by MOCVD on 2 inch c-plane sapphire wafers. Starting from the substrate, the stack consisted of a proprietary nucleation layer, for lattice mismatch compensation, a 1.8 µm GaN buffer, 1 nm AlN interlayer, followed by an undoped 21 nm $Al_{0.26}Ga_{0.74}N$ barrier and 1.5 nm GaN capping layer. The basis for HEMT operation is the formation of a high electron density channel, two-dimensional electron gas (2DEG), at the AlGaN/GaN heterojunction interface, due to polarization effect [35]. The sensor fabrication started with wet chemical cleaning of the substrate using acetone, isopropanol and DI water rinsing. Afterwards 100 nm deep mesa etching was performed by ICP BCl_3/Cl_2 plasma to isolate individual devices. Then ohmic contacts consisting of a Ti/Al/Ti/Au stack with thickness of 20/110/40/50 nm, were e-beam evaporated and patterned by lift-off. A 60 s dip in HCl:H_2O solution was done right before loading the wafers into the deposition chamber to remove any surface oxide [36]. After pattering, the contacts were annealed for 47 s at 870 °C in N_2 ambient. The gas sensing gate electrode was then formed by e-beam evaporation and lift-off of a 10 nm Pt layer. Then a bi-layer of 30/300 nm Ti/Au interconnect metal was evaporated and patterned by lift-off to guarantee reliable wire bonding. Finally, the devices were passivated by a 500 nm PECVD SiN_x layer followed by combined RIE and wet BOE etching to open the sensing area and the bonding pads. The schematic cross-section and top view optical micrograph of the fabricated device are shown in fig. 4.1. The gate dimensions exposed to gas were 40 µm × 400 µm and the gate-source and gate-drain spacing was 6 um, based on our earlier findings as discussed in chapter 3. After fabrication, the wafers were diced and individual devices were wire bonded to ceramic substrates for high temperature measurements.

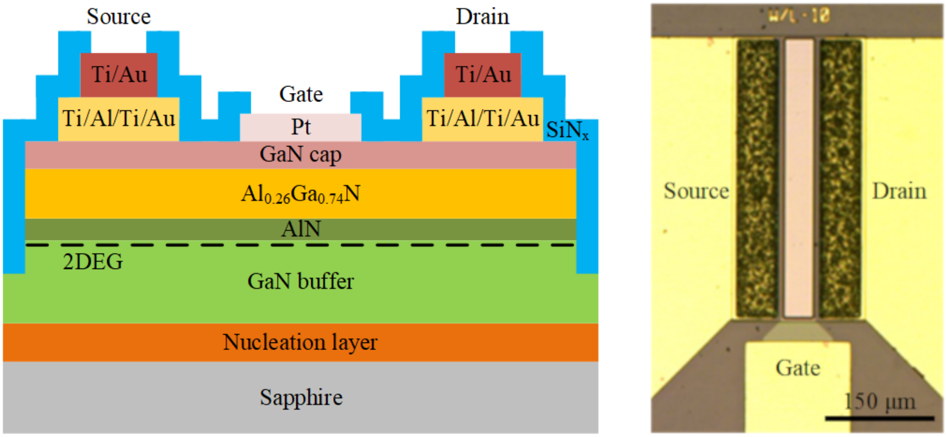

(a) (b)

Figure 4.1: Schematic cross-section of the studied Pt-AlGaN/GaN HEMT H_2S sensor (a). Top view optical micrograph of the fabricated sensor (b).

4.2.2. TESTING OF SENSORS

Gas testing was performed using a commercial gas mixing system from Beijing Elite Tech Co, which consists of mass flow controllers (MFC) to dilute the calibration gas, a 1.8 L volume chamber with temperature controlled hotplate, temperature and humidity sensors and electrical feedthroughs. The sensors were tested at different temperatures using H_2S reference gas diluted with dry synthetic air (O_2/N_2=21 %/79 %) to ensure close to 0 % relative humidity. The combined total gas flow was kept at 310 sccm. Electrical sensor measurements were conducted using a pair of Keithley 2450 source meters. Before gas sensing experiments the sensors underwent a burn-in procedure in dry air ambient for 24 hours at 150 °C with gate and drain bias voltages of 0 V and 5 V, respectively, in order to minimize baseline drift. Afterwards sensor activation was carried out with H_2 pulses of increasing concentration from 100 to 900 ppm with air purges in-between at 250 °C. We observed that such treatment allowed to extend the upper limit of H_2S detection before signal saturation occurred. Exposure to H_2 can reform the surface morphology of Pt [37] and increase the number of surface sites for gas adsorption. Further investigation into the mechanism of H_2 based pre-treatment are discussed section 4.4.

4.3. RESULTS AND DISCUSSION

The steady state sensing characteristics of the Pt-HEMT sensor were studied by measuring the drain current versus drain-source voltage ($I_{DS} - V_{DS}$) and the drain current versus gate-source voltage ($I_{DS} - V_{GS}$). Output ($I_{DS} - V_{DS}$) characteristics upon exposure to H_2S/Air concentrations of 15–90 ppm at temperatures of 150 °C, 200 °C and 250 °C are shown in figs. 4.2a–4.2c. The gate-source voltage (V_{GS}) was stepped from −3 V to 1 V

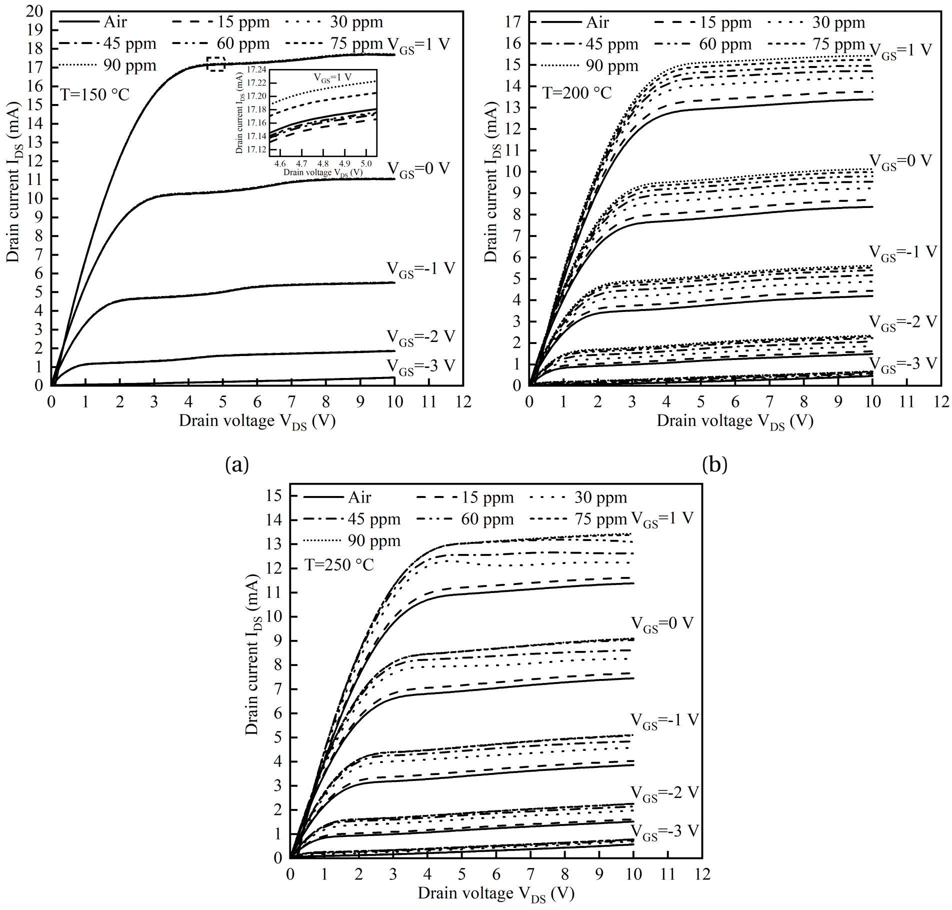

(a) (b)

(c)

Figure 4.2: Output ($I_{DS} - V_{DS}$) characteristics of Pt-HEMT sensors exposed to different H_2S concentrations at (a) 150 °C, with the inset showing a magnified view of the box area, (b) 200 °C and (c) 250 °C.

with 1 V increments. Proper transistor operation is clearly observed with distinct linear and saturation regions and the ability to modulate output current via the gate terminal is maintained at all tested temperatures. A profound rise in drain current was observed at 200 °C and 250 °C with increasing H_2S concentrations. At 250 °C the sensing signal started to saturate at concentrations above 60 ppm/air. The magnitude of current variation at 150 °C was much lower, with noticeable instability below 75 ppm/air. The corresponding transfer ($I_{DS} - V_{GS}$) and transconductance (g_m) characteristics at V_{DS}=7 V

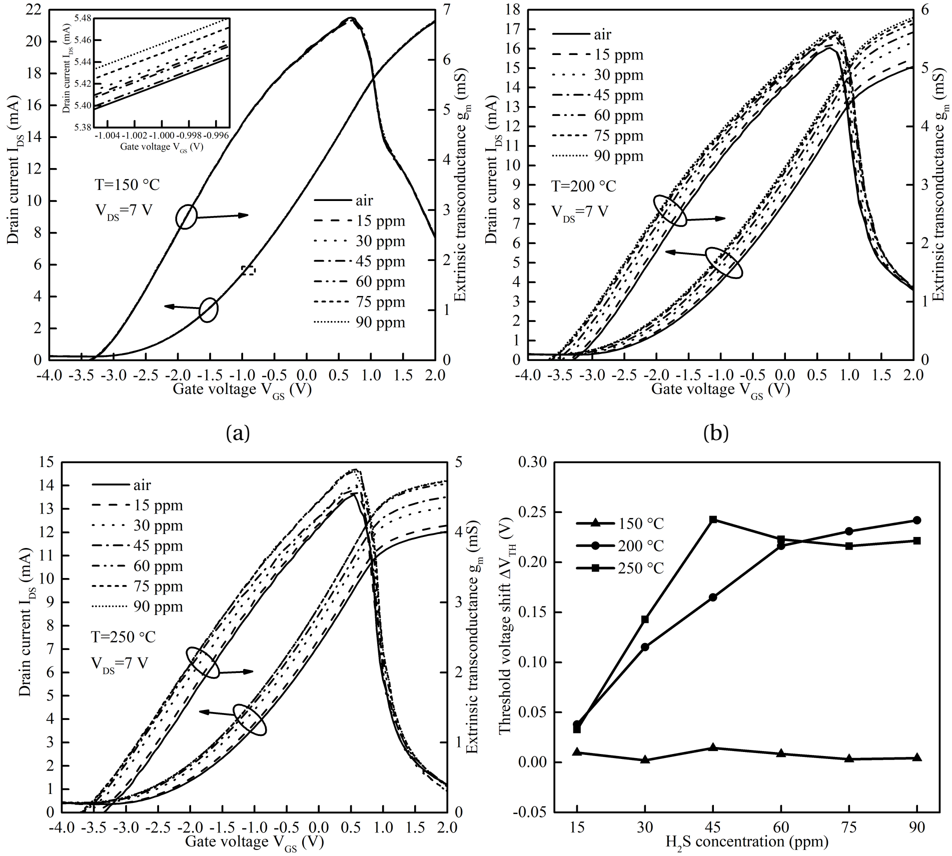

(a)

(b)

(c)

(d)

Figure 4.3: Transfer ($I_{DS}-V_{GS}$) and transconductance characteristics of Pt-HEMT sensors exposed to different H_2S concentrations at (a) 150 °C, with the inset showing a magnified view of the box area, (b) 200 °C and (c) 250 °C. (d) Threshold voltage shift versus H_2S concentration.

are shown in figs. 4.3a–4.3c. Upon exposure to H_2S the curves shift towards more negative voltages for the same I_{DS} levels. The maximum transconductance ($g_{m,max}$) values increased from 6.82, 5.35, 4.54 mS in air ambient to 6.83, 5.63, 4.89 mS when exposed to 90 ppm/air at temperatures of 150 °C, 200 °C and 250 °C, respectively. Higher transconductance in H_2S containing ambient is attributed to increased number of electrons in the 2DEG channel due to gas interaction with the Pt gate which is also evident from fig. 4.2. Threshold voltage (V_{TH}) values at tested concentrations were extracted from figs. 4.3a–4.3c using the linear extrapolation method by fitting a tangent line at the point of $g_{m,max}$ to the V_{GS} axis intercept [38]. The threshold voltage shift, defined as $\Delta V_{TH} = V_{TH,air} - V_{TH,\mathrm{H_2S}}$, for the tested H_2S concentration range is shown in fig. 4.3d.

Clearly the magnitude of ΔV_{TH} increases with increasing test gas concentration at 200 °C and 250 °C. At 150 °C ΔV_{TH} mostly unchanged, due to low catalytic dissociation efficiency of H_2S on Pt at this temperature. Output and transfer characteristics before and after exposure to 90 ppm H_2S/Air are shown in fig. 4.4a and fig. 4.4b, respectively. After the initial baseline measurements in dry air at 250 °C, H_2S was injected into the test chamber for 20 min followed by an air purge for 60 min. From fig. 4.4a an increase of 0.26 mA was observed for the baseline current (at V_{GS}=0 V, V_{DS}=5 V) and a corresponding −0.06 V shift (fig. 4.4b) of the transfer curve (at I_{DS}=5 mA). It was observed that after the sensor was exposed to ambient conditions for several hours the baseline values were restored. To understand the current and threshold voltage variations and analyse the gas sensing mechanism we first look at the saturation drain current of an AlGaN/GaN HEMT expressed as:

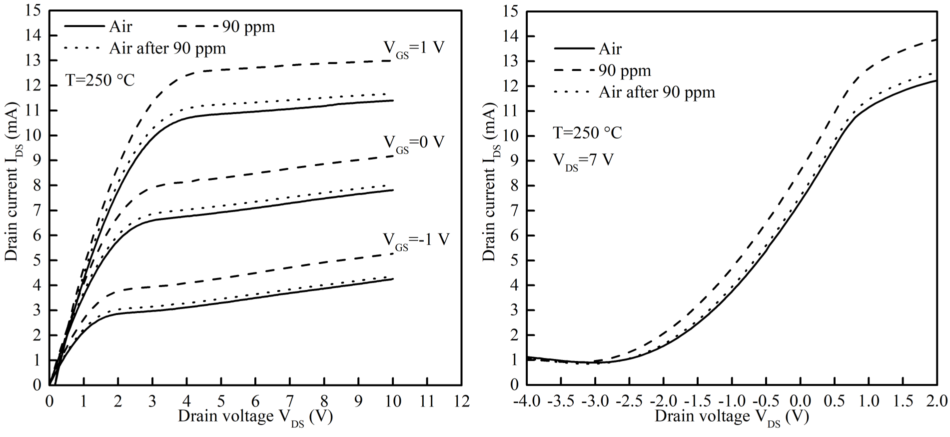

(a) (b)

Figure 4.4: (a) Output ($I_{DS}-V_{DS}$) and (b) transfer ($I_{DS}-V_{GS}$) characteristics of the Pt-HEMT sensor before and after exposure to 90 ppm of H_2S at 250 °C.

$$I_{DS,sat} = \frac{\mu C_b W_g}{2L_g}(V_{GS}-V_{TH})^2 \tag{4.1}$$

where μ is the 2DEG mobility, W_g/L_g the gate width/length, C_b is gate to channel capacitance, which is the sum of capacitance contributions from each layer between the gate metal and 2DEG $1/C_b = (1/C_{cap} + 1/C_{AlGaN} + 1/C_{AlN} + 1/C_{2DEG})$. The μ and C_b are determined by the quality and structure of the epitaxy, while W_g/L_g are defined by sensor design. The shift in threshold voltage towards more negative value would result in the observed I_{DS} increase in H_2S containing atmosphere. The expression of V_{TH} for an

AlGaN/GaN HEMT is:

$$V_{TH} = \Phi_b - \frac{\Delta E_C}{q} - \frac{q n_s}{C_b} \tag{4.2}$$

where Φ_b is the Schottky barrier height, ΔE_C is the conduction band discontinuity, q is the elementary charge and n_s is the sheet charge carrier density. The Schottky barrier height is in turn dependent on the work function (Φ_m) of the gate metal and the semiconductor electron affinity (χ_s), $\Phi_b = \Phi_m - \chi_s$. Previous research has found that hydrogen containing gas molecules upon adsorption on the surface of catalytic metals (e.g. Pt, Pd or Ir) dissociate and release hydrogen atoms [22, 28, 30]. In the case of H_2S adsorption in air ambient the probable reaction mechanism is as follows [39]:

$$H_2S_{(ad)} \longrightarrow SH_{(ad)} + H_{(ad)} \tag{4.3}$$

$$HS_{(ad)} \longrightarrow S_{(ad)} + H_{(ad)} \tag{4.4}$$

$$S_{(ad)} + O_{2(ad)} \longrightarrow SO_{2(gas)} \tag{4.5}$$

The S–H bonds are broken sequentially as described by eq. (4.3) and eq. (4.4) and the remaining sulfur reacts with O_2 present at the Pt surface and forms SO_2 which can then desorb from the surface. The hydrogen ions rapidly diffuse through the Pt to the M–S interface. It is assumed that there is an interfacial oxide layer present on the GaN surface, since it was exposed to ambient conditions during sensor fabrication for several hours and no chemical or plasma treatments were performed prior to Pt deposition. The oxide layer supplies bonding sites for the diffused H resulting in a dipole layer at the interface [40]. This causes the reduction of metal work function (Φ_m) and the lowering of the (Φ_b), which results in the observed ΔV_{TH} and I_{DS} increase in H_2S containing atmosphere. To evaluate the hydrogen sulfide detection performance of our Pt-HEMT sensor, we calculated the sensing response defined as:

$$S(\%) = \frac{\Delta I_{DS}}{I_{DS,air}} \times 100\% \tag{4.6}$$

where $\Delta I_{DS} = I_{DS,\mathrm{H_2S}} - I_{DS,air}$ is the drain current variation between H_2S containing and pure air ambient. Figure 4.5a shows the ΔI_{DS} as a function of drain-source voltage (V_{DS}) for V_{GS}=0 V at temperature of 200 °C. Measurements indicated that the ΔI_{DS} increases linearly with V_{DS} in the transistor linear region until it reaches the maximum value at the transition point to the saturation region at approximately 4 V, and then reduces by only 4 % at V_{DS}=10 V. This demonstrates that our sensor exhibits high stability and allows for a wide selection of biasing conditions without diminishing sensing performance. The

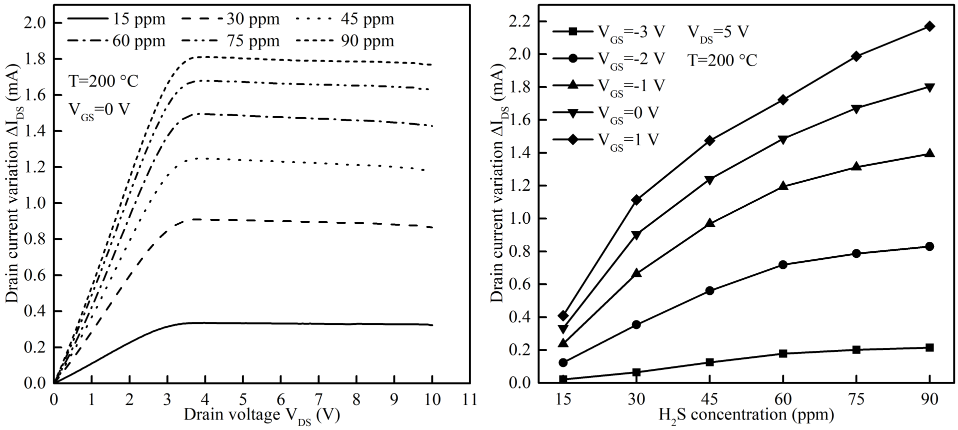

(a) (b)

Figure 4.5: (a) Drain current variation (ΔI_{DS}) as a function of drain-source (V_{DS}) voltage for different H_2S concentrations at 200 °C, V_{GS}=0 V. (b) Drain current variation (ΔI_{DS}) versus H_2S concentration at 200 °C, V_{DS}=5 V.

drain current variation at different H_2S concentrations and gate bias voltages is shown in fig. 4.5b. The magnitude of sensing signal variation is greatly impacted by the gate bias. For 90 ppm H_2S concentration the measured ΔI_{DS} increased tenfold, from 0.21 mA at V_{GS}=−3 V to 2.17 mA at V_{GS}=1 V. The ΔI_{DS} increase is due to larger baseline current ($I_{DS,air}$) with increasing gate bias. Figure 4.6a shows the hydrogen sulfide sensing re-

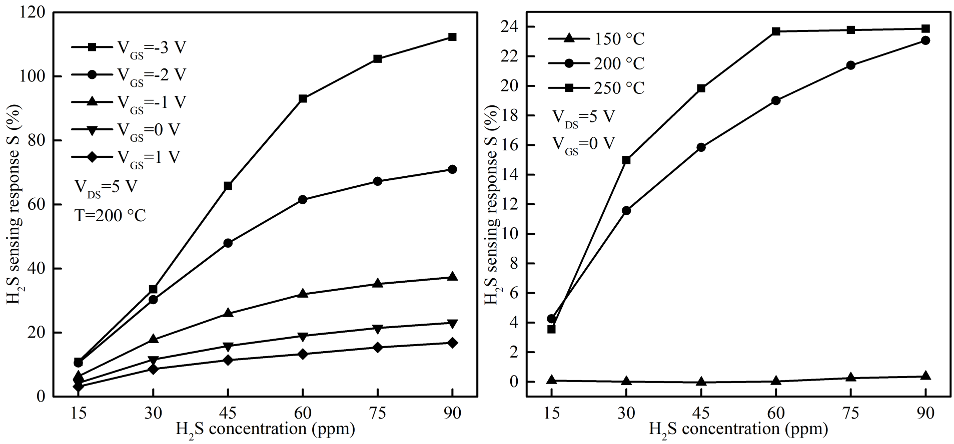

(a) (b)

Figure 4.6: Hydrogen sulfide sensor sensing response at (a) various gate bias voltages and (b) at different temperatures.

sponse at different gate bias voltages, while fig. 4.6b shows response at different temperatures. Looking at eq. (4.6) the reduction of S is due to larger increase of $I_{DS,air}$ with higher V_{GS} than the increase in ΔI_{DS}. Based on fig. 4.5b we conclude that HEMT type sensor can be operated at high signal amplitude (ΔI_{DS}) conditions (V_{GS}>0 V) to achieve the lowest gas detection limits. Alternatively, as shown in fig. 4.6a, operating in high response mode is possible when gate bias is approaching pinch-off state thereby minimizing sensor power consumption. GaN Schottky diode type H_2 sensor had been previously demonstrated with very high response of ~3500% at 150 °C, however the signal amplitude was on the order of nA [41]. From fig. 4.6b it is evident that response towards H_2S increased with higher temperature, however saturation started to occur earlier, namely above 60 ppm concentration.

Figure 4.7 shows transient characteristics of the Pt-HEMT sensors at the tested temperatures and increasing analyte gas concentrations. The bias conditions used were V_{DS}=5 V, V_{GS}=0 V to obtain high ΔI_{DS} and operate the sensor as 2-terminal device with gate and source terminals shorted. The drain current increased immediately upon in-

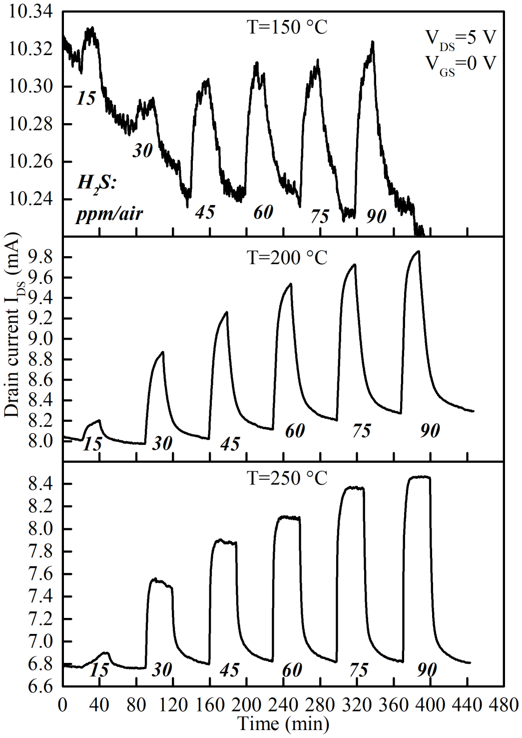

Figure 4.7: Transient response characteristics upon injection and purge of H_2S in dry air ambient at 150 °C, 200 °C and 250 °C (from top to bottom). During all measurements V_{DS}=5 V, V_{GS}=0 V.

jecting H_2S, with the operating temperature having a significant impact on the observed response. At 150 °C there is substantial baseline value drift at 15 ppm and 30 ppm, followed by minimal signal variation with increasing concentration. It is believed to be caused by sulfur poisoning of the Pt surface due to incomplete oxidation to SO_2 and desorption at this temperature [13]. Raising the temperature to 200 °C resulted in an increased signal and improved recovery of the sensor, while at 250 °C the sensor rapidly reached steady state after gas introduction and returned to the baseline level during air purge steps. Moreover signal saturation was less profound compared with DC measurements. The increased magnitude of response current at 200 °C and 250 °C is due to enhanced reaction rate of H–S bond cleavage and H atom diffusion through the Pt gate. The baseline current value in air ambient reduces with rising temperature due to reduction of electron mobility in 2DEG channel.

Response and recovery rates were estimated using rise (t_R) and fall (t_F) times, defined as the time required for the signal to rise/fall from 10 % to 90 % of the steady state values. This method was used to reduce the influence of the delay necessary to equilibrate gas concentration inside the testing chamber. Figure 4.8a and fig. 4.8b show the t_R and t_F as a function of H_2S concentration at tested temperatures. The transient times

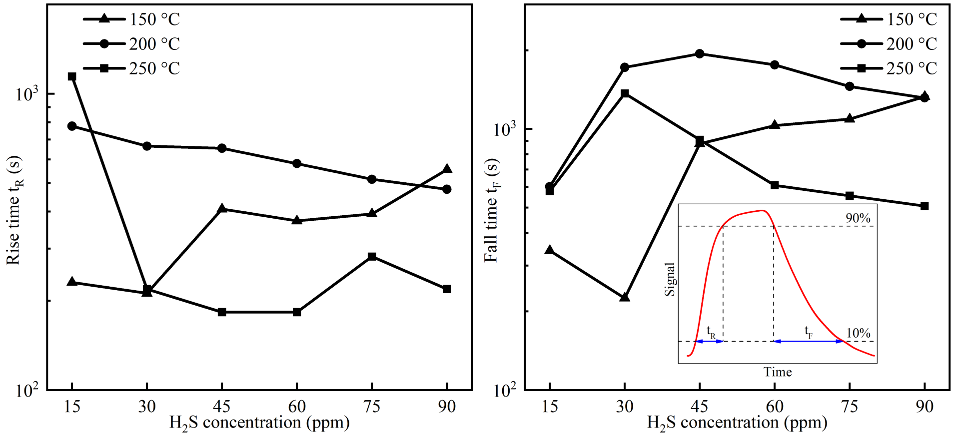

(a)

(b)

Figure 4.8: (a) Rise time (t_R) and (b) fall time (t_F) versus H_2S concentration at 150 °C, 200 °C and 250 °C. The inset schematically shows the definition of t_R and t_F.

decreased with increasing gas concentration for 200 °C and 250 °C. The results at 150 °C were irregular due to low signal variation and baseline current value drift at 15 ppm and 30 ppm gas concentrations which resulted in quicker t_R and t_F. Starting with 45 ppm the baseline stabilized and the response (recovery) times became more consistent. At

90 ppm H_2S concentration t_R (t_F) reduced from 476 (1316) s at 200 °C to 219 (507) s at 250 °C. The shorter rise/fall times are attributed to faster gas adsorption and desorption kinetics at the Pt surface and M–S interface with increasing temperature. Further decrease of t_R and t_F is expected with downsizing the volume of the testing chamber. Figure 4.9 shows 5 consecutive exposure and purge cycles of 90 ppm H_2S. Obviously the sensor demonstrated repeatable and reversible current variation characteristics under continuous operation at 250 °C.

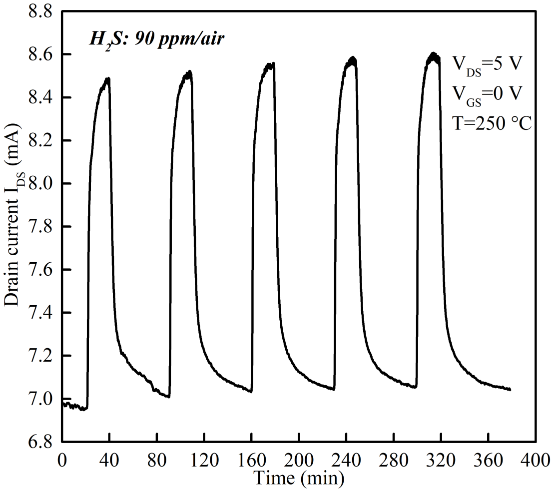

Figure 4.9: Five repetitive cycles of sensor exposure to 90 ppm of H_2S at 250 °C.

Pd and Pt gate field effect devices are known to detect H_2 gas, therefore a comparison of response between H_2S and H_2 was carried out. Figure 4.10a shows the transient drain current curves of the tested sensor exposed to 60 ppm and 90 ppm of H_2S, H_2 and NO_2 at 250 °C. The sensing response to 90 ppm for each gas is summarized in fig. 4.10b. It is evident that the response to H_2S was 4.5x higher than to H_2, while the response to NO_2 was negligible and I_{DS} decreased upon gas exposure.

Long-term operation stability of the Pt-HEMT sensor was tested by performing the H_2S tests over a period of 15 days. Figure 4.11 shows the daily drain current variation (ΔI_{DS}) for 60 ppm and 90 ppm H_2S at 250 °C. There was no significant deterioration of the sensing signal during the testing period. We did observe however that the Au-plated pads of our ceramic testing substrates and bond-pads of the HEMT chip were corroded after extended exposure to H_2S, therefore packaging reliability needs to be further investigated to ensure stable sensor operation.

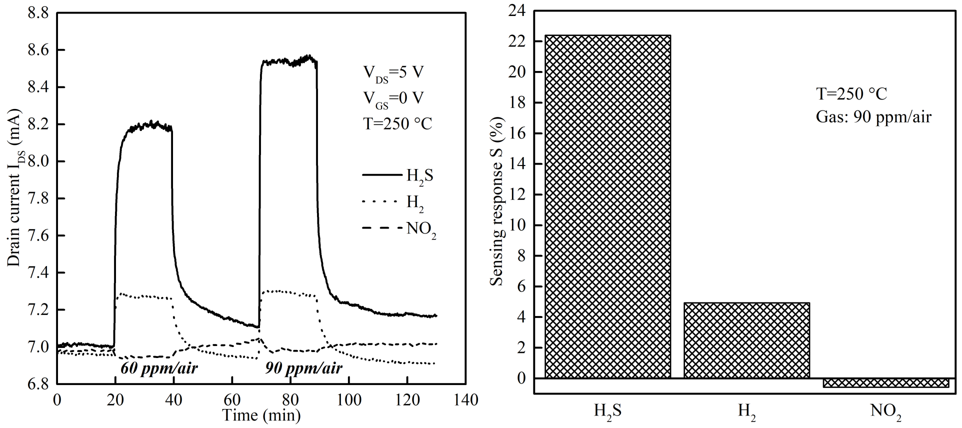

(a) (b)

Figure 4.10: (a) Transient response characteristics upon exposure to 60 ppm and 90 ppm of H_2S, H_2 and NO_2 at 250 °C in dry air ambient. (b) Sensing response to 90 ppm of H_2S, H_2 and NO_2.

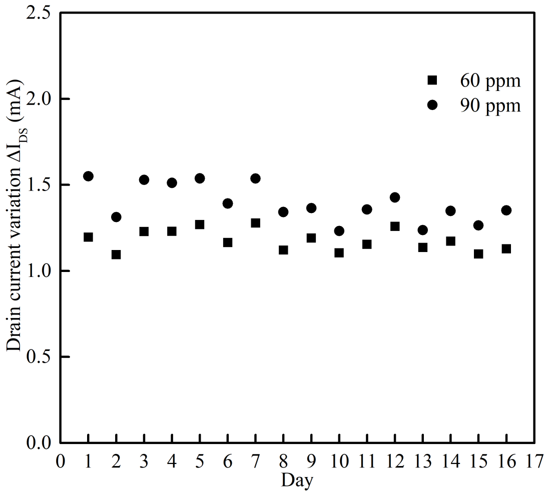

Figure 4.11: Sensor drain current variation (ΔI_{DS}) characteristics towards 60 ppm and 90 ppm of H_2S over 15 day testing period at 250 °C.

4.4. EFFECTS OF SENSOR PRE-TREATMENT WITH H_2

During sensor characterization it was observed that fresh devices exposed to H_2S exhibited higher signal variation (ΔI_{DS}) at low concentrations. Figure 4.12a shows the transient response curves (V_{GS}=0 V, V_{DS}=5 V) for different H_2S concentrations at 250 °C using a fresh sensor without H_2 pre-treatment. Clearly, I_{DS} has saturated at a low concentration of 30 ppm. Similar saturating response was observed in the case of SiC-FET-based

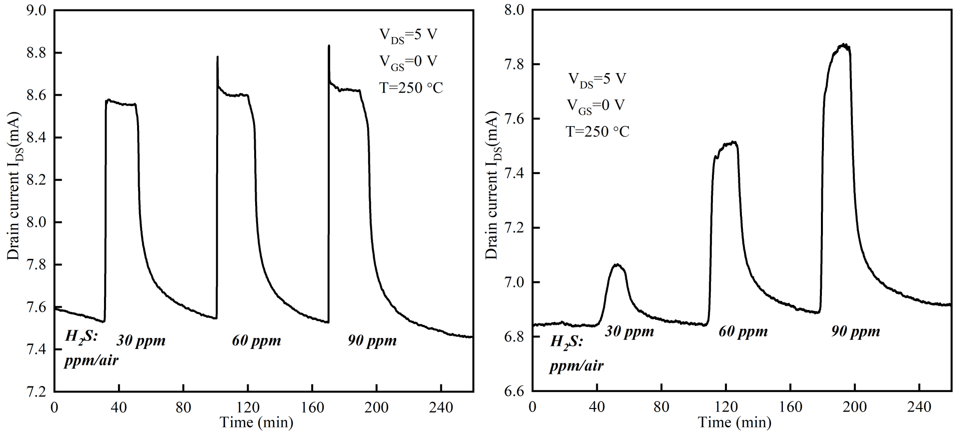

(a) (b)

Figure 4.12: Transient response curves for H_2S at 250 °C without H_2 pre-treatment (a). The transient response curves for H_2S at 250 °C with H2 pre-treatment (b).

H_2S sensors [33]. The H_2 pre-treatment process involved exposing the samples to alternating gas flows of dry air (50 min) and H_2 (20 min) for 6 h at 250 °C. The concentration of H_2 was increased with each exposure from 100 ppm to 900 ppm with 300 ppm increment. After each measurement cycle, the sensors were reset under room ambient conditions for at least 12 h. Figure 4.12b shows the transient response curves for the H_2 pre-treated sensors at 250 °C. The different H_2S concentrations are clearly distinguished. H_2S sensing response for sensors with and without H_2 pre-treatment is shown fig. 4.13. Before

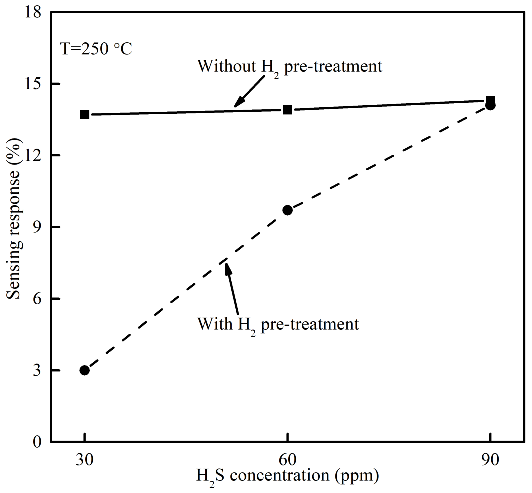

Figure 4.13: H_2S responses for sensors with and without H_2 pre-treatment measured at 250 °C.

treatment, the gas response is nearly unchanged for different H_2S concentrations, while after H_2 pre-treatment it is almost linear. The large S difference indicates that the H_2 pre-treatment can effectively extend the sensor detection range.

Prior to sensing H_2S, the influence of H_2 pre-treatment on sensor static characteristics in dry air ambient were studied as shown in fig. 4.14. After H_2 treatment drain current obviously decreased and threshold voltage (V_{TH}) shifted towards positive direction as shown in fig. 4.14a. According to eq. (4.2) a V_{TH} shift to higher values is likely due to increase of the Schottky barrier height (Φ_b), which in turn depends on the work function (Φ_m) of the Pt gate.

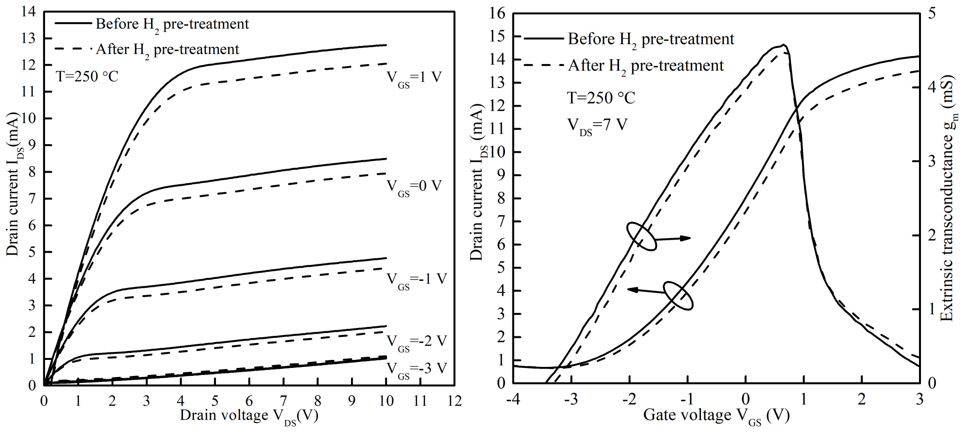

(a) (b)

Figure 4.14: (a) Output ($I_{DS} - V_{DS}$) and (b) transfer ($I_{DS} - V_{GS}$) characteristics of the Pt-HEMT sensor before and after H_2 pre-treatment at 250 °C in dry air.

In order to gain understanding of the observed I_{DS} reduction and V_{TH} shift after H_2 pre-treatment we have examined previously reported observations on catalytic metal interaction with H_2. Evidently H_2 exposure leads to:

- the formation of hydrogen induced interface dipole layer [22]
- the existence of slow H trapping sites, leading to hydrogen induced drift (HID) [42]
- Metal blistering due to H absorption induced stress [43]
- Morphological changes of Pt surface after exposure to H_2 [37]

Hydrogen dissociation on Pt surface followed by diffusion to the metal-semiconductor interface, which results in the dipole layer, is a reversible process of lowering Φ_b. HID manifests itself as a slow recovery of the sensor to baseline value after hydrogen exposure. It occurs due to protons penetrating into surface layers of SiO_2. HID cannot explain the observations after H_2 pre-treatment as it also results in lower Φ_b and is attributed to sodium contamination of SiO_2 [42]. Surface inspection of the gate area with opitcal microscopy before and after H_2 exposure did not reveal any metal blistering. Atomic force microscopy (AFM) was utilized to analyse the Pt gate surface morphology. The results also clearly indicate little change of Pt film morphology as shown in fig. 4.15.

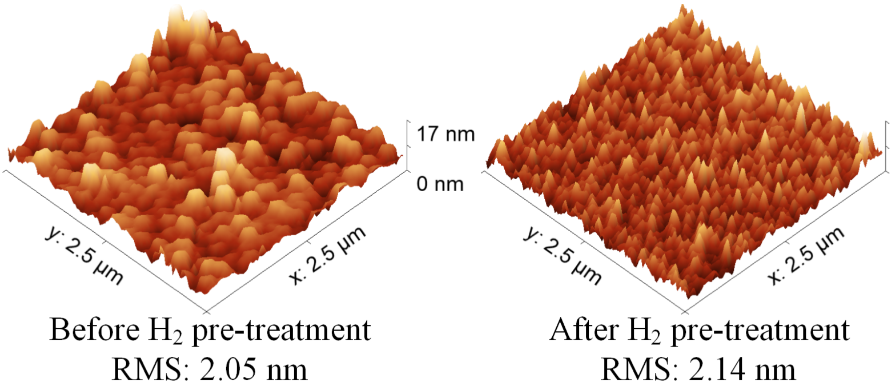

(a) (b)

Figure 4.15: AFM scan of Pt film surface (a) without and (b) with H_2 pre-treatment at 250 °C.

An alternative mechanism is proposed in order to explain the effects of H_2 treatment. Figures 4.16a and 4.16b show the presence of H in the Pt gate for sensors with and without H_2 pre-treatment. Some hydrogen atoms diffusing through Pt will get trapped within defect sites in the Pt grain boundaries, releasing an electron and becoming fixed positive H^+ ions. As a result induced negative charges will accumulate on the Pt film surface as

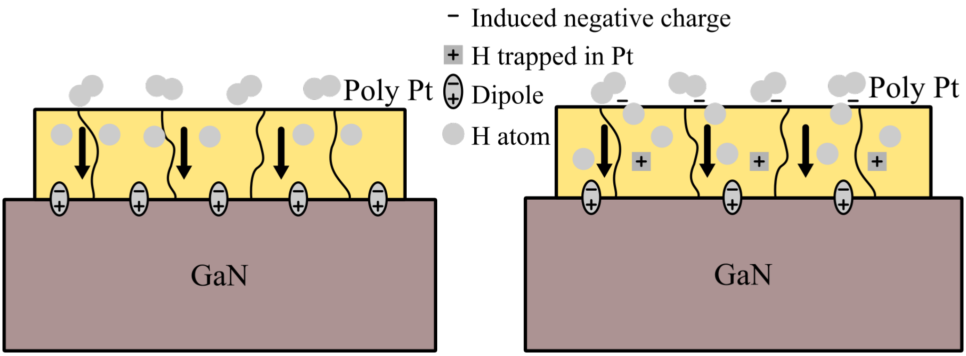

(a) (b)

Figure 4.16: Schematic diagram of H presence in the Pt film (a) before and (b) after H_2 pre-treatment.

shown in fig. 4.16b. The negative charge will increase the work function of the Pt film, resulting in the positive V_{TH} shift and I_{DS} reduction. Since these H^+ ions within Pt grains are fixed, the induced negative charges on Pt film surface are also stable. Another probable location for H trapping is Pt surface defects [44], such as surface clusters, steps and grain boundaries. Once absorbed, H atoms will show positive polarity due to a weaker electronegativity compared to Pt. Thus, a dipole layer can form around the Pt film surface and grain boundaries. These dipole layers will equivalently lower the Pt film work function, which will reduce the V_{TH}. However, these absorbed H atoms can desorb from the surface out into the atmosphere when the H_2 concentration is lowered. Since there are fixed H^+ ions within the Pt grains after H_2 pretreatment, the induced negative charges on the Pt film surface are present. The adsorbed H atoms on the Pt top surface will be attracted by these induced negative charges. Consequently, on the Pt top surface the diffusion of the adsorbed H atoms through the Pt film towards the interface of Pt/GaN will be partly suppressed. Furthermore, the positive trapped H^+ inside the metal may repel the atoms from the M-S interface (see fig. 4.16b). Hence under same H_2S concentration the amount of hydrogen atoms which can diffuse into the interface of Pt/GaN will decrease after pre-treatment. Reduction of interface dipole coverage thereby enables extending the sensor detection range as evident from fig. 4.13.

The transient response of the fresh HEMT sensor during H_2 pre-treatment process is shown in fig. 4.16. Only after exposure to 900 ppm H_2, the baseline value I_{DS} in dry air noticeably reduced. Apparently the H^+ ions activate within the Pt grains at a certain

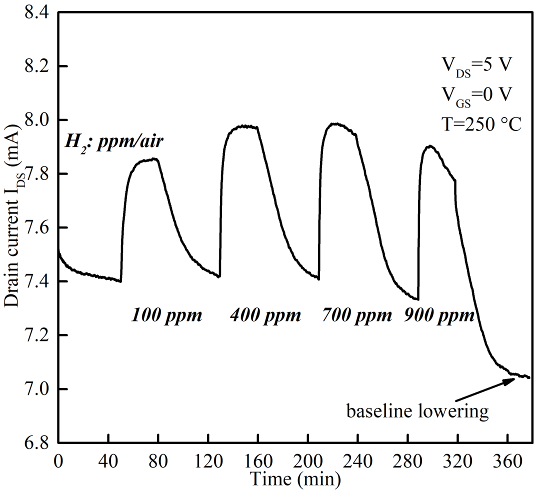

Figure 4.17: The transient response curve of H_2 pre-treatment process at 250 °C.

H_2 concentration and high temperature. Once these H^+ ions form they become stable charges than do not desorb like H atoms at the surface or interface. It also implies the H^+ ion formation process is negligible when the H_2 concentration is less than few 100 ppm.

4.5. CONCLUSIONS

Sensors based on AlGaN/GaN HEMTs with Pt catalytic gate were fabricated and characterized for detecting ppm levels of hydrogen sulfide at high temperature. The developed devices exhibited a significant drain current increase and threshold voltage shift upon exposure to the test gas. At 200 °C maximum ΔI_{DS} of 2.17 mA ($V_{GS} = 1$ V) as well as high sensing response of 112 % (V_{GS}=−3 V) for 90 ppm H_2S was obtained. High stability was observed with only 4 % reduction of ΔI_{DS} across the tested drain saturation voltage range, which enables a wide selection of biasing conditions. At 150 °C very low response and baseline drift were likely caused by sulfur poisoning effect of the Pt gate. Transient measurements confirmed stable operation with excellent response, recovery and repeatability properties. The rise (fall) times reduced from 476 (1316) s to 219 (507) s when the temperature was elevated from 200 °C to 250 °C. Sensing response of H_2S was 4.5x greater than H_2 for 90 ppm concentration. The operating stability was validated over 15 days with no significant reduction of sensing signal. However, the as-fabricated sensors exhibited saturation for low H_2S concentrations. A high temperature H_2 pre-treatment was proposed and successfully applied to extend the detection range. The mechanism is believed to be correlated with the interaction between Pt film and H_2, which may introduce stable H^+ ions within Pt grains and result in the positive V_{TH} shift. The negative charges induced by these H^+ ions at the Pt top surface will attract the adsorbed H atoms with positive polarity and the trapped ions in the bulk will repel them, hence the number of atoms diffusing to the M-S interface will reduce. Our findings firmly suggest that AlGaN/GaN HEMT sensors are a promising technology for industrial wearable worker safety detectors.

REFERENCES

[1] R. Sokolovskij, J. Zhang, E. Iervolino, C. Zhao, F. Santagata, F. Wang, H. Yu, P. M. Sarro, and G. Q. Zhang, *Hydrogen sulfide detection properties of Pt-gated AlGaN/GaN HEMT-sensor,* Sensors and Actuators B: Chemical **274**, 636 (2018).

[2] H.-M. Huang, H.-Y. Li, X.-X. Wang, and X. Guo, *Detecting low concentration of H_2S gas by $BaTiO_3$ nanoparticle-based sensors,* Sensors and Actuators B: Chemical **238**, 16 (2017).

[3] E.-C. Lee, J. Kwan, J.-H. Leem, S.-G. Park, H.-C. Kim, D.-H. Lee, J.-H. Kim, and D.-H. Kim, *Hydrogen Sulfide Intoxication with Dilated Cardiomyopathy,* Journal of Occupational Health **51**, 522 (2009).

[4] F. Zhang, A. Zhu, Y. Luo, Y. Tian, J. Yang, and Y. Qin, *CuO Nanosheets for Sensitive and Selective Determination of* H_2S *with High Recovery Ability,* The Journal of Physical Chemistry C **114**, 19214 (2010).

[5] B. Doujaiji and J. A. Al-Tawfiq, *Hydrogen sulfide exposure in an adult male,* Annals of Saudi Medicine **30**, 76 (2010).

[6] K. I. Lundström, M. S. Shivaraman, and C. M. Svensson, *A hydrogen-sensitive Pd-gate MOS transistor,* Journal of Applied Physics **46**, 3876 (1975), https://doi.org/10.1063/1.322185 .

[7] H. Lorenz, M. Peschke, H. Riess, J. Janata, and I. Eisele, *New suspended gate FET technology for physical deposition of chemically sensitive layers,* Sensors and Actuators A: Physical **23**, 1023 (1990).

[8] I. Eisele, T. Doll, and M. Burgmair, *Low power gas detection with FET sensors,* Sensors and Actuators B: Chemical **78**, 19 (2001).

[9] Z. Gergintschew, P. Kornetzky, and D. Schipanski, *The capacitively controlled field effect transistor (CCFET) as a new low power gas sensor,* Sensors and Actuators B: Chemical **36**, 285 (1996).

[10] M. Burgmair, H.-P. Frerichs, M. Zimmer, M. Lehmann, and I. Eisele, *Field effect transducers for work function gas measurements: device improvements and comparison of performance,* Sensors and Actuators B: Chemical **95**, 183 (2003).

[11] C. Kim, I. Cho, J. Shin, K. Choi, J. Lee, and J. Lee, *A New Gas Sensor Based on MOSFET Having a Horizontal Floating-Gate,* IEEE Electron Device Letters **35**, 265 (2014).

[12] M. S. Shivaraman, *Detection of* H_2S *with Pd-gate MOS field-effect transistors,* Journal of Applied Physics **47**, 3592 (1976).

[13] Z. Weixin and Z. Yibing, *The temperature characteristics of an* H_2S*-sensitive Pd-gate MOS transistor,* Sensors and Actuators **15**, 85 (1988).

[14] Wen-Chau Liu, Hsi-Jen Pan, Huey-Ing Chen, Kun-Wei Lin, Shiou-Ying Cheng, and Kuo-Hui Yu, *Hydrogen-sensitive characteristics of a novel Pd/InP MOS Schottky diode hydrogen sensor,* IEEE Transactions on Electron Devices **48**, 1938 (2001).

[15] M. Jaegle and K. Steiner, *Gas-sensitive GaAs-MESFETs,* Sensors and Actuators B: Chemical **34**, 543 (1996).

[16] C.-W. Hung, K.-W. Lin, R.-C. Liu, Y.-Y. Tsai, P.-H. Lai, S.-I. Fu, T.-P. Chen, H.-I. Chen, and W.-C. Liu, *On the hydrogen sensing properties of a Pd/GaAs transistor-type gas sensor in a nitrogen ambiance,* Sensors and Actuators B: Chemical **125**, 22 (2007).

[17] C.-C. Cheng, Y.-Y. Tsai, K.-W. Lin, H.-I. Chen, W.-H. Hsu, C.-W. Hong, and W.-C. Liu, *Characteristics of a Pd–oxide–*$In_{0.49}Ga_{0.51}P$ *high electron mobility transistor (HEMT)-based hydrogen sensor,* Sensors and Actuators B: Chemical **113**, 29 (2006).

[18] T.-H. Tsai, H.-I. Chen, K.-W. Lin, Y.-W. Kuo, P.-S. Chiu, C.-F. Chang, L.-Y. Chen, T.-P. Chen, Y.-J. Liu, and W.-C. Liu, *On a Pd/InAlAs metamorphic high electron mobility transistor (MHEMT)-based hydrogen sensor,* Sensors and Actuators B: Chemical **139**, 310 (2009).

[19] A. J. Suria, A. S. Yalamarthy, H. So, and D. G. Senesky, *DC characteristics of ALD-grown* Al_2O_3*/AlGaN/GaN MIS-HEMTs and HEMTs at* 600 °C *in air,* Semiconductor Science and Technology **31**, 115017 (2016).

[20] J. Song, W. Lu, J. S. Flynn, and G. R. Brandes, *Pt-AlGaN/GaN Schottky diodes operated at* 800 °C *for hydrogen sensing,* Applied Physics Letters **87**, 133501 (2005).

[21] J. Song and W. Lu, *Operation of Pt/AlGaN/GaN-Heterojunction Field-Effect-Transistor Hydrogen Sensors With Low Detection Limit and High Sensitivity,* IEEE Electron Device Letters **29**, 1193 (2008).

[22] C. Hsu, H. Chen, P. Chou, J. Liou, C. Chen, C. Chang, and W. Liu, *Hydrogen-Sensing Properties of a Pd/AlGaN/GaN-Based Field-Effect Transistor Under a Nitrogen Ambience,* IEEE Sensors Journal **13**, 1787 (2013).

[23] H.-I. Chen, K.-C. Chuang, C.-H. Chang, W.-C. Chen, I.-P. Liu, and W.-C. Liu, *Hydrogen sensing characteristics of a Pd/AlGaOx/AlGaN-based Schottky diode,* Sensors and Actuators B: Chemical **246**, 408 (2017).

[24] Y. Xi, L. Liu, Y.-H. Hwang, O. Phillips, F. Ren, S. J. Pearton, J. Kim, C.-H. Hsu, C.-F. Lo, and J. Wayne Johnson, *Study of hydrogen detection response time with Pt-gated diodes fabricated on AlGaN/GaN heterostructure,* Journal of Vacuum Science & Technology B **31**, 032202 (2013).

[25] C.-F. Lo, Y. Xi, L. Liu, S. J. Pearton, S. Doré, C.-H. Hsu, A. M. Dabiran, P. P. Chow, and F. Ren, *Effect of temperature on CO sensing response in air ambient by using ZnO nanorod-gated AlGaN/GaN high electron mobility transistors,* Sensors and Actuators B: Chemical **176**, 708 (2013).

[26] C. Y. Chang, B. S. Kang, H. T. Wang, F. Ren, Y. L. Wang, S. J. Pearton, D. M. Dennis, J. W. Johnson, P. Rajagopal, J. C. Roberts, E. L. Piner, and K. J. Linthicum, *CO_2 detection using polyethylenimine/starch functionalized AlGaN/GaN high electron mobility transistors,* Applied Physics Letters **92**, 232102 (2008).

[27] Y. Halfaya, C. Bishop, A. Soltani, S. Sundaram, V. Aubry, P. Voss, J.-P. Salvestrini, and A. Ougazzaden, *Investigation of the Performance of HEMT-based NO, NO_2 and NH_3 Exhaust Gas Sensors for Automotive Antipollution Systems,* Sensors **16**, 273 (2016).

[28] T. Chen, H. Chen, C. Hsu, C. Huang, C. Chang, P. Chou, and W. Liu, *On an Ammonia Gas Sensor Based on a Pt/AlGaN Heterostructure Field-Effect Transistor,* IEEE Electron Device Letters **33**, 612 (2012).

[29] K. Son, B. Yang, N. Prokopuk, J. S. Moon, A. Liao, T. M. Katona, and M. A. Khan, *RF GaN HEMT Sensors for Detection of Caustic Chemicals,* IEEE Sensors Journal **11**, 3476 (2011).

[30] Y. Xi, L. Liu, F. Ren, S. J. Pearton, J. Kim, A. Dabiran, and P. P. Chow, *Methane detection using Pt-gated AlGaN/GaN high electron mobility transistor based Schottky diodes,* Journal of Vacuum Science & Technology B **31**, 032203 (2013).

[31] J. Schalwig, G. Müller, M. Eickhoff, O. Ambacher, and M. Stutzmann, *Gas sensitive GaN/AlGaN-heterostructures,* Sensors and Actuators B: Chemical **87**, 425 (2002).

[32] J.-F. Xiao, C.-P. Hsu, I. Sarangadharan, G.-Y. Lee, J.-I. Chyi, and Y.-L. Wang, *Pt/GaN Schottky Diodes for Highly Sensitive Hydrogen Sulfide Detection,* ECS Journal of Solid State Science and Technology **5**, Q137 (2016).

[33] Z. Darmastuti, M. Andersson, L. Ojamäe, A. Lloyd Spetz, M. Larsson, and N. Lindqvist, *SiC based Field Effect Transistor for H2S detection,* in *SENSORS, 2011 IEEE* (2011) pp. 770–773.

[34] R. Sokolovskij, E. Iervolino, C. Zhao, F. Santagata, F. Wang, H. Yu, P. M. Sarro, and G. Q. Zhang, *Pt-AlGaN/GaN HEMT-Sensor for Hydrogen Sulfide (H_2S) Detection,* Proceedings **1**, 463 (2017).

[35] O. Ambacher, J. Smart, J. R. Shealy, N. G. Weimann, K. Chu, M. Murphy, W. J. Schaff, L. F. Eastman, R. Dimitrov, L. Wittmer, M. Stutzmann, W. Rieger, and J. Hilsenbeck, *Two-dimensional electron gases induced by spontaneous and piezoelectric polarization charges in N- and Ga-face AlGaN/GaN heterostructures,* Journal of Applied Physics **85**, 3222 (1999).

[36] R. Sohal, P. Dudek, and O. Hilt, *Comparative study of NH_4OH and HCl etching behaviours on AlGaN surfaces,* Applied Surface Science **256**, 2210 (2010).

[37] Y. H. Kahng, R. G. Tobin, R. Loloee, and R. N. Ghosh, *Sulfur surface chemistry on the platinum gate of a silicon carbide based hydrogen sensor,* Journal of Applied Physics **102**, 064505 (2007).

[38] A. Ortiz-Conde, F. J. García-Sánchez, J. Muci, A. T. Barrios, J. J. Liou, and C.-S. Ho, *Revisiting MOSFET threshold voltage extraction methods,* Microelectronics Reliability **53**, 90 (2013).

[39] D. R. Alfonso, *First-principles studies of H_2S adsorption and dissociation on metal surfaces,* Surface Science **602**, 2758 (2008).

[40] O. Weidemann, M. Hermann, G. Steinhoff, H. Wingbrant, A. Lloyd Spetz, M. Stutzmann, and M. Eickhoff, *Influence of surface oxides on hydrogen-sensitive pd:gan schottky diodes,* Applied Physics Letters **83**, 773 (2003).

[41] T.-H. Tsai, H.-I. Chen, K.-W. Lin, C.-W. Hung, C.-H. Hsu, T.-P. Chen, L.-Y. Chen, K.-Y. Chu, C.-F. Chang, and W.-C. Liu, *Hydrogen Sensing Characteristics of a Pd/AlGaN/GaN Schottky Diode,* Applied Physics Express **1**, 041102 (2008).

[42] C. Nylander, M. Armgarth, and C. Svensson, *Hydrogen induced drift in palladium gate metal-oxide-semiconductor structures,* Journal of Applied Physics **56**, 1177 (1984).

[43] M. Armgarth and C. Nylander, *Blister formation in Pd gate MIS hydrogen sensors,* IEEE Electron Device Letters **3**, 384 (1982).

[44] R. Duś and E. Nowicka, *Bivalent ability for charge transfer in process of hydrogen interaction with surfaces of transition metals,* Progress in Surface Science **67**, 139 (2001).

5

Recessed gate Pt-AlGaN/GaN H_2 sensors

The focus of this chapter is the fabrication and characterization of recessed gate Pt-AlGaN/GaN HEMT H_2 sensors. First, a method for highly controllable etching of AlGaN/GaN is developed. The process consists of cyclic oxidation of nitride with O_2 plasma using ICP-RIE etcher followed by wet etching of the oxidized layer. Previously reported cyclic oxidation-based GaN etching obtained very slow etching rate (~0.38 nm/cycle), limited by oxidation depth. The proposed approach allows fine control of the oxidation enabling the formation of accurately controlled recess of very thin (20~30 nm) barrier layers. With optimized power settings, etch rates from ~0.6 to ~11 nm/cycle were obtained. AFM results did not show any increase in surface roughness after etching, indicating that surface quality of the etched layer was not affected by the etching process. Pt-HEMT sensors were then fabricated with recessed gate depth from 5 to 15 nm and tested towards H_2 response at 240 °C. Shallow recess (5 nm) resulted in a 1.03 mA increase in signal variation (ΔI_{DS}), while deep recess (15 nm) resulted in highest sensing response of 145.8 % towards 300 ppm H_2 as compared to reference sensors without recess. Transient measurements demonstrated fully reversible H_2 response for all tested devices. The response time for 250 ppm decreased from 7.3 to 2.5 min and the recovery time from 29.2 to 8.85 min for 15 nm recess. The power consumption of the sensors reduced with increasing recess depth from 146.6 to 2.95 mW.

5.1. INTRODUCTION

Nowadays, most governments rely on non-renewable fossil fuels such as oil, natural gas and coal to meet the energy needs of growing manufacturing and transportation industries. The natural reserves of hydrocarbons are depleting and combustion of these materials is a major source of greenhouse gases and air pollutants such as CO, CO_2, NO_x, SO_x and particulates that have adverse health effects [1]. Adoption of renewable energy sources such as solar, wind or hydro power is required to alleviate fossil dependence. Hydrogen is a clean, sustainable synthetic fuel that is widely adopted in spacecraft propulsion systems by several nations [2]. Few technological hurdles still have to be overcome to advance H_2 utilization for personal and commercial vehicles. Storage and transportation of gaseous or liquid H_2 is challenging due to its physical and chemical properties. It is an odourless and colorless gas with high diffusivity, low boiling point of −253 °C and broad flammability range 4–75 % in air [3]. Therefore sensors capable of detecting a wide range of hydrogen concentrations are of critical importance for monitoring and prevention of leakage.

Various types of H_2 sensors have been developed over the last few decades. These include catalytic, electrochemical, optical, resistive or acoustic (also see section 1.3) [4]. Resistive type metal-oxide (MOX) based H_2 sensors with a wide range of sensing materials such as SnO_2 [5], In_2O_3 [6], Ga_2O_3 [7] and many others [8, 9] have been demonstrated.

Field effect devices such as MOS capacitors, Schottky diodes and MOSFETs are extensively studied as H_2 sensors ever since the first Si-FET with Pd gate was demonstrated by [10]. Due to the narrow bandgap of Si the maximum operating temperature of MOSFETs is limited to 200 °C. Other semiconductor materials including GaAs [11], AlGaAs [12], InAlAs [13] or SiC [14] were investigated for H_2 sensor applications in order to improve sensing characteristics and operate in harsh environments. Wide bandgap gallium nitride (GaN) has attracted immense interest for developing power switching devices [15] and next generation semiconductor sensors [16] due to its superior electronic, chemical, thermal and mechanical properties. Numerous GaN based H_2 sensors have been previously demonstrated. Since the initial report of the AlGaN/GaN HEMT H_2 sensor with Pt gate [17] numerous modifications to the structure have been studied in order to enhance the sensing characteristics as discussed earlier in section 2.2.2. Epitaxial AlGaN/GaN heterojunctions exhibit strong polarization effects, forming a high carrier density two dimensional electron gas (2DEG) channel at the interface, which results in intrinsically depletion-mode operation.

A specific and widely studied modification of AlGaN/GaN HEMTs is the recess etching of the thin (20~30 nm) AlGaN barrier in order to achieve enhancement-mode (E-mode) operation [18]. Partial barrier recess has also been applied to reduce ohmic contact resistance of Au-free, CMOS compatible contacts [19], V-gate HEMTs for power amplifiers with minimized dc-RF disperion [20] or lowering the turn-on voltage of Schottky barrier diodes [21]. Few reports have investigated the impact of barrier recess on sensing performance of HEMT-based sensors. Open gate AlGaN/GaN NO_2 sensor with varying barrier recess depths was reported by [22]. They found that thinning the AlGaN barrier resulted in increased response to low NO_2 concentrations under humid ambient conditions. A glucose biosensor with recessed barrier was demonstrated by [23]. Photoelectrochemical (PEC) etching using H_3PO_4 solution and He-Cd laser was utilized to partially recess the AlGaN barrier as well as to form a gate oxide layer consisting of Al_2O_3/Ga_2O_3. ZnO nanorods were then grown in the gate region and functionalized with glucose oxidase. Sensitivity towards pH and glucose was increased using the recessed structure.

AlGaN/GaN recess is commonly done by low power reactive ion etching (RIE) using Cl_2/BCl_3 plasma, which often exhibits difficulties of depth control, non-uniformities, etching residues and lattice damage due to ion bombardment. Increasing the substrate temperature from 20 °C to 180 °C during inductively coupled plasma (ICP) RIE etching was demonstrated to reduce the amount of Cl-based residues and lower the etched surface roughness [24]. PEC method was also demonstrated for recessing the barrier layer without damage [25]. However, this approach requires uniform intensity He-Cd laser illumination as well as precise pH control of the H_3PO_4 solution and leads to increased surface roughness [26]. Alternatively, thermal oxidation of AlGaN barrier at 650 °C, without oxidizing GaN, coupled with KOH oxide etching at 70 °C was successfully demonstrated [27]. Another approach to etch AlGaN/GaN consists of plasma surface oxidation followed by selective oxide etching with diluted acid. This method is commonly referred to as digital etching, because the two steps are repeated several times until desired etching depth is obtained [28]. Cyclic oxidation of AlGaN/GaN, using O_2 plasma asher, followed by wet hydrochloric acid (HCl) etching of the oxidized surface to fabricate recessed-gate GaN MOSFETs was reported in [29]. Using 300 W RF power for 3 min, an etching rate of ~0.38 nm/cycle was obtained, being too slow for most barrier recess applications.

In this chapter, we first develop a novel method for precise, low damage cyclic etching of AlGaN/GaN for precision barrier recess applications, using ICP-RIE oxidation and wet etching. Optimization of equipment power settings allowed to obtain a wide range of etching rates ~0.6 to ~11 nm/cycle without any observable increase in surface roughness with respect to the unetched surface. We then implement this method in our processing flow to fabricate Pt-AlGaN/GaN recessed gate H_2 sensors and study their gas response characteristics.

5.2. EXPERIMENTAL

5.2.1. PRECISION RECESS OF ALGAN/GAN USING ICP-RIE OXIDATION

The experimental work on the two-step etching process was carried out in the IOS cleanroom in Beijing. The epitaxial structure of AlGaN/GaN on sapphire, as described in section 2.3.1, was used for recess etching process development. The wafer surface was cleaned with acetone and isopropanol. Then 300 nm of SiO_2 were deposited by PECVD and used as a hard mask during the etching experiments. The oxide was patterned with photoresist and etched with buffered oxide etchant (BOE), as it does not etch the underlying semiconductor layers. After photoresist removal, the 2 inch wafers were laser scribed into 7 mm × 7 mm chips to be used for recess etching experiments. Prior to first oxidation, native oxide was removed by HCl solution dip. Nitride oxidation was done with ICP-RIE etcher using O_2 plasma for 3 min followed by 1 min oxide etch using 1:4/HCl:H_2O solution at room temperature. Two ICP-RIE systems from two different vendors (AST and Oxford Instruments) with different ICP source and RF bias generator power ranges were used. Oxidation recipe parameters for both systems are summarized in table 5.1. Only O_2 gas was injected into the chamber during oxidation process. Three chips were loaded into the etching chamber simultaneously with random orientations for testing each oxidation recipe. After 3 or 4 etching cycles the SiO_2 mask was removed with BOE. Etching depth and surface roughness were measured using Bruker Dimension Edge AFM. Average etch rate per cycle was determined by measuring multiple points across the test samples.

Table 5.1: Process recipe information for ICP-RIE oxidation.

Parameter	**AST Cirie-200**	**Oxford Plasmalab 100**
O_2 flow rate (sccm)	40	40
Pressure (mtorr)	8	8
ICP power (W)	150–450	450
ICP range (W)	0–2000	200–2500
RF power (W)	15–150	75
RF range (W)	0–600	5–400
Oxidation time (s)	180	180

5.2.2. CHARACTERIZATION RESULTS

We have investigated the effects of ICP and RF power on O_2 plasma oxidation of AlGaN/GaN, while other settings were kept constant for all experiments. Average etching rates for the tested RF and ICP power range, using AST system, are shown in fig. 5.1. Obtained results showed a linear increase in etching rate with increasing RF power. A wide range of average etching rate from ~0.6 to ~6nm/cycle was achieved. The dependency on ICP power was less noticeable, with little variation in etching rate, especially for 300 W and 450 W ICP power. The RF generator is used to control the energy of plasma ions while ICP generator is used to optimize plasma density. We conclude that higher energy O_2 ions can penetrate deeper into the nitride layer to form thicker oxide, while the plasma density was not depleted considerably for the tested range, to significantly influence the oxidation process. A 3.4x higher etching rate (11 nm/cycle) was obtained when using Oxford Instruments system in comparison to AST (3.22 nm/cycle) when using same power parameters 450 W/75 W (ICP/RF). These differences could be attributed to numerous equipment design variations e.g. the usable generator power range, chamber size and design, ion energy, etc. Therefore equipment specific optimizations should be carried it out in order to obtain the desired oxidation depth. After 3 cycles of etching with the Oxford Instruments tool the measured step height was 33 nm, indicating that the GaN buffer was also etched.

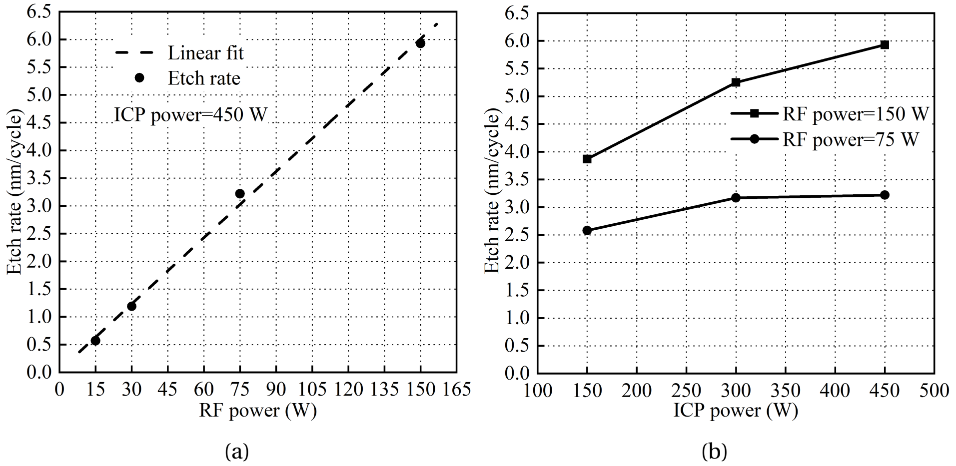

(a) (b)

Figure 5.1: Etch rate dependency on (a) RF power at constant ICP power and (b) ICP power at constant RF power using the AST etcher.

Surface damage after ICP-RIE oxidation based etching was evaluated by roughness measurements. AFM surface morphology images of the unetched (after SiO_2 mask removal with BOE) and etched layers are shown in figs. 5.2a and 5.2b. After 3 cycles of etching with 450 W/150 W (ICP/RF) recipe using AST system the RMS roughness remained unchanged. Roughness was also not altered after etching with Oxford Instruments sys-

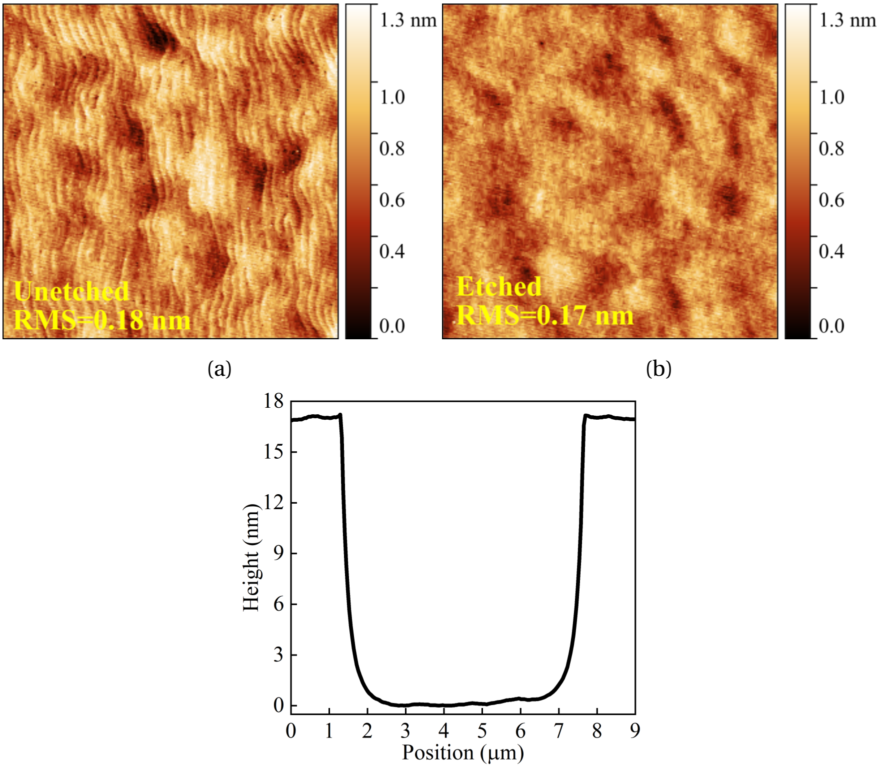

(a) (b)

(c)

Figure 5.2: AFM surface morphology images of (a) unetched and (b) etched surfaces using AST 450 W/75 W (ICP/RF) recipe and (c) etched profile after 3 oxidation/etching cycles.

tem with unetched and etched RMS roughness values of 0.22 nm and 0.21 nm, respectively. Unlike plasma etch, wet etching of the oxide layer with HCl is selective towards the nitride layer, hence no surface damage is induced on the underlying AlGaN/GaN. A step profile across a 6 µm trench (fig. 5.2c) shows smooth and uniform bottom surface.

5.2.3. SENSOR FABRICATION PROCESS

The same epitaxial AlGaN/GaN structure was used to fabricate the Pt-HEMT sensors with recessed gate in the Shenzhen SUSTech cleanroom. The process started with wafer cleaning using piranha solution (3:1/H_2SO_4:H_2O_2) followed by acetone, isopropanol and DI water rinsing to remove any particulates or organic contaminants. Mesa etching was then performed using ICP-RIE with BCl_3/Cl_2 plasma to the depth of 100 nm. Afterwards 200 nm of PECVD SiO_2 were deposited and patterned by BOE etching to be used as hard mask for barrier recess. A Naura GSE 200 Plus ICP-RIE tool was used for plasma oxidation of the GaN cap and AlGaN barrier layers. The recipe parameters were similar to those used in IOS, with ICP power 450 W, O_2 flow rate of 40 sccm, base pressure 8 mtorr, oxidation time 180 s. The RF power was varied in the range of 20–75 W to modify the oxidation depth rate per cycle and 1:4/HCl:H_2O was used to etch the formed oxide. Sensors with four different recess depths were fabricated for comparison, denoted as samples B, C, D and E, while sample A was a reference without gate recess. The SiO_2 mask was then removed by BOE etching. The ohmic contact patterns were formed by photolithographic patterning, e-beam evaporation of Ti/Al/Ti/Au (20/110/40/50 nm) and lift-off. Prior to the metal deposition a dip in 1:4/HCl:H_2O was done in order to remove any surface oxide. Rapid thermal annealing at 850 °C for 45 s in N_2 ambient was performed to obtain low contact resistance ohmic contacts. 10 nm of Pt were then e-beam deposited and patterned to form the sensing gate electrode. Afterwards the interconnect bi-layer of Ti/Au with thickness 20/300 nm was processed with e-beam evaporation and lift-off. Device passivation was then carried out by depositing 200 nm of SiN_x in order to protect the GaN surface and metal interconnects from scratches and contamination. The SiN_x was then patterned by a combination of ICP-RIE followed by wet BOE etching to expose the Pt gate and the contact pads for wire bonding. The schematic cross-section view of the HEMT-sensor structure with a recessed gate electrode is shown in fig. 5.3a and the top view optical micrograph of the processed sensor in fig. 5.3b. The dimensions of the gate electrode exposed to the ambient were 4 µm×400 µm, the source-gate and gate-drain spacings were 6 µm.

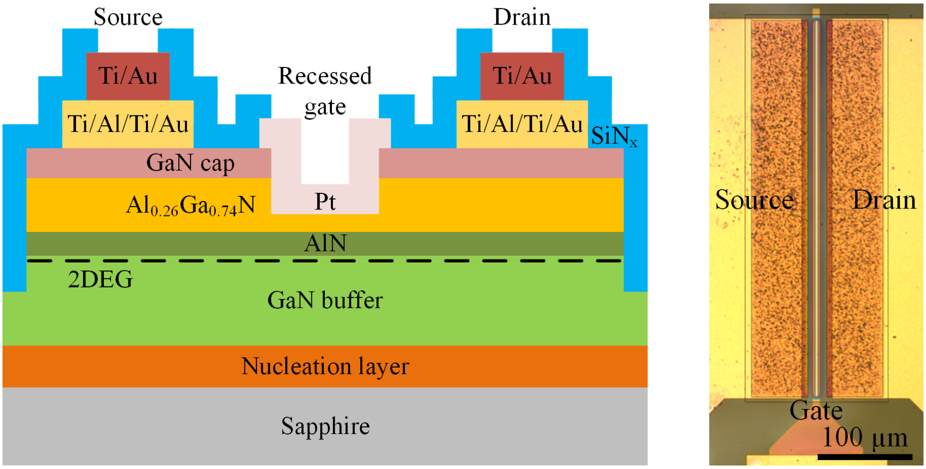

(a) (b)

Figure 5.3: Schematic cross-section of the recessed gate Pt-AlGaN/GaN HEMT H_2 sensor (a). Top view optical micrograph of the fabricated sensor (b).

5.2.4. SENSOR TESTING PROCESS

The fabricated wafers were diced using laser scribing. Individual sensors were then wire-bonded to ceramic substrates and placed in a stainless steel 100 ml chamber with a heater and humidity sensor. The concentration of the test gas and the relative humidity inside the testing chamber were controlled with mass flow controllers using a commercial gas mixing system from Beijing Elite Tech Co (see fig. 3.4). The test gas was supplied from H_2 cylinders with known concentration, diluted with N_2. The background gas was synthetic air (O_2/N_2=21 %/79 %). Electrical connections to the sensors were made with probe needles inside the test chamber and current-voltage characteristics were measured using two Keithley 2450 sourcemeters. Prior to H_2 sensing, fresh sensors underwent a burn-in process at 260 °C for 12 h in order to reduce the baseline signal drift.

5.3. RESULTS AND DISCUSSION

In order to validate the cyclic nature of the two-step barrier recess process, scanning transmission electron microscopy (STEM) imaging was conducted on test samples using FEI Talos STEM with 200 kV acceleration voltage. Figure 5.4a shows the cross-sectional view of the patterned sample after 180 s ICP-RIE oxidation at 40 W RF power. A thin layer of oxide has formed on the plasma exposed surface and part of the AlGaN layer was consumed as a result. The thickness of the oxide was 4.1 nm as determined from the magnified view of the oxidized area shown in fig. 5.4b. The Au and carbon layers were deposited to protect the chip surface from plasma damage during TEM sample prepa-

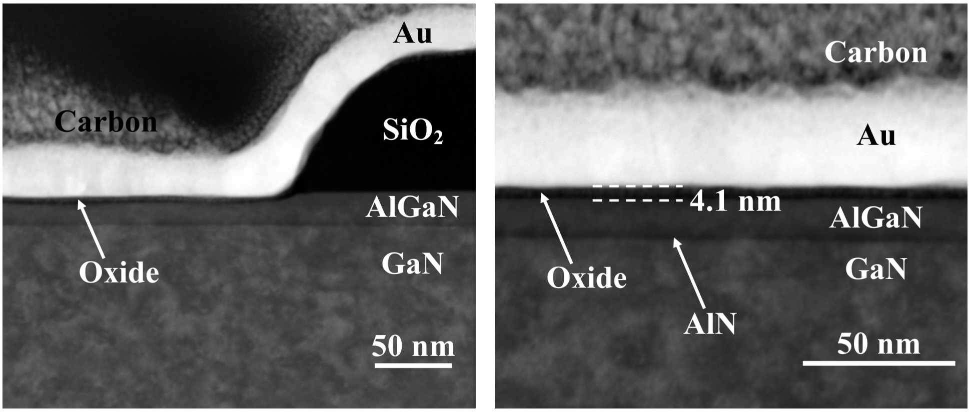

(a) (b)

Figure 5.4: Cross-section STEM images of (a) edge of the pattern exposed to oxygen plasma treatment and (b) a magnified view of the oxidized AlGaN surface.

ration using focused ion beam (FIB). Energy dispersive spectroscopy (EDS) analysis was carried out in order to examine the composition of the layer formed by exposure to oxygen plasma as shown in fig. 5.5. The presence of O, Al and Ga is clearly observed in the oxidized film, whereas N concentration is diminished. The likely reaction mechanism of plasma oxidation is:

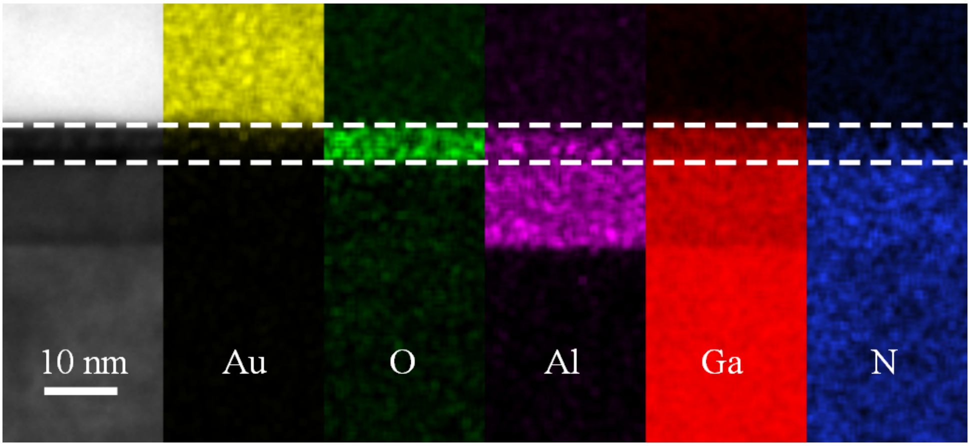

Figure 5.5: EDS element mapping of the oxygen plasma exposed AlGaN surface. The area between the dashed lines indicates the location of the oxidized surface.

$$2\,\mathrm{AlGaN} + 6\,\mathrm{O}^* \longrightarrow \mathrm{Ga_2O_3} + \mathrm{Al_2O_3} + \mathrm{N_2}\uparrow \tag{5.1}$$

where O^* are the excited oxygen plasma atoms. The depth of recess was measured by atomic force microscopy (AFM) using Bruker Dimension Edge. The depth profiles of the barrier recess across a 5 µm wide test structure are shown in fig. 5.6. The RF power settings of plasma oxidation recipes, the exact measured recess depth and trench surface roughness for samples B–E are collected in table 5.2. A low surface roughness was measured for all depths. Samples B-D required 2 oxidation/etching cycles to obtain the

Table 5.2: Plasma RF power conditions, etch depth and surface roughness of recessed regions, measured by AFM, of sensors B–E.

Sensor	**Oxidation RF power (W)**	**Measured depth (nm)**	**Roughness (nm)**
B	20+20	5.4	0.57
C	75+40	10.1	0.51
D	75+75	12.3	0.54
E	75+75+35	15	0.56

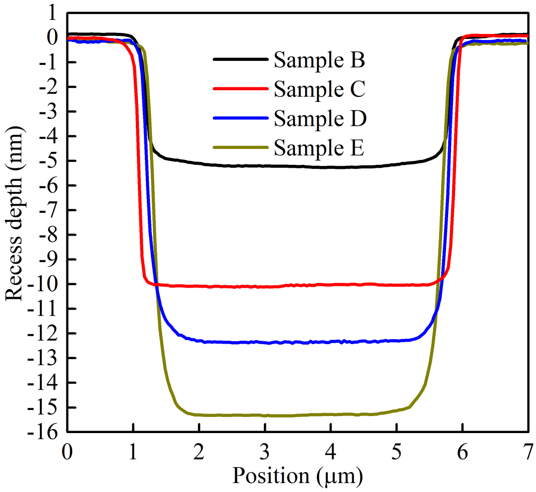

Figure 5.6: Depth profiles obtained by AFM scans of samples B, C, D and E across 5 µm test trenches.

desired etching depth, while 3 cycles were used for sample E. The cross-section STEM image of the non-recessed and recessed AlGaN regions of sample D is shown fig. 5.7a and the edge of the sensing gate electrode exposed to H_2 in fig. 5.7b. An interfacial layer of

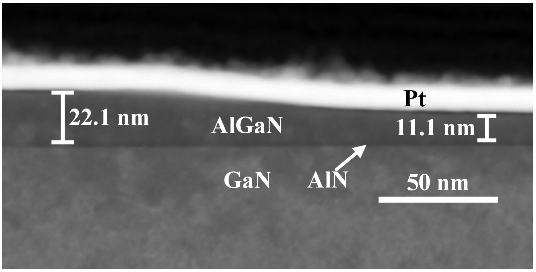

(a)

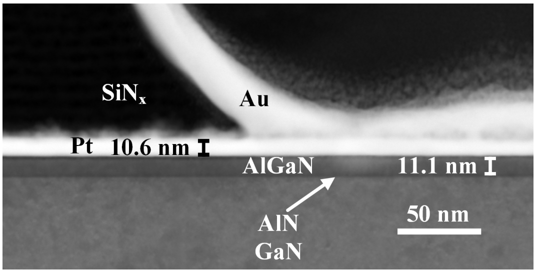

(b)

Figure 5.7: Cross-section STEM images of (a) the non-recessed and recessed AlGaN region and (b) the edge of the gate electrode exposed to H_2 gas of sensor D.

oxide was observed between the Pt gate and AlGaN. It is possible that this oxide formed due to exposure to atmosphere and during contact RTA, as residual H_2O and O_2 may be present in N_2 atmosphere of the annealing chamber [30].

Electrical measurements were conducted in order to determine the influence of gate recess depth on the characteristics of the studied sensors prior to gas sensing experiments. The transfer curves ($I_{DS} - V_{GS}$) of devices A-E at 30 °C are shown in fig. 5.8a. A clearly evident shift of the curves towards positive values is observed with increasing depth of barrier recess. The threshold voltages of these devices were extracted by fitting a tangent line at the point of maximum transconductance ($g_{m,max}$) to the x-axis intercept (i.e. $I_{DS} = 0$) [31]. Figure 5.8b shows the shift of V_{TH} with increasing recess depth. The V_{TH} increased from -1.57 V for the non-recessed sensor A to $V_{TH} = 1.49$ V for sensor E with ~15 nm recess depth, which resulted in enhancement mode device.

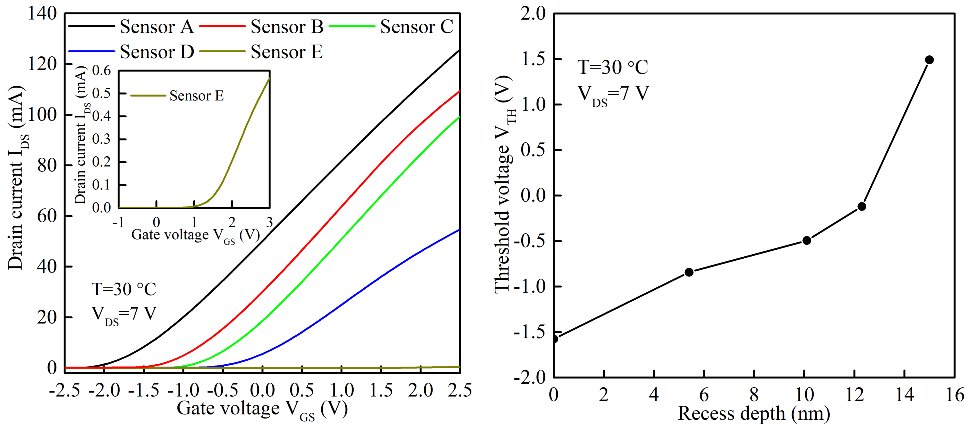

(a) (b)

Figure 5.8: (a) Transfer characteristics ($I_{DS} - V_{GS}$) of sensors A–E at room temperature. The inset shows the magnified view of sensor E. (b) Threshold voltage shift with increasing depth of barrier recess.

Output ($I_{DS} - V_{DS}$) characteristics of sensors with different recess depth are shown in fig. 5.9. The gate voltage (V_{GS}) of sensors A to D was stepped from -3 V to 1 V with 1 V increments and from -1 V to 3 V with 0.5 V steps for sensor E. All devices demonstrated good transistor characteristics with clear linear and saturation regions as well as pinch-off below V_{TH}. The maximum drain current ($I_{DS,max}$) decreased with deeper recess depth due to reduction of the electron density under the gate electrode and increase in the channel resistance (R_{ch}) according to [18]:

$$R_{ch} = \frac{L_g t_r}{\mu \epsilon_0 \epsilon (V_{GS} - V_{TH} - \phi_b)} \tag{5.2}$$

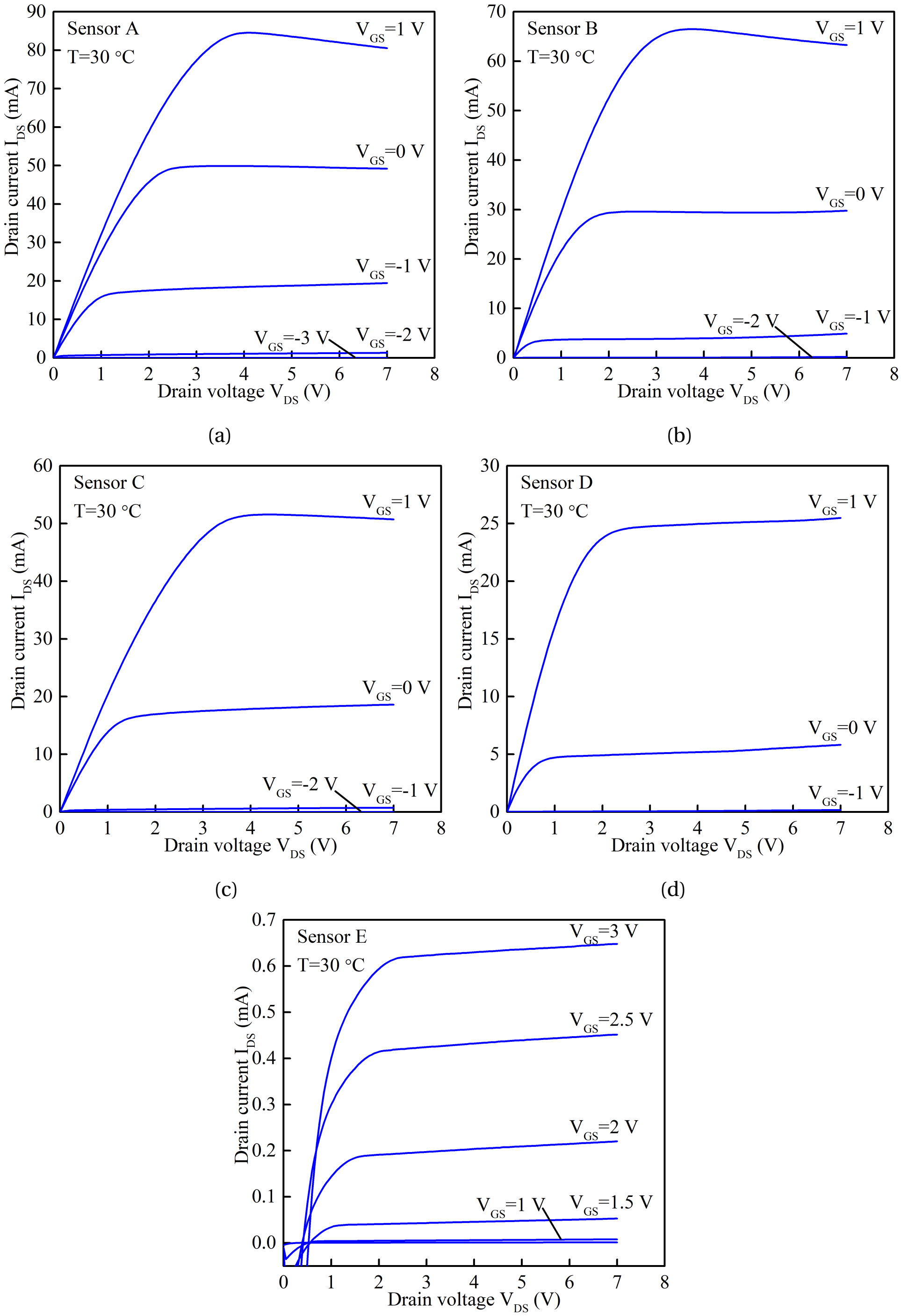

(a)

(b)

(c)

(d)

(e)

Figure 5.9: Output characteristics ($I_{DS} - V_{DS}$) of fabricated (a) sensor A, (b) sensor B, (c) sensor C, (d) sensor D, (e) sensor E at room temperature.

where L_g is the gate length, t_r the thickness of the AlGaN barrier under the gate, μ is the electron mobility, ϕ_b is the Schottky barrier height ϵ_0 and ϵ are the dielectric permittivity of vacuum and AlGaN, respectively. The relation between the 2DEG density of the non-recessed (n_s) and recessed (n_{sr}) region can be expressed as:

$$n_{sr} = n_s\left(1 - \frac{t_{cr}}{t_r}\right) \tag{5.3}$$

where t_{cr} is the critical AlGaN thickness at witch 2DEG forms [32] and is expressed as:

$$t_{cr} = \frac{(\phi_b - \Delta E_C)\epsilon_0\epsilon}{qn_s} \tag{5.4}$$

where ΔE_C is the conduction band offset between AlGaN and GaN. The dependence of threshold voltage on the barrier thickness can then be expressed as:

$$V_{TH} = \phi_b + \frac{qn_s}{\epsilon_0\epsilon}(t_{cr} - t_r) \tag{5.5}$$

Compared with other sensors the drain current of device E reduced substantially. This is attributed to significant reduction of 2DEG density as the barrier was recessed down to near critical thickness t_{cr}. Furthermore the voltage difference ($V_{GS} - V_{TH}$) is reduced for E-mode HEMT leading to additional increase of R_{ch}. Biasing the device at higher gate voltage leads to forward bias gate leakage as evident from the shift of drain voltage axis crossing point and reverse current at low V_{DS} (see fig. 5.9e).

Sensing characteristics of the fabricated sensors were examined by exposing them to increasing concentrations of H_2 in dry air at 240 °C. The measured transfer characteristics of sensors A–E at V_{DS}=7 V exposed to 5–300 ppm H_2 are shown in fig. 5.10. All devices demonstrated response to low H_2 concentrations as evident from V_{TH} shift towards more negative values. The threshold voltage shift ($\Delta V_{TH} = V_{TH,air} - V_{TH,\mathrm{H}_2}$) of the tested sensors with increasing recess depth upon exposure to 300 ppm of H_2 is shown in fig. 5.10f. Compared to reference sensor A the ΔV_{TH} was higher for sensors B and C, while it reduced for sensors D and E, which corresponds to the measured maximum transconductance ($g_{m,max}$) values in air of 12.26, 14.66, 14.05, 9.02 and 0.32 mS of sensors A–E, respectively. The corresponding output characteristics upon H_2 exposure are shown in fig. 5.11. The gate voltage was stepped from −3 V to 1 V with 1 V increments for sensors A–D and from −1 V to 3 V for sensor E. The devices still maintained proper characteristics at high temperature above the Si-based FET limit. The drain current (I_{DS}) increased upon H_2 exposure down to 5 ppm. The detection principle is based on catalytic dissociation of H_2 molecules into 2H atoms at the surface of the Pt gate. Some of these

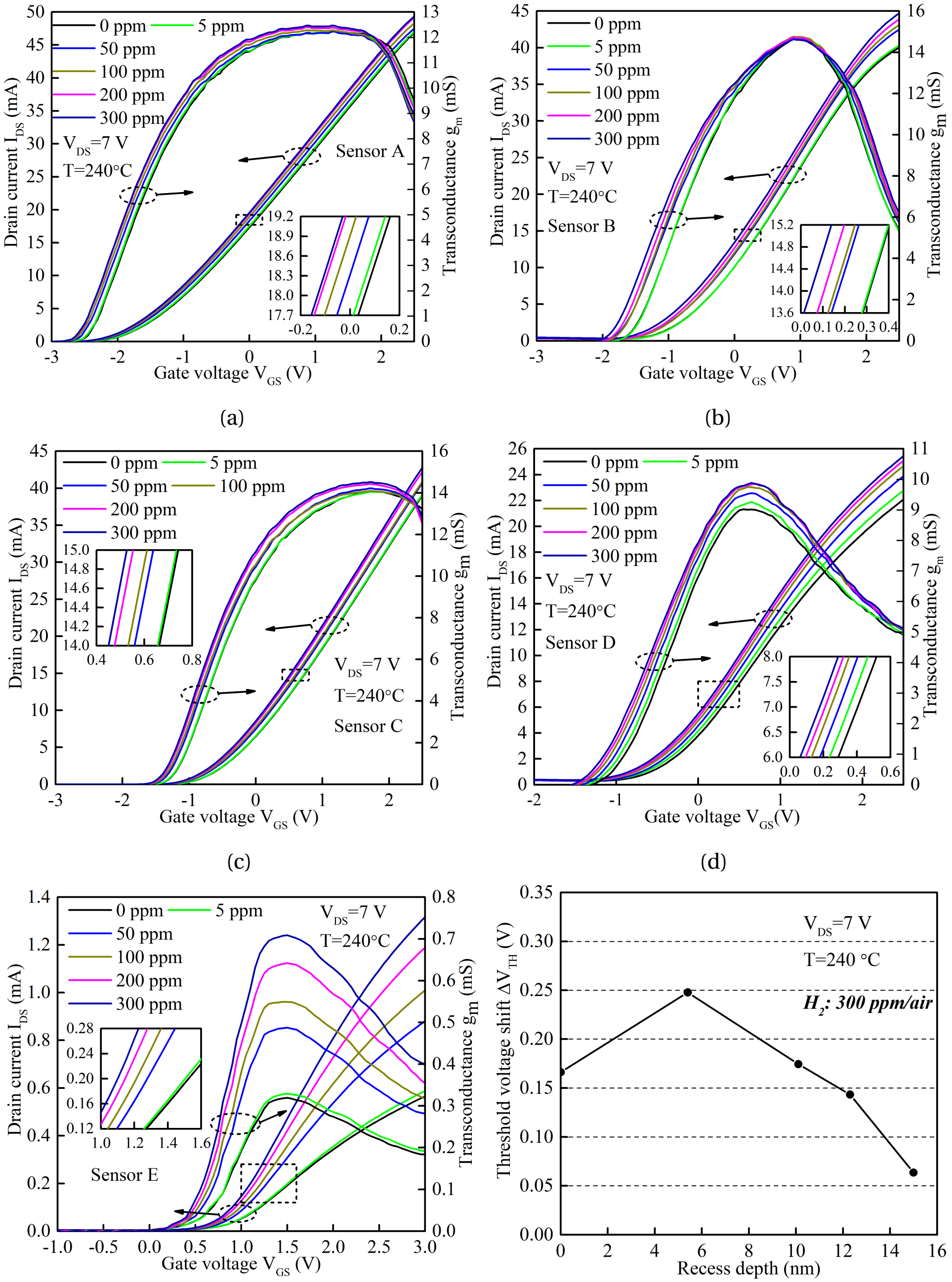

(a) (b) (c) (d) (e) (f)

Figure 5.10: Transfer characteristics ($I_{DS}-V_{GS}$) of (a) sensor A, (b) sensor B, (c) sensor C, (d) sensor D and (e) sensor E exposed to different H_2 concentrations at 240 °C. The insets show the magnified view of the box area. (f) The threshold voltage shift (ΔV_{TH}) from air to 300 ppm H_2 as a function of recess depth.

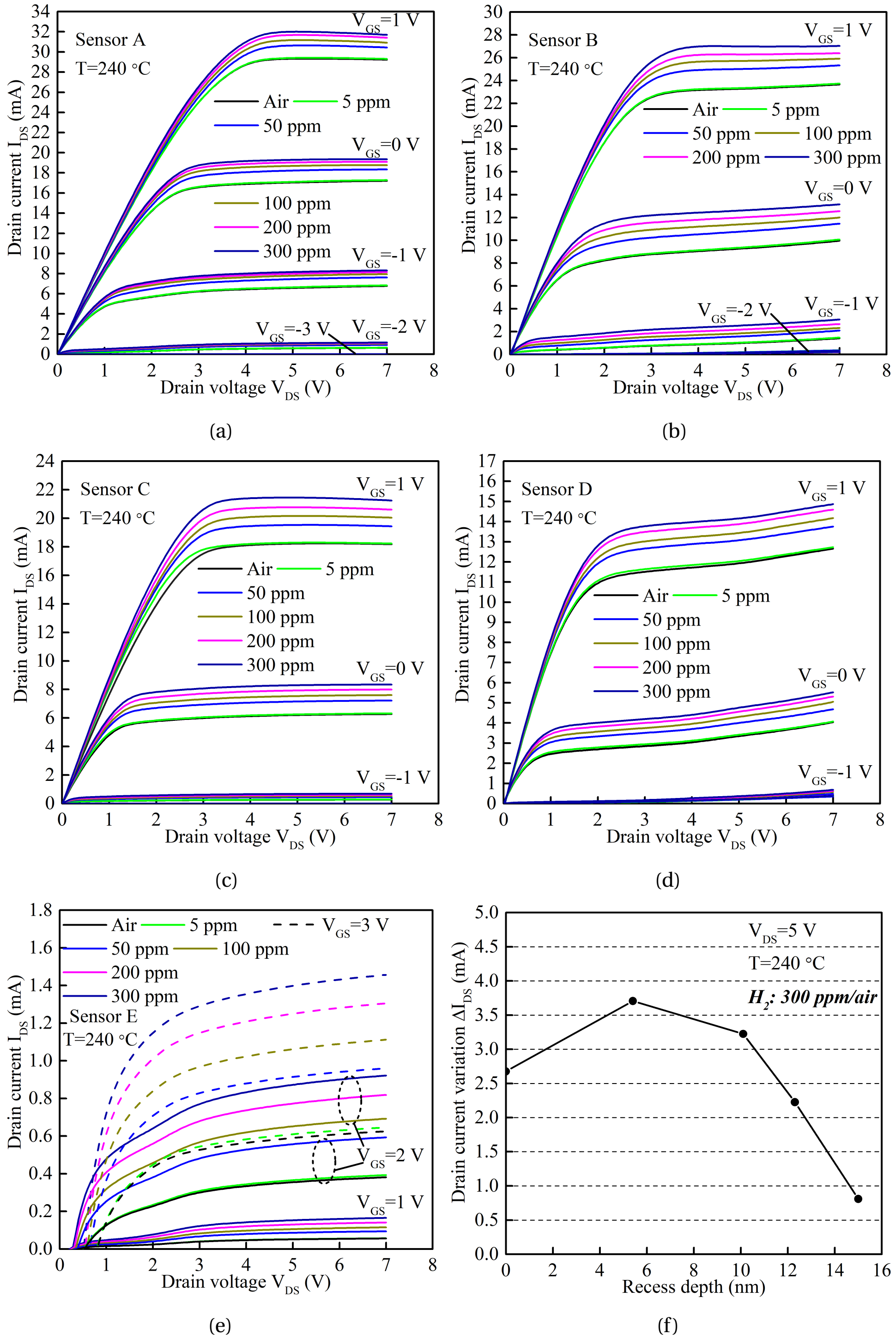

(a) (b) (c) (d) (e) (f)

Figure 5.11: Output characteristics ($I_{DS} - V_{DS}$) of (a) sensor A, (b) sensor B, (c) sensor C, (d) sensor D and (e) sensor E exposed to different H_2 concentrations at 240 °C. (f) The drain current variation (ΔI_{DS}) from air to 300 ppm H_2 as a function of recess depth.

atoms rapidly diffuse through the Pt towards the metal-semiconductor interface and form a dipolar layer. The dipoles cause a reversible lowering of the Pt work function, which results in the observed negative threshold voltage shift (ΔV_{TH}) and output current increase (ΔI_{DS}) [33].

To characterize and compare the H_2 sensing performance of the studied sensors the drain current variation ΔI_{DS} and sensing response (S) were extracted. The S is defined as:

$$S(\%) = \frac{I_{DS,H_2} - I_{DS,air}}{I_{DS,air}} \times 100\% = \frac{\Delta I_{DS}}{I_{DS,air}} \times 100\% \tag{5.6}$$

where I_{DS,H_2} and $I_{DS,air}$ is the drain current magnitude under H_2 containing and air ambient, respectively. The drain current variation (ΔI_{DS}) as a function of recess depth is shown in fig. 5.11f. The drain bias of all devices was V_{DS} =5 V and the gate bias (V_{GS}) was 1 V for devices A–D and 3 V for device E. Compared to sensor A the ΔI_{DS} increased from 2.68 mA to 3.71 mA for sensor B and 3.22 mA for sensor C when exposed to 300 ppm H_2 and decreased with deeper recess. The sensing response (S) towards H_2 of the tested sensors is shown in fig. 5.12. The V_{DS}=5 V for all sensors and V_{GS}=0 V for sensors A–D and

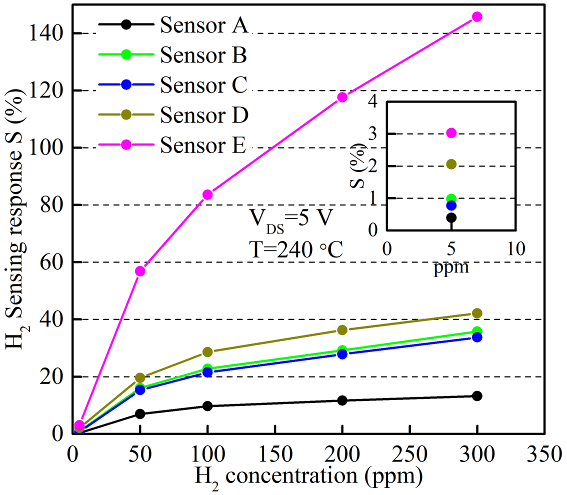

Figure 5.12: Hydrogen sensing response of sensors A–E at 240 °C. The V_{GS}=0 V for A–D and V_{GS}=2 V for sensor E. The inset shows the magnified S towards 5 ppm.

V_{GS}=2 V for sensor E. The S towards 300 ppm of H_2 increased from 13.23 % for sensor A to 35.84, 33.76, 42.15 and 145.77 % for sensor B–E, respectively. A 11x increase in sensing response was obtained for a 15 nm recess depth compared to non-recessed sensor.

Transient response characteristics of the Pt-AlGaN/GaN HEMT sensors at 240 °C towards 10–250 ppm H_2 are shown in fig. 5.13. The sensors A-D were biased at V_{GS}=0 V,

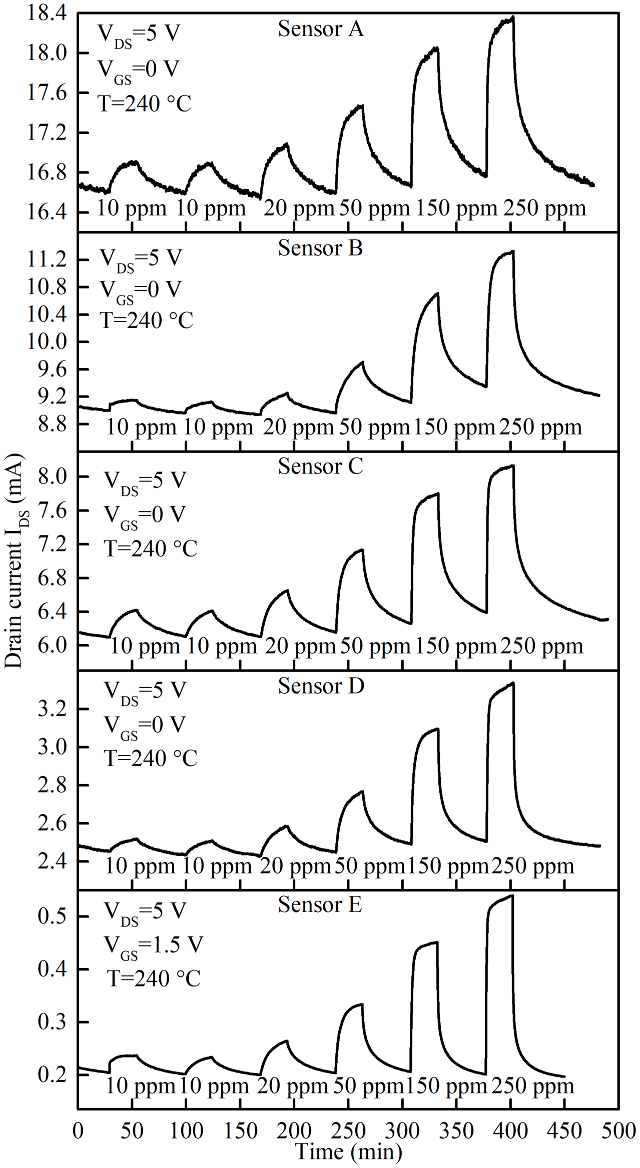

Figure 5.13: Transient response characteristics upon injection and purge of H_2 at 240 °C for sensors A–E with increasing depth of recess. The V_{GS}=0 V for A–D, and V_{GS}=1.5 V for sensor E.

sensor E at V_{GS}=1.5 V and the V_{DS}=5 V for all tested sensors. The drain current increased immediately after gas was introduced into the test chamber. The response (t_{res}) and recovery time (t_{rec}) of the tested sensors towards 250 ppm with increasing recess depth is shown in fig. 5.14. The t_{res} is defined as the time required for the sensors to reach

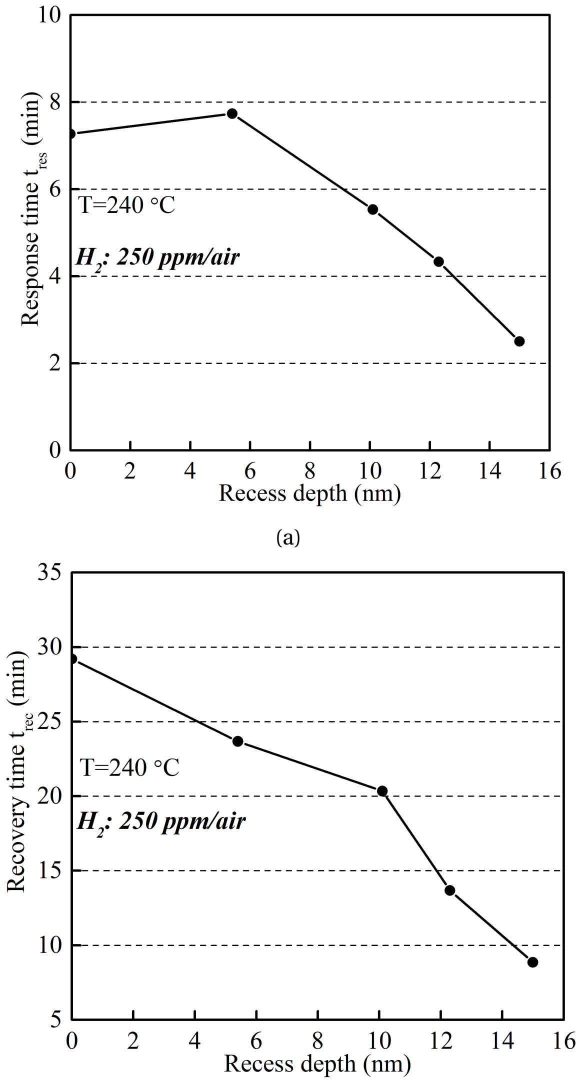

(a)

(b)

Figure 5.14: The (a) response (t_{res}) and (b) recovery (t_{rec}) time of sensors A-E as a function of recess depth. The V_{GS}=0 V for A–D, and V_{GS}=1.5 V for sensor E.

90 % of the equilibrium I_{DS} value in H_2 and t_{rec} is the time needed for I_{DS} to return to 10 % above the value in air. Both t_{res} and t_{rec} gradually decreased with thinning the AlGaN barrier. The response time decreased from 7.26 min for non-recessed sensor A to 2.5 min for sensor E with 15 nm recess and the recovery time decreased from 29.2 min to 8.85 min, respectively. Sensor signal repeatability was studied by exposing them to three

successive cycles of 250 ppm H_2 for 25 min followed by air purging for 60 min as shown in fig. 5.15. Repeatable sensor signal variation was observed for all sensors, indicating that recessing the barrier does not deteriorate the transient sensor operation.

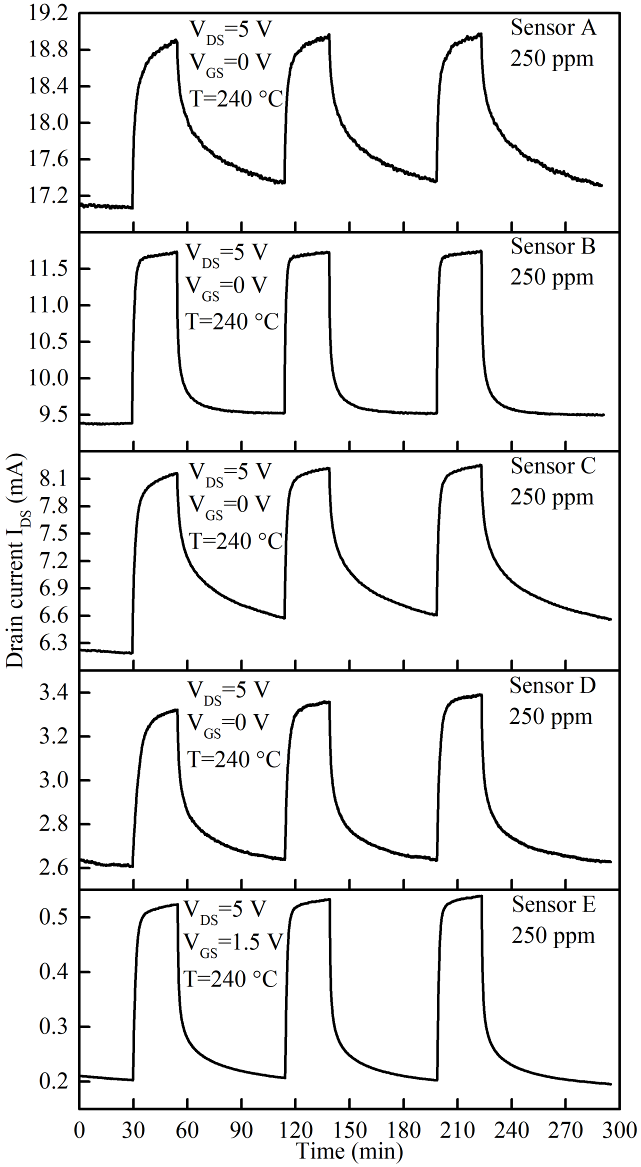

Figure 5.15: Repeatability characteristics upon injection and purge of 250 ppm H_2 at 240 °C for sensors A–E with increasing depth of recess. The V_{GS}=0 V for A–D, and V_{GS}=1.5 V for sensor E.

Reducing the power consumption of AlGaN/GaN HEMT based micro-sensors is crucial for integration into portable and battery powered gas detectors. The comparison of continuous power consumption is given in fig. 5.16. The power values were calculated at V_{DS}=5 V and V_{GS} of 0 and 1 V for sensors A–D, while for sensor E the V_{GS} was 2 and 3 V. The power consumption decreased from 85.2 (146.6) mW to 1.8 (2.95) mW when comparing sensors A and E at V_{GS} 0 (1) V and 2 (3) V, respectively. The obtained 48x power reduction is significant as additional power would be required to raise the operating temperature of the sensors via integrated microheater in real-world application scenario.

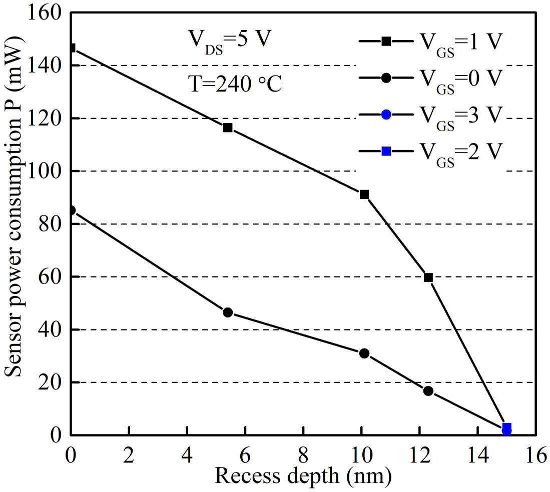

Figure 5.16: Power consumption values for sensors A–E at 240 °C and V_{DS}=5 V.

5.4. CONCLUSIONS

In this chapter, a precision, low damage cyclic etching of AlGaN/GaN using ICP-RIE oxidation and wet etching was developed. Controllable etching rates in 0.6~11nm/cycle range were obtained. This method is highly promising for the formation of accurate recess of few to several tenths of nm in the thin AlGaN/GaN layers. It was then implemented to fabricate HEMT-based H_2 sensors.

Sensors with increasing gate recess depths from 5 to 15 nm were processed using the aforementioned barrier etching method. The surface roughness of the recessed regions was studied with AFM and recessed profile and Pt-AlGaN interface was examined by STEM and EDS. Room temperature DC characteristic measurement showed a reduction of output current (I_{DS}) with increasing recess depth and a positive shift of threshold voltage from −1.57 V to 1.49 V going from non-recessed to 15 nm recess, due to the lowering of the 2DEG density under the thinner AlGaN layer under the gate.

High temperature (240 °C) static and transient H_2 sensing characteristics were studied and compared with a baseline sensor without gate recess. Exposure to H_2 resulted in the increase in current (ΔI_{DS}) and negative shift of threshold voltage (ΔV_{TH}). All the tested sensors were able to detect low H_2 concentrations down to 5 ppm. The largest ΔI_{DS} and ΔV_{TH} of 3.71 mA and 0.25 V at 300 ppm was obtained for sensors with shallow recess of ~5 nm, which was 1.03 mA and 0.08 V higher than of the reference sensor. The sensing response at 300 ppm gradually increased with recess depth from 13.2 % for non-recessed sensor to 145.8 % for sensor with 15 nm recess depth. Transient measurements with increasing H_2 concentration revealed superb response, recovery as well as repeatability characteristics. Comparing non-recessed and 15 nm recessed sensors the response (recovery) time decreased from 7.3 (29.2) min to 2.5 (8.85) min, respectively. Power consumption of the sensors was effectively reduced by implementing barrier recess from 146.6 to 2.95 mW. Therefore, precisely etching a recess in the barrier layer under the Pt sensing gate electrode is an effective method to enhance the static in transient sensing characteristics of AlGaN/GaN HEMT H_2 sensors.

REFERENCES

[1] M. Kampa and E. Castanas, *Human health effects of air pollution,* Environmental Pollution **151**, 362 (2008).

[2] D. Cecere, E. Giacomazzi, and A. Ingenito, *A review on hydrogen industrial aerospace applications,* International Journal of Hydrogen Energy **39**, 10731 (2014).

[3] Y. S. Najjar, *Hydrogen safety: The road toward green technology,* International Journal of Hydrogen Energy **38**, 10716 (2013).

[4] T. Hübert, L. Boon-Brett, G. Black, and U. Banach, *Hydrogen sensors – A review,* Sensors and Actuators B: Chemical **157**, 329 (2011).

[5] S. Ansari, P. Boroojerdian, S. Sainkar, R. Karekar, R. Aiyer, and S. Kulkarni, *Grain size effects on H_2 gas sensitivity of thick film resistor using SnO_2 nanoparticles,* Thin Solid Films **295**, 271 (1997).

[6] W.-Y. Chung, G. Sakai, K. Shimanoe, N. Miura, D.-D. Lee, and N. Yamazoe, *Preparation of indium oxide thin film by spin-coating method and its gas-sensing properties,* Sensors and Actuators B: Chemical **46**, 139 (1998).

[7] M. Fleischer and H. Meixner, *Improvements in Ga_2O_3 sensors for reducing gases,* Sensors and Actuators B: Chemical **13**, 259 (1993).

[8] V. Aroutiounian, *Metal oxide hydrogen, oxygen, and carbon monoxide sensors for hydrogen setups and cells,* International Journal of Hydrogen Energy **32**, 1145 (2007).

[9] G. Korotcenkov and B. Cho, *Metal oxide composites in conductometric gas sensors: Achievements and challenges,* Sensors and Actuators B: Chemical **244**, 182 (2017).

[10] K. I. Lundström, M. S. Shivaraman, and C. M. Svensson, *A hydrogen-sensitive Pd-gate MOS transistor,* Journal of Applied Physics **46**, 3876 (1975), https://doi.org/10.1063/1.322185 .

[11] L. Lechuga, A. Calle, D. Golmayo, and F. Briones, *Hydrogen sensor based on a Pt/GaAs Schottky diode,* Sensors and Actuators B: Chemical **4**, 515 (1991).

[12] C.-T. Lu, K.-W. Lin, H.-I. Chen, H.-M. Chuang, C.-Y. Chen, and W.-C. Liu, *A new Pd-oxide-$Al_{0.3}Ga_{0.7}As$ MOS hydrogen sensor,* IEEE Electron Device Letters **24**, 390 (2003).

[13] C.-W. Hung, T.-H. Tsai, H.-I. Chen, Y.-Y. Tsai, T.-P. Chen, L.-Y. Chen, K.-Y. Chu, and W.-C. Liu, *Temperature-dependent hydrogen sensing characteristics of a new Pt/InAlAs Schottky diode-type sensor,* Sensors and Actuators B: Chemical **128**, 574 (2008).

[14] M. T. Soo, K. Y. Cheong, and A. F. M. Noor, *Advances of SiC-based MOS capacitor hydrogen sensors for harsh environment applications,* Sensors and Actuators B: Chemical **151**, 39 (2010).

[15] B. J. Baliga, *Gallium nitride devices for power electronic applications,* Semiconductor Science and Technology **28**, 074011 (2013).

[16] S. Pearton, F. Ren, Y.-L. Wang, B. Chu, K. Chen, C. Chang, W. Lim, J. Lin, and D. Norton, *Recent advances in wide bandgap semiconductor biological and gas sensors,* Progress in Materials Science **55**, 1 (2010).

[17] J. Schalwig, G. Müller, M. Eickhoff, O. Ambacher, and M. Stutzmann, *Gas sensitive GaN/AlGaN-heterostructures,* Sensors and Actuators B: Chemical **87**, 425 (2002).

[18] W. Saito, Y. Takada, M. Kuraguchi, K. Tsuda, and I. Omura, *Recessed-gate structure approach toward normally off high-Voltage AlGaN/GaN HEMT for power electronics applications,* IEEE Transactions on Electron Devices **53**, 356 (2006).

[19] J. Zhang, S. Huang, Q. Bao, X. Wang, K. Wei, Y. Zheng, Y. Li, C. Zhao, X. Liu, Q. Zhou, W. Chen, and B. Zhang, *Mechanism of Ti/Al/Ti/W Au-free ohmic contacts to AlGaN/GaN heterostructures via pre-ohmic recess etching and low temperature annealing,* Applied Physics Letters **107**, 262109 (2015).

[20] R. Chu, L. Shen, N. Fichtenbaum, D. Brown, Z. Chen, S. Keller, S. P. DenBaars, and U. K. Mishra, *V-Gate GaN HEMTs for X-Band Power Applications,* IEEE Electron Device Letters **29**, 974 (2008).

[21] S. Lenci, B. De Jaeger, L. Carbonell, J. Hu, G. Mannaert, D. Wellekens, S. You, B. Bakeroot, and S. Decoutere, *Au-Free AlGaN/GaN Power Diode on 8-in Si Substrate With Gated Edge Termination,* IEEE Electron Device Letters **34**, 1035 (2013).

[22] R. Vitushinsky, M. Crego-Calama, S. H. Brongersma, and P. Offermans, *Enhanced detection of* NO_2 *with recessed AlGaN/GaN open gate structures,* Applied Physics Letters **102**, 172101 (2013).

[23] C.-T. Lee and Y.-S. Chiu, *Photoelectrochemical passivated ZnO-based nanorod structured glucose biosensors using gate-recessed AlGaN/GaN ion-sensitive field-effect-transistors,* Sensors and Actuators B: Chemical **210**, 756 (2015).

[24] S. Huang, Q. Jiang, K. Wei, G. Liu, J. Zhang, X. Wang, Y. Zheng, B. Sun, C. Zhao, H. Liu, Z. Jin, X. Liu, H. Wang, S. Liu, Y. Lu, C. Liu, S. Yang, Z. Tang, J. Zhang, Y. Hao, and K. J. Chen, *High-temperature low-damage gate recess technique and ozone-assisted ALD-grown* Al_2O_3 *gate dielectric for high-performance normally-off GaN MIS-HEMTs,* in *2014 IEEE International Electron Devices Meeting* (2014) pp. 17.4.1–17.4.4.

[25] Y. Chiou, L. Huang, and C. Lee, *Photoelectrochemical Function in Gate-Recessed AlGaN/GaN Metal–Oxide–Semiconductor High-Electron-Mobility Transistors,* IEEE Electron Device Letters **31**, 183 (2010).

[26] C.-T. Lee, H.-W. Chen, F.-T. Hwang, and H.-Y. Lee, *Investigation of Ga oxide films directly grown on n-type GaN by photoelectrochemical oxidation using He-Cd laser,* Journal of Electronic Materials **34**, 282 (2005).

[27] Z. Xu, J. Wang, J. Liu, C. Jin, Y. Cai, Z. Yang, M. Wang, M. Yu, B. Xie, W. Wu, X. Ma, J. Zhang, and Y. Hao, *Demonstration of Normally-Off Recess-Gated AlGaN/GaN MOSFET Using GaN Cap Layer as Recess Mask,* IEEE Electron Device Letters **35**, 1197 (2014).

[28] D. Buttari, S. Heikman, S. Keller, and U. K. Mishra, *Digital etching for highly reproducible low damage gate recessing on AlGaN/GaN HEMTs*, in *Proceedings. IEEE Lester Eastman Conference on High Performance Devices* (2002) pp. 461–469.

[29] Y. Wang, M. Wang, B. Xie, C. P. Wen, J. Wang, Y. Hao, W. Wu, K. J. Chen, and B. Shen, *High-Performance Normally-Off Al_2O_3/GaN MOSFET Using a Wet Etching-Based Gate Recess Technique*, IEEE Electron Device Letters **34**, 1370 (2013).

[30] T. Hashizume and H. Hasegawa, *Effects of nitrogen deficiency on electronic properties of AlGaN surfaces subjected to thermal and plasma processes*, Applied Surface Science **234**, 387 (2004).

[31] A. Ortiz-Conde, F. J. García-Sánchez, J. Muci, A. T. Barrios, J. J. Liou, and C.-S. Ho, *Revisiting MOSFET threshold voltage extraction methods*, Microelectronics Reliability **53**, 90 (2013).

[32] J. P. Ibbetson, P. T. Fini, K. D. Ness, S. P. DenBaars, J. S. Speck, and U. K. Mishra, *Polarization effects, surface states, and the source of electrons in AlGaN/GaN heterostructure field effect transistors*, Applied Physics Letters **77**, 250 (2000).

[33] H. Fukuda, H. Seo, K. Kasama, T. Endoh, and S. Nomura, *Highly Sensitive MOSFET Gas Sensors with Porous Platinum Gate Electrode*, Japanese Journal of Applied Physics **37**, 1100 (1998).

6

Conclusions and research outlook

This chapter is a summary of the work carried out during this Ph.D. project on developing AlGaN/GaN high electron mobility transistor based field effect type sensors for gas sensing applications. Main findings and results are discussed. Afterwards, suggestions for future work are made to further advance the field of this exciting technology.

6.1. CONCLUSIONS

The necessity of sensing our surrounding environment has been continuously growing. The earliest gas detectors were essential to improve safety of coal mining during the industrial revolution. **Chapter 1** starts with a historical overview of the main chemical and gas sensor research developments up to the present times. There is no one sensing technology that can cover all possible use cases or meet the specific requirements of various industries. An analysis of most widely studied sensing traducers is presented, which includes optical, electrochemical, mass-sensitive, calorimetric, magnetic and electrical sensors. A detailed review of field effect type sensor operating principle is then presented, followed by a summary of previously reported applications and types of FET sensors made from silicon, various compound III-V and state-of-art wide-bandgap semiconductors.

Chapter 2 starts with a discussion of gallium nitride (GaN) material properties, which are also compared to other wide-bandgap semiconductors. The wurtzite crystal structure of GaN, which is the origin of unique polarization properties is presented, the physics of AlGaN/GaN heterostructure are described as well as the origin of the 2DEG. Afterwards the structure and operating principle of the HEMT based sensors is discussed and a review of previously demonstrated gas sensors based on GaN is given. The remainder of the chapter is dedicated to describing the newly developed AlGaN/GaN HEMT based sensor microfabrication process. Each layer of the starting epitaxial structure grown by MOCVD on sapphire substrates is described. The first processing step was mesa etching for individual device isolation by ICP-RIE plasma etching. Then significant efforts were made in order to develop low R_c ohmic contacts. To pattern multilayer Au-based metal stack, lift-off technique was implemented, which was later enhanced with a bilayer process using LOR to improve metal patterning yield. Optimization of contact annealing conditions allowed to obtain low R_c under 0.6 Ωmm. Following contact formation, the sensing gate electrodes were formed. Catalytic Pt was used as gate metal due to its high work function, thermal and chemical stability and sensitivity to hydrogen containing gases. Problem with poor Pt adhesion was resolved by passivating the sensor surface with $\mathrm{SiN_x}$ after Pt patterning instead of before. Fabricated sensors were diced using laser scribing and bonded to high temperature tolerant ceramic PCBs.

Prior to fabricating the AlGaN/GaN HEMT sensors a set of photolithography masks with various layouts was designed as discussed in **Chapter 3**. The dimensions of the gate electrode were selected as design variables to have several gate width to length ratios (W_g/L_g). HEMT output current (I_{DS}) and transconductance (g_m) are directly related to this ratio. The first mask set contained sensors with W_g/L_g ratios from 0.25 to 10.

The gas testing methodology and equipment are also introduced in this chapter. The fabricated sensors were tested towards response to H_2 from 5 to 500 ppm. The detection limit of sensors with W_g/L_g=0.25 was above 20 ppm. Increasing the ratio to 10 lowered the detection limit to 5 ppm. Sensing response towards 500 ppm increased from 3.5 to 7.6 % and signal variation from 15.2 to 695 µA. Response times have gradually decreased with higher W_g/L_g however the recovery times increased. Based on these results a new set of masks with W_g/L_g up to 100 were fabricated.

The fabricated Pt-AlGaN/GaN HEMT sensors were applied for detection of toxic hydrogen sulfide (H_2S) gas as described in **Chapter** 4. These sensors were able to detect H_2S in the range of 15–90 ppm. As fabricated devices were found to exhibit sensing signal saturation at 30 ppm H_2S in air. Sensor pre-treatment with pulses of H_2 and air at 250 °C allowed to extend the sensing range up to 90 ppm. It was attributed to incorporation of positively charged H^+ ions in the Pt film and the induced negative charges on the Pt surface, which prevented some of the hydrogen atoms from diffusing to the metal-semiconductor interface, resulting in lower signal magnitude at 30 ppm and extended overall detection range. The H_2-treated sensors were tested at temperatures from 150 to 250 °C. Low response magnitude and large baseline drift were observed at 150 °C. The magnitude of the sensing signal increased significantly at 200 and 250 °C, up to ΔI_{DS}=2.2 mA (at V_{GS}=1 V) and the obtained sensing response was 112 % (at V_{GS}=−3 V). These sensors also exhibited excellent stability characteristics under broad range of drain bias (V_{DS}) conditions and during response testing for a period of 15 days. The response and recovery times towards 90 ppm H_2S reduced by 54 % and 61.5 %, respectively when the operating temperature was increased from 200 to 250 °C. Hence, GaN based sensors operate reliably at temperatures above the Si-based FET sensor limit which expands their application domains. Response to H_2S was also 4.5x higher than H_2 under same gas concentrations.

6

Gate recess is a well-known and widely studied method to obtain enhancement mode (E-mode) HEMTs. In **Chapter** 5 the impact of etching a recess in the AlGaN barrier on the H_2 sensing characteristics is studied. In order to precisely recess few nanometers of AlGaN a two-step cyclic etching method was developed. The first step was oxidizing the AlGaN/GaN surface using oxygen plasma oxidation in an ICP-RIE etcher. The oxidized surface was then selectively etched with a HCl solution. This cycle was then repeated until the desired recess depth was achieved. It was possible to control thickness of the oxidized AlGaN layer and hence the etching rate from 0.6 to 11nm/cycle by varying the RF and ICP power values. Sensors with increasing recess depth from 5 to 15 nm were fabricated using this recess etching approach and analyzed with AFM, STEM and EDS.

As expected etching a recess in the AlGaN barrier under the Pt gate electrode, resulted in the lowering of the drain output current (I_{DS}) and positive shift of threshold voltage (V_{TH}). An E-mode sensor with V_{TH} =1.49 V was obtained for recess depth of 15 nm. Hydrogen response characteristics of sensors with 4 recess depths were studied and compared to non-recessed reference device. Shallow recess (5 and 10 nm) sensors obtained higher maximum transconductance and higher signal variation (ΔI_{DS}) towards 300 ppm H_2 compared to the reference device. The sensing response increased with recess depth from 13.2 to 145.8 % due to lowering of the baseline current value. Transient response characteristics were significantly improved by implementing recessed gate sensors. The response time reduced by 3x and the recovery time by 3.3x for recess depth of 15 nm. Furthermore barrier recess etching significantly lowered the power consumption of the sensors. At 240 °C the power consumption reduced by 50x.

6.2. RESEARCH OUTLOOK

Gallium nitride is highly anticipated to replace silicon as material for high power, high voltage switching devices and high frequency power amplifiers due to its adventagious material properties compared to Si and GaAs [1]. While GaN devices for power switching and RF applications are already being commercialized, their application towards detection of gases and chemical elements is still an emerging technology. Based on previously reported results as well as those demonstrated in this dissertation it is evident that GaN-based field effect sensors can be implemented for wide range of sensing applications. Numerous further research initiatives are possible to advance this technology. GaN HEMT sensors that can reliably operate at very high temperature >400 °C require further development. Previously reported high temperature HEMT Pt sensors were studied under N_2 or oxygen deficient (4 % O_2) ambient [2–4]. More investigations under high temperature air ambient are necessary to establish device reliability and enable detection of hydrocarbons. It is expected that inserting a stable insulator layer between gate electrode and GaN to form MIS-HEMT sensors will improve their sensing performance under high temperature. Our results demonstrated improvement of sensing performance with recessed gate HEMTs, therefore recess MIS-HEMTs should also be investigated for gas sensing as it would allow to minimize gate leakage current when of the barrier thickness is only few nanometres.

GaN-based devices are naturally depletion mode, so the gate electrode is not strictly necessary to form a conductive channel between the source and drain. The gate region of the sensor can therefore be functionalized with non-metal sensing layers such as metal-oxides, polymers or nano-structures [5–7]. Numerous other GaN HEMT and sensing layer combinations can therefore be studied and combined on a single chip to form multiple gas detectors, i.e. electronic noses. Sensors that incorporate a gas sensitive oxide combined with catalytic metal gate into reactive metal-insulator structures should also be investigated [8, 9].

REFERENCES

[1] T. Ueda, M. Ishida, T. Tanaka, and D. Ueda, *GaN transistors on si for switching and high-frequency applications,* Japanese Journal of Applied Physics **53**, 100214 (2014).

[2] J. Schalwig, G. Müller, M. Eickhoff, O. Ambacher, and M. Stutzmann, *Group III-nitride-based gas sensors for combustion monitoring,* Materials Science and Engineering: B **93**, 207 (2002).

[3] J. Song and W. Lu, *Operation of Pt/AlGaN/GaN-Heterojunction Field-Effect-Transistor Hydrogen Sensors With Low Detection Limit and High Sensitivity,* IEEE Electron Device Letters **29**, 1193 (2008).

[4] Y. Halfaya, C. Bishop, A. Soltani, S. Sundaram, V. Aubry, P. Voss, J.-P. Salvestrini, and A. Ougazzaden, *Investigation of the Performance of HEMT-based NO, NO_2 and NH_3 Exhaust Gas Sensors for Automotive Antipollution Systems,* Sensors **16**, 273 (2016).

[5] S.-T. Hung, C.-J. Chang, C. C. Chen, C. F. Lo, F. Ren, S. J. Pearton, and I. I. Kravchenko, *SnO_2-gated AlGaN/GaN high electron mobility transistors based oxygen sensors,* Journal of Vacuum Science & Technology B **30**, 041214 (2012).

[6] C. Y. Chang, B. S. Kang, H. T. Wang, F. Ren, Y. L. Wang, S. J. Pearton, D. M. Dennis, J. W. Johnson, P. Rajagopal, J. C. Roberts, E. L. Piner, and K. J. Linthicum, *CO_2 detection using polyethylenimine/starch functionalized AlGaN/GaN high electron mobility transistors,* Applied Physics Letters **92**, 232102 (2008).

[7] S. C. Hung, C. W. Chen, C. Y. Shieh, G. C. Chi, R. Fan, and S. J. Pearton, *High sensitivity carbon monoxide sensors made by zinc oxide modified gated GaN/AlGaN high electron mobility transistors under room temperature,* Applied Physics Letters **98**, 223504 (2011).

[8] A. Trinchi, K. Galatsis, W. Wlodarski, and Y. X. Li, *A Pt/Ga_2O_3-ZnO/SiC Schottky diode-based hydrocarbon gas sensor,* IEEE Sensors Journal **3**, 548 (2003).

[9] M. Miyoshi, S. Fujita, and T. Egawa, *Demonstration of NOx gas sensing for Pd/ZnO/GaN heterojunction diodes,* Journal of Vacuum Science & Technology B **33**, 013001 (2015).

Summary

The rapid development and market growth of microelectronics technology continues to provide expanding connectivity, productivity, entertainment and well-being to billions of users globally. Moreover, continuous demand for more on-chip functionally presents an exciting opportunity for integration of various chemical sensors for monitoring pollution of our surrounding environment and exposure to toxic, corrosive or flammable gases.

Historically, investigations into gas detectors started during the industrial revolution; the mining industry needed devices that could reduce the amount of mining and other occupational accidents. Significant progress in chemical and gas sensor research began during the 1920s. Since then numerous sensing methods with different transducer types such as optical, electrochemical, mass-sensitive, calorimetric, magnetic or electrical have been studied and some commercialized. Microelectronic devices such as MOS capacitors, Schottky diodes and transistors are favourable for developing highly miniaturized integrated gas sensors. Since the first demonstration of a Si-MOSFET H_2 sensor with a Pd gate numerous modifications were developed in order to expand this technology towards wider range of analytes. The maximum operating temperature of these sensors is however limited by the low energy bandgap of silicon. Furthermore, silicon is also susceptible to chemical etching, hence not suitable for corrosive ambient. Wide-bandgap gallium nitride (GaN) is a highly chemically stable semiconductor suitable for harsh environment applications. The objective of this research project is to develop a gas sensor based on AlGaN/GaN high electron mobility transistor (HEMT). To achieve this, a micro-fabrication process is developed, sensor layout is designed and the sensor response is characterised for several gases.

The device physics and fabrication process of GaN HEMTs significantly differs from Si MOSFET or CMOS technology. Due to the wurtzite crystal structure, GaN possesses strong spontaneous polarization effects. When a heterojunction of AlGaN/GaN is made there is a net polarization difference at the interface, that results in a the formation of a highly conductive electron channel, the two-dimensional electron gas (2DEG). The initial epitaxial structure with low sheet resistance was defined and purchased from a commercial vendor. It was grown by MOCVD on chemically stable c-plane sapphire substrates which allows to obtain high crystal quality. The fabrication process began with isolating individual devices by forming mesa structures via ICP-RIE etching. Afterwards the contact process was developed to obtain low ohmic contact resistance ($R_C <$ $1\,\Omega\,\mathrm{mm}$). It involved optimization of the contact metal stack composition, the thickness of each layer, the time and temperature of the rapid thermal annealing. Furthermore, the lift-off process used to pattern Au containing metal layers, was modified by using bilayer photolithography with LOR resist to improve the yield and quality of the formed patterns. The gate electrode used for gas detection was Pt deposited by e-beam evaporation. To improve adhesion, it was patterned directly on the GaN layer, before surface passivation. Completed devices were packaged on ceramic PCBs for high temperature gas testing.

Several designs of AlGaN/GaN HEMT sensors were made in order to optimize gas sensing performance. The width (W_g) and length (L_g) of the sensing gate electrode were the design variables, as they directly impact the output drain current (I_{DS}) and the transconductance (g_m) of the transistor. Sensors with increasing W_g/L_g ratio were studied towards H_2 in air. They were placed inside the small volume hermetic chamber with temperature and humidity control. Test gas of known concentration and flow rate was supplied using a computer-controlled gas mixing system with mass flow controllers. Sensors with W_g/L_g ratios from 0.25 to 10 were tested and the results demonstrated that signal variation and sensing response increased with higher ratios. The detection limit was lowered from >20 ppm down to 5 ppm. Transient characteristics demonstrated a reduction in response time and increase in recovery time with increasing W_g/L_g. Based on these findings, a second generation design was made, which included W_g/L_g ratios up to 100.

The fabricated sensors were investigated for detection of H_2S. The gas response was tested at temperatures of 150–250 °C and the sensors demonstrated promising sensing characteristics in the 15–90 ppm concentration range. The as–fabricated sensors exhibited signal saturation at 30 ppm H_2S concentration. A high temperature pre-treatment with H_2 pulses was introduced which allowed to extend the H_2S detection range, due to incorporation of positive H^+ ions in the Pt sensing electrode. At 150 °C the sensors exhibited low response to H_2S. Raising the temperature to 200 °C significantly enhanced the sensing response and signal variation. Transient measurements validated excellent response, recovery and repeatability characteristics. Increasing the temperature to 250 °C reduced the response and recovery times by more than 2x. Selectivity towards H_2 was 4.5x and response to NO_2 was very low at 250 °C. The long–term stability was confirmed with response tests over a period of 15 days and no significant signal degradation was observed.

Gate recess is a known method to achieve enhancement mode AlGaN/GaN HEMTs by partially or completely etching the AlGaN barrier under the gate electrode in order to deplete the 2DEG. Conventional plasma etching technique frequently results in barrier surface damage, non-uniformities and Cl residues. In this work, a method was developed to precisely recess etch the AlGaN layer without causing surface damage. It involved first oxidizing the surface with oxygen plasma in ICP-RIE etcher. The ICP and RF power determined the depth of oxidised layer. Afterwards the oxide was etched using HCl solution and the cycle was repeated until the required depth of etching was obtained. The measured recess depth from ~0.6 to 11nm/cycle was obtained, depending on the power settings of the oxidation step. This method was applied to fabricate Pt-AlGaN/GaN HEMT sensors with increasing gate recess depth and tested towards H_2 detection. The output current reduced with increasing recess depth up to 15 nm as the density of electrons in 2DEG channel under the gate electrode gradually decreased. The threshold voltage shifted from -1.57 V towards positive values and devices with 15 nm recess became E–mode, with V_{TH} =1.49 V. As compared to non-recessed reference device, sensors with shallow recess of 5 and 10 nm demonstrated higher sensing signal variation towards 300 ppm. Sensing response gradually increased with recess depth from 13.2 to 145.8 %. The response and recovery times decreased by 3x for the 15 nm recessed sensor. Furthermore, gate recess etching reduced the power consumption of the HEMT sensor up to 50x.

This thesis is concluded with summarizing the main obtained results and providing suggestions for future research opportunities in the field of GaN-based gas/chemical sensors.

Samenvatting

De snelle ontwikkeling en marktgroei van micro-elektronica-technologie blijft miljarden gebruikers wereldwijd voorzien van groeiende connectiviteit, productiviteit, entertainment en welzijn. Bovendien leid de voortdurende vraag naar meer on-chip functionaliteit ook tot mogelijkheden voor in-chip integratie van verschillende chemische sensoren voor het monitoren van vervuiling van onze omgeving en blootstelling aan giftige, corrosieve of ontvlambare gassen.

Historisch gezien begonnen onderzoeken naar gasdetectors tijdens de industriële revolutie; de mijnbouw industrie had behoefte aan apparaten die het aantal mijnbouw en andere arbeidsongevallen konden verminderen. Aanzienlijke vooruitgang in het onderzoek naar chemische en gassensoren begon in de jaren 1920. Sindsdien zijn talloze detectiemethoden met verschillende transducertypen bestudeerd, zoals optisch, elektrochemisch, massagevoelig, calorimetrisch, magnetisch of elektrisch en sommige hiervan met commercieel succes. Micro-elektronische apparaten zoals MOS-condensatoren, Schottky-diodes en transistoren zijn gunstig voor het ontwikkelen van sterk geminiaturiseerde en geïntegreerde gassensoren. Sinds de eerste demonstratie van een Si-MOSFET H_2-sensor met een Pd-gate elektrode werden tal van wijzigingen ontwikkeld om deze technologie uit te breiden naar een breder scala aan analyten. De maximale bedrijfstemperatuur van deze sensoren wordt echter beperkt door de lage energie bandafstand van Silicium. Bovendien is silicium vatbaar voor chemisch etsen en daarom niet geschikt voor corrosieve omgevingen. Wide-bandgap gallium nitride (GaN) is een zeer chemisch stabiele halfgeleider die geschikt is voor barre omgevingen. Het doel van dit onderzoek is om gas sensor te ontwikkelen gebaseerd op AlGaN/GaN hoge elektronenmobiliteit transistoren (HEMT). Om dit te bereiken is een micro-fabricageproces ontwikkeld, de sensor lay-out is ontworpen en de respons van de sensoren op verschillende gassen is gekarakteriseerd.

De device fysica en het fabricageproces van GaN HEMT's verschillen aanzienlijk van Si MOSFET- of CMOS-technologie. Vanwege de wurtzite kristalstructuur bezit GaN sterke spontane polarisatie-effecten. Wanneer een heterojunctie van AlGaN/GaN wordt gemaakt, is er een netto polarisatieverschil op het grensvlak, dat resulteert in de vorming van een goed geleidend elektronenkanaal, het tweedimensionale elektrongas (2DEG).

De initiële epitaxiale structuur met lage film-weerstand is op specificatie ingekocht bij een commerciële partij. De epitaxiale structuur is gegroeid door middel van MOCVD op de chemisch stabiele c-vlakken van saffiersubstraten waarmee het mogelijk is om een hoge kristalkwaliteit te realiseren. Het fabricageproces start de fabricage van mesastructuren via ICP-RIE-etsen waarmee later de afzonderlijke devices worden geïsoleerd. Daarna is een contactproces ontwikkeld om een lage Ohmse contactweerstand ($R_C < 1\,\Omega\,\mathrm{mm}$) te verkrijgen. Dit is bereikt door optimalisatie van de samenstelling van de contactmetaalstapeling, de dikte van elke laag, en temperatuur en tijd van de snelle thermische gloeiing. Verder is het lift-off proces dat is gebruikt om Au-bevattende metaallagen te vormen, gemodificeerd met behulp van dubbellaagse fotolithografie met LOR-resist om de opbrengst en kwaliteit van de gevormde patronen te verbeteren. De gate-elektrode die is gebruikt voor gasdetectie bestaat uit Pt, gedeponeerd door elektronenstraal verdamping. Om de hechting te verbeteren, is deze direct op de GaN-laag gedeponeerd, voordat de oppervlakte passivatie is uitgevoerd. Gecompleteerde devices zijn geassembleerd keramische PCB's voor het uitvoeren van testen op hoge temperatuur in gas.

Er zijn verschillende ontwerpen van AlGaN/GaN HEMT-sensoren gemaakt om de gasdetectie te optimaliseren. De ontwerpvariabelen zijn de breedte (W_g) en lengte (L_g) van de detectie gate-elektrode, omdat deze rechtstreeks van invloed zijn op de drainstroom (I_{DS}) en de transconductantie (g_m) van de transistor. Sensoren met toenemende W_g/L_g-verhouding zijn bestudeerd H_2 en in lucht ter referentie. De sensoren zijn in een hermetisch gesloten kamer met een klein volume geplaatst en met temperatuur- en vochtigheidsregeling. Testgas met bekende concentratie en stroomsnelheid is geleverd met behulp van een computergestuurd gasmengsysteem met massastroomregelaars. Sensoren met W_g/L_g-verhoudingen van 0,25 tot 10 zijn getest en de resultaten tonen aan dat signaalvariatie en detectie-respons toenemen met hogere W_g/L_g-verhoudingen. De detectielimiet is verlaagd van > 20 ppm tot 5 ppm. Dynamische karakterisatie vertoont een vermindering van de responstijd en een toename van de hersteltijd met toenemende W_g/L_g. Op basis van deze bevindingen is een ontwerp van de tweede generatie gemaakt met W_g/L_g-verhoudingen tot 100.

De gefabriceerde sensoren zijn onderzocht op detectie van H_2S. De gasreactie werd getest bij temperaturen van 150–250 °C en de sensoren vertonen veelbelovende detectie-eigenschappen in het concentratiebereik van 15–90 ppm. Net vervaardigde sensoren vertonen signaalverzadiging bij een concentratie van 30 ppm H_2S. Een voorbehandeling op hoge temperatuur met H_2-pulsen is geïntroduceerd die het mogelijk maakt het H_2S-detectiebereik te vergroten, vanwege de opname van positieve H^+ -ionen in de Pt-detectie-elektrode. Bij 150 °C vertonen de sensoren een lage respons op H_2S. Door de temperatuur te verhogen tot 200 °C wordt de detectie-respons en signaalvariatie aanzienlijk verbeterd. Dynamische metingen valideren de uitstekende eigenschappen van respons, herstel en herhaalbaarheid. Door de temperatuur te verhogen tot 250 °C zijn de respons- en hersteltijden met meer dan 2x verlaagd. De selectiviteit voor H_2 is 4,5x en de respons op NO_2 is zeer laag bij 250 °C. De stabiliteit op lange termijn is bevestigd met responsietests gedurende een periode van 15 dagen en er is geen significante signaalverslechtering waargenomen.

De verlaagde gate structuur is een bekende methode waarmee de E–modus van AlGaN/GaN HEMT's wordt versterkt. Dit wordt bereikt door de AlGaN-barrière onder de gate-elektrode gedeeltelijk of volledig te etsen om de 2DEG te depleteren. Conventionele plasma-etstechnieken resulteren vaak in barrière oppervlakschade, niet-uniformiteiten en Cl-residuen. In dit werk is een methode ontwikkeld om de AlGaN-laag nauwkeurig te verlagen zonder oppervlakteschade te veroorzaken. De 1-e stap is het oxideren van het oppervlak door middel van zuurstofplasma in een ICP-RIE etser. Het ICP- en RF-vermogen bepalen de diepte van de geoxideerde laag. Daarna is het oxide geëtst met behulp van HC1-oplossing en de cyclus werd herhaald totdat de vereiste etsdiepte is bereikt. De gemeten laagafname van ~0,6 tot 11 nm/cyclus is afhankelijk van de vermogensinstellingen van de oxidatiestap. Deze methode is toegepast om Pt-AlGaN/GaN HEMT-sensoren te produceren met toenemende gate-uitsparingsdiepte en getest op H_2-detectie. De uitgangsstroom verminderd met toenemende diepte van de uitsparing tot 15 nm in relatie met de geleidelijke afname van de dichtheid van elektronen in 2DEG-kanaal onder de gate-elektrode. De drempelspanning verschuift van −1,57 V naar positieve waarden en devices met een uitsparing van 15 nm worden E—modus devices, met V_{TH} =1,49 V. In vergelijking met niet-verzonken referentie devices vertonen sensoren met een ondiepe uitsparing van 5 en 10 nm een grotere variatie van het detectiesignaal naar 300 ppm.

De detectierespons neemt geleidelijk toe met een diepte van 13,2 nm tot 145,8 %. De respons- en hersteltijden nemen met 3x af voor de 15 nm verlaging sensor. Bovendien verminderd een geëtste gate-uitsparing het stroomverbruik van de HEMT-sensor tot 50x.

Dit proefschrift wordt afgesloten met een samenvatting van de belangrijkste verkregen resultaten en suggesties voor toekomstige onderzoeksmogelijkheden op het gebied van op GaN gebaseerde gas/chemische sensoren.

Acknowledgements

As I am approaching the end of my Ph.D. studies I realise that none of the obtained results would have been possible without the support, encouragement and dedication of numerous people that have contributed to this work. I would hereby like to express my sincere gratitude to all these exceptional individuals.

First of all, I would like to thank my promotor prof. dr. Guoqi Zhang for providing the exciting opportunity to do my PhD research at TU Delft, BRC. Our encouraging discussions helped me to make up my mind to conduct research in China. During my entire Ph.D. research duration, Prof. Zhang provided excellent guidance, support and feedback regarding all aspects of my work. I was able to work in several locations across China thanks to his extensive networking efforts to ensure collaboration with universities and research institutes in Changzhou, Beijing and Shenzhen. Prof. Zhang would always help to find the best solution to any problem encountered during my stay in China and introduce me to people who may provide useful assistance.

I would also like thank my daily supervisor duo Dr. Elina Iervolino and Dr. Fabio Santagata. Their strong expertise in the field of microelectronics, microfabrication technology as well as research management were extremely valuable. They have also helped me to settle in Shenzhen find accommodation and the internship in Founder IC. Working together was a really fulfilling experience for me. They helped me to gain initial insight into doing research as well as entrepreneurship opportunities in China. I knew that I could count on them to help me with any issues I encountered at any time and I truly value the friendship we have developed.

I am very grateful to Prof. Pasqualina M. Sarro for providing highly useful feedback and encouragement on my work progress. Her suggestions on how to improve my manuscripts and abstracts were always valuable.

During my research I have received immense support from CSA, SKL and IOS. I am grateful to Dr. Jun Ruan and Madam Ling Wu for proving financial support during my work in Changzhou and Beijing as well as helping with all the required work permits in China. My gratitude also goes out to Prof. Junxi Wang for introducing me to the IOS microfabrication facilities and the cleanroom manager Ms. Li Wang for helping me to optimize my process flowchart to meet their requirements. Many thanks to all the engineers of the IOS cleanroom for their assistance in fabricating, packaging and measuring my devices.

A significant part of my research was conducted at The Southern University of Science and Technology in Shenzhen. I am immensely grateful to Prof. Hongyu Yu for inviting me to join his group at SUSTech and providing the necessary infrastructure, technical discussions and funding. My thanks also go out to the students and researchers of Prof. Yu's group: Xinpeng Lin, Wenmao Li, Guangnan Zhou, Yang Jiang, Jingyi Wu, Wei-Chih Cheng, Siqi Lei, Yumeng Zhu, Marzieh Mahrokh, Hongze Zheng, Fanming Zeng, Ganhui Chen and others for sharing their useful experimental results and procedures, helping to perform experiments and useful discussions. I would also like to acknowledge Jian Zhang and Meng-Ya Fan visiting students from Fudan University for their contribution to device fabrication and testing. I am very thankful to the cleanroom engineering staff of the Materials Characterization and Preparation Center of SUSTech for their support in device fabrication and process calibration. Furthermore, I must express my gratitude to Prof. Gaiying Yang, Dr. Dongsheng He and Dr. Yang Qiu for their training and support in sample preparation and analysis with FIB, TEM and EDS. Thank you to prof. Guangrui Xia from University of British Columbia for many highly insightful discussions and suggestions regarding my research. Special thanks to Prof. Fei Wang and Dr. Changhui Zhao for providing training and allowing me to use their gas sensor testing equipment.

I would to acknowledge the financial support for my research from Shenzhen city government project via grant "Research of AlGaN HEMT MEMS sensor for work in extreme environment"(Grant no: JCYJ20170412153356899).

My gratitude goes to Prof. Shunfeng Li and Prof. Guoyi Zhang for introducing me to Founder Microelectronics Co. when I first arrived to Shenzhen. I am very grateful to Jianguo Chen, director of product development, for offering me an internship at their company and providing the opportunity to work in a modern semiconductor foundry. I really enjoyed working with Anatoly Turyhin and Dr. Hui Sun on the development of CMOS compatible GaN HEMTs.

I am truly thankful to my SKL and BRC collogues: Mingzhi Dong, Jianwen Sun, Bo Sun, Hongyu Tang, Manjunath Ramachandrappa Venkatesh and Guangjun Lv for their help with getting accustomed to living in China, introducing me to necessary people and helping to perform experiments. Long hours spent working together were really memorable and fruitful.

I would also like to thank all the members of ECTM group, EKL laboratory and the research group of Prof. Zhang at TU Delft: Dr. Gregory Pandraud, Dr. Henk van Zeijl, Dr. Rene Poelma, Brahim Mansouri, Dr. Aleksandar Jovic, Yelena Grachova, Dr. Jing

Zhang, Dr. Xueming Li, Dr. Cinzia Silvestri, Dr. Pan Liu and Dr. Bruno Morana. It was really enjoyable working together and sharing some wonderful conversations over a cup of coffee. Special thanks to Dr. Henk van Zeijl for helping me with with translation of the summary and propositions to Dutch.

Lastly, my sincere gratitude goes to my mom, my family, friends and Shiqing Zhang for all the help, support and encouragement to successfully conclude my Ph.D. research.

Curriculum Vitæ

Robert SOKOLOVSKIJ

13-01-1987	Born in Vilnius, Lithuania.

EDUCATION

2014–2019	PhD in Microelectronics Delft University of Technology, Delft, The Netherlands	
	Thesis:	AlGaN/GaN high electron mobility transistor (HEMT) based sensors for gas sensing applications
	Promotor:	Prof. dr. G. Q. Zhang
2011–2013	Master of Science in Electrical Engineering Delft University of Technology, Delft, The Netherlands	
	Thesis:	Foldable 3D Wafer Level SSL Package Using Flexible Interconnect
	Promotor:	Prof. dr. G. Q. Zhang
2006–2010	Bachelor in Telecommunications Physics and Electronics Vilnius University, Vilnius, Lithuania	

Work experience

2018–	Research assistant The Southern University of Science and Technology, Shenzhen, China
2014–2018	Engineer State Key Laboratory of Solid State Lighting, Changzhou, China
2012–2013	Intern Philips Lighting, Eindhoven, The Netherlands
2009–2011	Telecommunications Engineer Saugumo vizija, Vilnius, Lithuania

Projects

2017–2020	Research of AlGaN HEMT MEMS sensor for work in extreme environment (Grant no: JCYJ20170412153356899)

List of Publications

JOURNAL PAPERS

1. **R. Sokolovskij**, P. Liu, H. W. Van Zeijl, B. Mimoun, and G. Q. Zhang, *Design and Fabrication of a Foldable 3D Silicon Based Package for Solid State Lighting Applications*, Journal of Micromechanics and Microengineering, **25**, 055017 (2015).

2. M. Dong, F. Santagata, **R. Sokolovskij**, J. Wei, C. Yuan, and G. Q. Zhang, *3D system-in-package design using stacked silicon submount technology*, Microelectronics International, **32**, pp. 63-72 (2015).

3. **R. Sokolovskij**, J. Zhang, E. Iervolino, C. Zhao, F. Santagata, F. Wang, H. Yu, P. M. Sarro, and G. Q. Zhang, *Hydrogen Sulfide Detection Properties of Pt-Gated AlGaN/GaN HEMT-Sensor*, Sensors and Actuators B: Chemical, **274**, pp. 636-644, (2018).

4. J. Zhang, **R. Sokolovskij**, G. Chen, Y. Zhu, Y. Qi, X. Lin, W. Li, G. Q. Zhang, Y. L. Jiang, and H. Yu, *Impact of high temperature H_2 pre-treatment on Pt-AlGaN/GaN HEMT sensor for H_2S detection*, Sensors and Actuators B: Chemical, **280** pp. 138-143 (2019).

5. H. Tang, Y. Li, **R. Sokolovskij**, L. Sacco, H. Zheng, H. Ye, H. Yu, X. Fan, H. Tian, T. L. Ren, and G. Q. Zhang, *Ultra-High Sensitive NO_2 Gas Sensor Based on Tunable Polarity Transport in CVD-WS_2/IGZO p-N Heterojunction*, ACS Applied Materials & Interfaces, **11**, (2019).

6. J. Sun, **R. Sokolovskij**, E. Iervolino, F. Santagata, Z. Liu, P.M. Sarro, and G.Q. Zhang, *Characterization of an Acetone Detector Based on a Suspended WO_3-Gate AlGaN/GaN HEMT Integrated With Microheater*, IEEE Transactions on Electron Devices, **66** pp. 4373-4379 (2019).

7. J. Sun, **R. Sokolovskij**, E. Iervolino, Z. Liu, P.M. Sarro, and G.Q. Zhang, *Suspended AlGaN/GaN HEMT NO_2 Gas Sensor Integrated With Micro-heater*, Journal of Microelectromechanical Systems, Early Access pp. 1-8 (2019).

8. **R. Sokolovskij**, J. Zhang, H. Zheng, W. Li, Y. Jiang, G. Yang, H. Yu, P. M. Sarro, G.Q. Zhang, *The Impact of Gate Recess on the H_2 Detection Properties of Pt-AlGaN/GaN HEMT Sensors*, IEEE Sensors Journal (submitted).

CONFERENCE PAPERS

1. P. Liu, H. W. Van Zeijl, M. R. Venkatesh, **R. Sokolovskij**, R. Kurt, and G. Q. Zhang, *Review on retrofit G4 LED lamps: Technology, challenges, and future trends*, in Proc.IEEE 65th Electronic Components and Technology Conference (ECTC), San Diego (USA), **25**, pp. 2277-2282 (2015).
2. **R. Sokolovskij**, J. Sun, F. Santagata, E. Iervolino, S. Li, G.Y. Zhang, P.M. Sarro, and G.Q. Zhang, *Precision Recess of AlGaN/GaN with Controllable Etching Rate Using ICP-RIE Oxidation and Wet Etching*, Procedia Engineering, **168**, pp. 1094-1097 (2016).
3. **R. Sokolovskij**, E. Iervolino, C. Zhao, F. Santagata, F. Wang, H. Yu, P. M. Sarro, and G. Q. Zhang, *Pt-AlGaN/GaN HEMT-Sensor for Hydrogen Sulfide (H_2S) Detection*, in Proc. Eurosensors Conference, Paris, pp. 3–6 (2017).
4. Y. Hu, J. Yang, Z. Huang, **R. Sokolovskij**, and F. Wang, *Wireless sensor node with hybrid energy harvesting for air-flow rate sensing*, in Proc. IEEE Sensors Conf., Glasgow, 2017, pp. 1-3.
5. **R. Sokolovskij**, E. Iervolino, C. Zhao, F. Wang, H. Yu, P.M. Sarro, and G.Q. Zhang, *Pt-AlGaN/GaN HEMT-sensor layout optimization for enhancement of hydrogen detection*, in Proc. IEEE Sensors Conf., Glasgow, 2017, pp. 1-3.
6. W. Li, J. Zhang, **R. Sokolovskij**, Y. Zhu, Y. Qi, X. Lin, J. Wu, L. Jiang, and H. Yu, *Au-based and Au-free ohmic contacts to AlGaN/GaN structures on silicon or Sapphire substrates*, in Proc. 18th International Workshop on Junction Technology (IWJT), Shanghai, 2018, pp. 1-4.
7. **R. Sokolovskij**, J. Zhang, Y. Jiang, G. Chen, G. Q. Zhang, and H. Yu, *AlGaN/GaN HEMT micro-sensor technology for gas sensing applications*, in 14th IEEE International Conference on Solid-State and Integrated Circuit Technology (ICSICT), Qingdao, 2018, pp. 1-3.
8. **R. Sokolovskij**, J. Zhang, H. Zheng, W. Li, Y. Jiang, G. Yang, H. Yu1, P. M. Sarro, G.Q. Zhang, *Recessed gate Pt-AlGaN/GaN HEMT H2 sensor*, in Proc. IEEE Sensors Conf., Montreal, 2019, pp. 1-3.

PATENTS

1. F. Santagata, E. Iervolino, **R. Sokolovskij**, M. Dong, and G. Q. Zhang, *Sensor, preparation method and multi-sensor system*, CN Patent WO2017088560A1 (2016).
2. F. Santagata, E. Iervolino, **R. Sokolovskij**, M. Dong, and G. Q. Zhang, *Wet corrosion method of group III nitride*, CN Patent WO2017101535A1 (2016).